DOCTORAL THESIS

Artificial Neuron Model for Large Scale Spiking Brain Neural Network

A unified hybrid excitable cell model for neurons, cardiac myocytes and the brain–heart interface





100 billion neurons simulated

86 % spike coincidence

8 species · cardiac AP

DR. ASIF MEHMOOD

DOCTOR OF PHILOSOPHY · COMPUTER SCIENCE

Supervisor: Dr Muhammad Javed Iqbal

University of Engineering and Technology, Taxila, Pakistan

2025



Artificial Neuron Model for Large Scale Spiking Brain Neural Network

A thesis submitted in partial fulfilment of the requirements for the degree of

Doctor of Philosophy in Computer Science

PRESENTED BY

Dr. Asif Mehmood

Registration No. 2017-UET/PhD-CS-09

SUPERVISOR

Dr Muhammad Javed Iqbal

Department of Computer Science

Faculty of Telecommunication and Information Engineering

University of Engineering and Technology, Taxila, Pakistan

July 17, 2025

Publications

The research presented in this thesis has been published in the following peer-reviewed journals and conference proceedings.

Arabian Journal for Science and Engineering

Asif Mehmood, Muhammad Javed Iqbal. *"Hybrid Spiking Neural Networks for Anomaly Detection of Brain, Heart and Pancreas."*

doi: 10.1007/s13369-024-08833-w

IEEE Access, vol. 11, pp. 128187–128197, 2023

Asif Mehmood, Muhammad Javed Iqbal. *"Hybrid Excitable Spiking Neural Network for Cardiovascular Disease Prediction."*

doi: 10.1109/ACCESS.2023.3330439

Neural Computing and Applications

Asif Mehmood, Muhammad Javed Iqbal. *"A Unified Hybrid Excitable Cell Model for Anomaly Detection of Heart."*

doi: 10.1007/s00521-025-11674-9

Neuroinformatics

Asif Mehmood, Ayesha Ilyas, Hajira Ilyas. *"Cardiac Heterogeneity Prediction by Cardio-Neural Network Simulation."*

doi: 10.1007/s12021-025-09717-6

14th Int. Conf. on Computational Intelligence and Security (CIS), IEEE, 2018, pp. 1–5

Asif Mehmood, Muhammad Javed Iqbal, Hassan Dawood, Ping Guo. *"Computationally Efficient Low Power Neuron Model for Digital Brain."*

IEEE Xplore: 8564247

Acknowledgment

I would like to express my sincere gratitude to my supervisor **Dr. Muhammad Javed Iqbal**, Assistant Professor, Faculty of Telecommunication and Information Engineering, University of Engineering and Technology, Taxila, Pakistan, for his continuous support, helpful advice and valuable guidance throughout this project work. His emphasis for excellence kept me well-directed and focused. He has made me able to follow the thesis plan very smoothly through his well defined execution and cooperation day in and day out. His cheerful and enthusiastic encouragement was a source of strength for me to complete this project.

I am immensely grateful to **Dr. Syed Adnan Shah**, Assistant Professor, Faculty of Telecommunication and Information Engineering, University of Engineering and Technology, Taxila, Pakistan, for giving me valuable inputs regarding MATLAB coding and results presentation. His vast experience of the field has assisted me in a very sophisticated manner right to the completion.

I am thankful to **Dr. Kashif Sattar**, Assistant Professor, IT department, Arid University Rawalpindi, Pakistan, for his support in preparation of manuscript for journal submission.

My sincere appreciation goes to **Dr. Ali Daud**, Associate Professor, Department of Computer Science and Software Engineering, International Islamic University, Islamabad, Pakistan, for providing fruitful information about different journals and submission guidelines.

My sincere gratitude is to **Dr. Junaid Ali Khan**, Professor/Dean Faculty of Basic sciences, Department of Computer Science and Engineering, HITEC University, Taxila, Pakistan, whose emphasis for excellence kept me focused on to my project and helped me complete it in time. I thank him for providing the necessary resources and facilities to carry out this project in time.

I would also acknowledge the active support, I got from all my class fellows, especially, Mr. Muhammad Awais, Mr. Muhammad Faheem and Mr. Muhammad Farooq for providing feedback on methodology and results to carry out this project in time.

Finally, I am extremely gratified and indebted to my family members, especially, my parents and elder brother **Mr. Atif Ilyas** (late), for their enormous support, persistent encouragement and earnest prayers throughout this project.

Dr. Asif Mehmood
UET Taxila, 2025

Abstract

Modeling and simulation of human brain with diverse neurocomputational features is a challenging task. To perform biologically meaningful brain simulation, biologically comprehensive and computationally simple model of neuron is required. State of the art models in literature are either complex in terms of biological details or exhibit limited neurocomputational features. The essential part of information processing in brain is concerned with diverse neurocomputational features and bidirectional communication between brain and organs. In this work a unified model of excitable cells is proposed. The model contains the dynamics of neurotransmitters to replicate the enriched neurocomputational features and adrenergic receptors to handle the bidirectional communication between brain and organs. A network of 2191 fully connected neurons, as per the dimensions of dataset, is simulated and performance of proposed model is compared with Generalized Leaky Integrate and Fire (GLIF) model, Multi-scale Adaptive Threshold (MAT) model, and Quadratic Integrate and Fire (QIF) model. It is observed that proposed model is 86% efficient in terms of coincidence factor when compared with GLIF 69%, MAT 73%, and QIF 77%. In terms of firing rate coefficient, prediction accuracy of proposed model is 83% against GLIF 55%, MAT 61%, and QIF 67%. The model extended to the neural network of human brain level containing 100 billion neurons by assuming the neural response in digital form. This assumption reduced the memory requirement of simulation to 13 gigabytes. The model applied to the cells of heart and successfully replicated the electrical activity of cardiac myocyte of different species. A network of 1000 fully connected neurons and cardiac myocytes simulated, and electrical activity is recorded. From electrophysiological data of cardio-neural network simulation, heart rate variability is predicted. This study provides the modeling and simulation phase of brain-heart interface to predict morbidity at early stages. The recent advancements in nano-electronics will make is possible to develop brain-heart interface as nano-chip implant in subject to monitor and control the brain-heart interplay through electrophysiological signals.

Keywords: Spiking neural network · Hybrid excitable cell model · Action potential · Adaptive threshold · Cardiac myocyte · Brain–heart interface

Thesis at a Glance

2191
mouse visual-cortex neurons used for validation

86 %
coincidence factor (GLIF 69, MAT 73, QIF 77 %)

83 %
firing-rate coefficient (GLIF 55, MAT 61, QIF 67 %)

100 B
neurons simulated on a desktop computer

13 GB
memory for a brain-scale, bit-coded network

8
species whose cardiac action potentials are reproduced

Contents

- Publications ii
- Acknowledgment iii
- Abstract iv
- List of Figures ix
- List of Tables xiii

1 Introduction 1

1.1 Background . . . 2
1.2 Motivation . . . 5
1.3 Problem Statement . . . 6
1.4 Aims and Objectives . . . 6
1.5 Contributions . . . 7
1.6 Thesis Structure . . . 7
1.7 Summary . . . 8

2 Literature Review 9

2.1 Neural Structure . . . 10
2.1.1 Membrane . . . 10
2.1.2 Axon . . . 11
2.1.3 Threshold . . . 11
2.1.4 Dendrite . . . 11
2.2 Action Potential . . . 11
2.3 Synaptic Transmission . . . 14
2.4 Neural Networks . . . 14
2.5 Neural Computation . . . 15
2.6 Summary . . . 16

3 Methodology 18

3.1 Hybrid Excitable Cell Model . . . 19

3.2 Neurocomputational Features . . . 22

3.2.1 Regular Spiking . . . 22

3.2.2 Fast Spiking . . . 23

3.2.3 Class-I Excitability . . . 23

3.2.4 Class-II Excitability . . . 24

3.2.5 Intrinsic Induced Bursting . . . 25

3.2.6 Intrinsic Induced Spiking . . . 26

3.2.7 Mixed Mode . . . 26

3.2.8 Phasic Spiking . . . 27

3.2.9 Phasic Bursting . . . 27

3.2.10 Resonator . . . 28

3.2.11 Tonic Bursting . . . 28

3.2.12 Tonic Spiking . . . 28

3.2.13 Spike Frequency Adaptation . . . 29

3.2.14 Spike Latency . . . 30

3.3 Experimental Settings and Dataset . . . 31

3.4 Baseline Approaches . . . 32

3.4.1 Generalized Leaky Integrate and Fire (GLIF) Model . . . 32

3.4.2 Multi-scale Adaptive Threshold (MAT) Model . . . 33

3.4.3 Quadratic Integrate and Fire (QIF) Model . . . 35

3.5 Performance Evaluation Measures . . . 35

3.5.1 Coincidence Factor . . . 35

3.5.2 Firing Rate Coefficient . . . 36

3.6 Summary . . . 37

4 Results and Discussions: Neuron 38

4.1 Cell Level Performance . . . 39

4.2 Network Level Performance . . . 45

4.3 Building Large Scale Model of Human Brain . . . 47

4.4 Limitations . . . 49

4.5 Homogeneous and Heterogeneous Spatial Firing Distribution . . . 51

4.6 Summary . . . 52

5 Results and Discussions: Cardiac Myocyte 53

5.1 Cardiac Myocytes . . . 54

5.2 Cardiac Currents . . . 57

5.2.1 Inward Sodium Current I_{Na} . . . 57

5.2.2 Late Sodium Current I_{NaL} . . . 58

5.2.3 Transient Outward Current I_{to} . . . 59

5.2.4 L-Type Calcium Current I_{CaL} . . . 60

5.2.5 Rapid Potassium Current I_{Kr} . . . 60

5.2.6 Slow Potassium Current I_{Ks} . . . 61

5.2.7 Inward Potassium Current I_{K1} . . . 62

5.2.8 Sodium-Calcium Exchange Current I_{NaCai} . . . 63

5.2.9 Subspace Sodium-Calcium Exchange Current I_{NaCass} . . . 63

5.2.10 Sodium-Potassium Exchange Current I_{NaK} . . . 64

5.2.11 Potassium Background Current I_{Kb} . . . 65

5.2.12 Sodium Background Current I_{Nab} . . . 65

5.2.13 Calcium Background Current I_{Cab} . . . 67

5.2.14 Calcium pump Current I_{pCa} . . . 67

5.3 Calcium Fluxes . . . 68

5.3.1 Calcium Leakage Flux from Network Sarcoplasmic Reticulum J_{leak} . . . 69

5.3.2 Calcium Release Flux from Junctional Sarcoplasmic Reticulum J_{rel} . . . 69

5.3.3 Calcium Flux from Network to Junctional Sarcoplasmic Reticulum J_{tr} . . . 70

5.3.4 Calcium Uptake Flux from Cytosol to Network Sarcoplasmic Reticulum J_{up} . . . 71

5.4 Cardiac Action Potential of Different Species . . . 72

5.4.1 Cardiac Myocytes in Human . . . 72

5.4.2 Cardiac Myocytes in Dog . . . 74

5.4.3 Cardiac Myocytes in Cat . . . 75

5.4.4 Cardiac Myocytes in Zebra-fish . . . 75

5.4.5 Cardiac Myocytes in Guinea Pig . . . 76

5.4.6 Cardiac Myocytes in Rabbit . . . 77

5.4.7 Cardiac Myocytes in Mouse . . . 78

5.4.8 Cardiac Myocytes in Rat . . . 79

5.5 Cardio-Neural Network . . . 80

5.6 Pancreatic Cells . . . 82

5.7 Summary . . . 83

6 Conclusion and Future Directions 85

6.1 From Model to Silicon: the NeuroBit64 Chip Family . . . 86

6.1.1 NeuroBit64: the Brain Chip . . . 86

6.1.2 Organ Variants: Common Architecture . . . 86

6.1.3 NeuroBit64-Cardio: Brain and Heart . . . 88

6.1.4 NeuroBit64-Pancreas: Brain and Pancreas . . . 89

6.1.5 NeuroBit64-Kidney: Brain and Kidney . . . 90

6.1.6 Verification and Size . . . 91

6.1.7 Limitations . . . 92

6.2 Mobile Applications . . . 92

6.2.1 From the Chip to the Phone . . . 92

6.2.2 The Organ Monitor . . . 93

6.2.3 The Body Monitor . . . 93

6.2.4 GlucoSense . . . 93

6.3 Expected Advantages of the Chips and Applications . . . 94

6.4 Future Directions . . . 95

A MATLAB Source Code 98

A.1 Baseline Models and the HEC Model . . . 99

A.2 Neural Ensembles of the Dataset . . . 100

A.3 Coincidence Factor of Individual Neurons . . . 101

A.4 Coincidence Factor of the Trials . . . 103

A.5 Firing-Rate Coefficient . . . 105

A.6 Bit-Matrix Simulation of Large-Scale Networks . . . 106

A.7 Cardiac Action Potential and Adrenergic Neurons . . . 109

A.8 Cardio-Neural Network and Heart Rate Variability . . . 111

› Bibliography 113

List of Figures

1.1 Fixed point neuron (FPN) computation from six neighboring neurons in cubical structure. 4

2.1 Action potential of neuron due to activation of ion channels. 12

2.2 Phase portrait of gating parameter n against membrane potential V. 13

2.3 Action potential generated by Hodgkin and Huxley model. 13

3.1 Functional hierarchy of brain-heart interactions: (a) Communication between brain (excitatory and inhibitory neurons) and heart (α and β-adrenergic receptors) by the autonomic nervous system (sympathetic and parasympathetic). (b) Communication between neuron and cardiac myocyte by electrical spikes. 19

3.2 Relation between membrane potential v (blue) and membrane potential recovery parameter u (red). 20

3.3 Membrane potential simulated by hybrid excitable cell model (blue), threshold (black), and input synaptic current (red). 21

3.4 Regular Spiking neuron in response of constant steady state current. 23

3.5 Fast Spiking neurons fire spikes of high frequency in response of steady state constant current. 24

3.6 Class-I excitability of neural activity is independent of variations in input current. 24

3.7 Class-II excitability of neural activity depends upon input current and can be implemented for prediction of type of input current. 25

3.8 Intrinsic Induced Bursting 25

3.9 Intrinsic Induced Spiking 26

3.10 Mixed mode. 26

3.11 Phasic spiking. 27

3.12 Phasic bursting neuron fires burst of action potential initially followed by regular spiking. 27

3.13 Resonator neuron is activated if the frequency of stimulation is matched with firing frequency of neuron.. 28

3.14 Tonic bursting 29

3.15 Tonic spiking 29

3.16 Spike Frequency Adaptation 30

3.17 Spike Latency neuron resonates after firing spike. 30

3.18 Spikes of dataset of single trial containing matrix of size (2191×217) with 2191 neurons and 217 time bins. 31

3.19 Generalized Leaky Integrate and Fire Model 33

3.20 Multi-scale Adaptive Threshold Model 34

3.21 Quadratic Integrate and Fire Model 36

4.1 (a) Dataset (b) GLIF (c) MAT (d) QIF (e) HEC Model (f) Input current. 40

4.2 Graphical representation of coincidence factor of 10 neurons out of 2191 neurons from first trial of dataset out of 14 trials. 42

4.3 Graphical representation of average value coincidence factor of 14 trials with each trial containing 2191 neurons. 44

4.4 Comparison of baseline models with proposed model in terms of computational complexity. 44

4.5 Graphical representation of firings of 2191 neurons per time bin over 217 time bins for first trial of dataset. 46

4.6 Graphical representation of firing rate correlation coefficient of 2191 neurons averaged over 217 time bins for 14 trials. 47

4.7 Binary representation of 1000×1000 matrix to manipulate 64 million neurons. (a) 1000×1000 matrix (b) Splitting of 1000×1000 matrix with each decimal number into 64 bits binary number. (c) 64 bit binary representation of decimal number. 48

4.8 Simulation results of 100 billion neurons with 100 trillion sparsely coupled synaptic connections. 50

4.9 Neural activity across different brain regions in terms of neurocomputational features of brain with heterogeneous inter regional communication represented by different colours, previously reported for excitatory and inhibitory neurons [71]. 51

5.1 a) Action potential pulses generated by single cardiac myocyte (blue) b) Neuron activated by beta-adrenergic receptors (black) c) Neuron stimulated by alpha-adrenergic receptors (magenta) d) Potential pulse generated by release of beta-adrenergic receptors e) Potential waveform activated by release of alpha-adrenergic receptors f) Electrical pulses generated by cardiac myocytes to activate the neural network of brain (red). 56

5.2 Flowchart describing the communication pathway between brain and heart via autonomic nervous system to control the functionality of both organs. 57

5.3 Inward sodium current 58

5.4 Late sodium current 59

5.5 Transient Outward Current 60

5.6 L-Type Calcium Current 61

5.7 Delayed Rapid Potassium Rectifier Current 61

5.8 Delayed Slow Potassium Rectifier Current . . . 62
5.9 Inward Potassium Rectifier Current . . . 62
5.10 Sodium-Calcium Exchange Current . . . 63
5.11 Sodium-Calcium Exchange Current of Subspace Component . . . 64
5.12 Sodium-Potassium Exchange Current . . . 65
5.13 Potassium Background Current . . . 66
5.14 Sodium Background Current . . . 66
5.15 Calcium Background Current . . . 67
5.16 Calcium pump Current . . . 68
5.17 Calcium Leakage Flux from Network Sarcoplasmic Reticulum (NSR) . . . 69
5.18 Calcium Release Flux from Junctional Sarcoplasmic Reticulum (JSR) . . . 70
5.19 Calcium Flux from Network Sarcoplasmic Reticulum (NSR) to Junctional Sarcoplasmic Reticulum (JSR) . . . 71
5.20 Calcium Uptake Flux from Cytosol to Network Sarcoplasmic Reticulum (NSR) . . . 71
5.21 Action potential of human cardiac myocyte . . . 73
5.22 Action potential of dog cardiac myocyte . . . 74
5.23 Action potential of cat cardiac myocyte . . . 75
5.24 Action potential of zebra-fish cardiac myocyte . . . 76
5.25 Action potential of guinea pig cardiac myocyte . . . 77
5.26 Action potential of rabbit cardiac myocyte . . . 78
5.27 Action potential of mouse cardiac myocyte . . . 79
5.28 Action potential of rat cardiac myocyte . . . 80
5.29 (a) Cardio-neural network of 1000 neurons synchronized with upstroke of 1000 cardiac myocytes. (b) Collective behavior of neural network to estimate the occurrence of heartbeat. (c) Inter-beat-interval-difference calculated from inter-beat-interval. . . . 81
5.30 (a) Pancreatic α-cells, when the glucose level is low, the threshold of the cell is constant. (b) Pancreatic β-cells, when glucose level exponentially approaches the peak. (c) Pancreatic δ-cells, when glucose level exponentially decays from the peak. . . . 82

6.1 Mask layout of NeuroBit64-S in the SkyWater 130 nm process (3,172 standard cells, design-rule and layout-versus-schematic clean). The chip has not been fabricated. 87
6.2 Connections of an organ chip. The brain chip and the organ chip exchange activity over three wires; the organ chip reports to a phone or computer through a Bluetooth serial module. Broken lines: the bit stream for a 2.4 GHz transmitter is generated, but the transmitter itself is not designed. . . . 87

6.3 NeuroBit64-Cardio, normal rhythm (software model that is bit-identical to the Verilog description). (a) Action potential of one myocyte. (b) Population spikes of the β-adrenergic and α-adrenergic neurons; their distance is the action potential duration. (c) Upstrokes of the 1000 myocytes travelling through the 32 conduction groups. 89

6.4 NeuroBit64-Pancreas, healthy islet. (a) Firing rates of the three cell populations at fixed glucose concentrations. (b) Glucose concentration read back by the chip from the firing rates against the concentration given to it. 90

6.5 NeuroBit64-Kidney. (a) Loss of nephrons: the total filtration stays normal up to a loss of 50 % because (b) the remaining nephrons filter more and the renin level rises. (c) Total filtration (blue) and renin level (orange) of the healthy kidney at different perfusion pressures. 90

6.6 Block floorplans of the three organ chips, to scale (55 % utilization assumed). These are planning drawings, not mask layouts. 91

6.7 The applications at the width of a phone screen, running the software models of the chips. Left: Body Monitor in the conduction-block scenario. Centre: Organ Monitor, heart chip in normal rhythm. Right: Organ Monitor, kidney chip with 25 % of the nephrons switched off. 94

List of Tables

3.1 Values of model parameters for simulation of neurocomputational features of neurons. 23

4.1 Comparison between hybrid excitable cell model, quadratic integrate and fire model, multi-scale adaptive threshold model and generalized leaky integrate and fire model. 40

4.2 Numerical values of coincidence factor for 10 neurons out of 2191 neurons of first trial of dataset out of 14 trials. 42

4.3 Average numerical values of coincidence factor of 14 trials with each trial containing 2191 neurons. 43

4.4 Mean firings of 2191 neurons averaged over 217 time bins for each trial of dataset. 46

5.1 Brief description of model parameters, notations and symbols used for cardiac myocytes 55

5.2 Values of Model Parameters (MPs) for simulation of cardiac myocytes of different species 72

5.3 Values of model parameters for simulation of pancreatic cells 83

6.1 The NeuroBit64 family. Cell counts and areas are synthesis results for the SkyWater 130 nm standard-cell library; those of the organ variants are for the complete chips with 1000 units. 88

6.2 Comparison of the Verilog descriptions with the software models. 91

CHAPTER 01

Introduction

> *The brain is a world consisting of a number of unexplored continents and great stretches of unknown territory.*
>
> — Santiago Ramón y Cajal

QUESTIONS TO EXPLORE

1. Why is simulating a brain of one hundred billion neurons and one thousand trillion synapses still out of reach?
2. Why are existing neuron models either too complex to scale or too simple to be biologically faithful?
3. How can an adaptive threshold and fixed-point neuron computation simplify large-scale simulation?
4. What does this thesis set out to achieve, and what does it contribute?

IN THIS CHAPTER

1.1	Background	2
1.2	Motivation	5
1.3	Problem Statement	6
1.4	Aims and Objectives	6
1.5	Contributions	7
1.6	Thesis Structure	7
1.7	Summary	8

This chapter is devoted to the basic concepts related to neuron. From a biological point of view, neurons are considered as excitable cells with chemical interactions in terms of ion channels. On the other hand, the neuroscience community treats neuron as computational unit of information processing of brain. The purpose of this chapter is to highlight the actual picture of neuron by looking through the prism of intrinsic features. Therefore, readers will be able to understand the ion channel dynamics as well the effect of ion channels on neuron behavior. This chapter will briefly explore the concepts related to firing of neurons, threshold generation, dynamical behavior of neuron in terms of ion channels and threshold variability.

1.1 Background

Modeling and simulation of a human brain containing one hundred billion neurons and one thousand trillion synapses is a challenging task for the neuroscience community. After conducting rigorous experiments and exhaustive simulations over the years, researchers can understand the animal behavior associated with individual brain region (intra-regional). However, communication across different brain regions (inter-regional) during complex tasks related to vision, speech and motor control are still unknown [1]. To understand such complex tasks performed by a brain, researchers require a unified model for whole brain that can capture animal behavior with biological parameters. Such models would be significantly important about the evaluation of animal behavior in terms of simulation rather conducting expensive, time consuming and ethically prohibited experiments [2].

Modeling and simulation of the human brain with complex biological parameters in real-time is a challenging task. A biologically realistic neuron contains cell body, dendrites and axon for computation and communication with other neurons. Neuron captures input from other neurons or sensory receptors through dendrites. The signals captured by dendrites are superposed and a composite input signal is generated [3]. Depending upon the strength of input signal, cell body initiates a nerve impulse that propagates through axon to the target neuron or cluster of neurons with similar features, called neural network. From modeling perspective of neuron, it is important to understand the dendritic superposition of different weak signals into a composite signal. There are several chemical and electrical phenomena behind this superposition such as potential gradient, ion channel dynamics and electrostatic interactions between ions [4]. The cell membrane of neuron also plays a vital role in action potential generation process. The action potential of single neuron is combined with other similar featured neurons to form a cluster of neurons as neural network. These neural networks are specialized for certain tasks depending upon the nature of input and corresponding output.

Computational neuroscience is concerned with the numerical methods to investigate the underlying processes for spike generation. The electrophysiological features of neurons in terms of spike train determines the information processing mechanism. The combination of spike train by application of input varies between neurons even possessing identical electrophysiological and morphological features. Thus, to understand information processing mechanism of brain, intrinsic properties of neuron are also of key importance. Computational models that can predict current voltage response of neuron are derived from conductance-based models. Hence, treating the neuron in a manner where response is predicted by overall assumption of conductance, introduces error in neural response. The prime reason of error in such models is the negligence

of neural intrinsic properties and their integration at large scale network level. Therefore, building large scale neural network by implementing conductance based computational models provides poor prediction of experimental data [5].

In order to discover the computational aspect of brain, it is necessary to device an accurate model of neuron at cell level and its integration at large scale network level. Therefore, neural dynamics in terms of anatomy and electrophysiology, must be integrated in mathematical format. For this purpose, the current voltage response of neurons is taken as dataset and corresponding model parameters are predicted. This method is suitable to develop the neural model in a more sophisticated and scientific manner to converge the spike train generated by biological neuron. The internal dynamics of neuron in terms of ion channels or voltage activated gates is estimated by threshold [6]. The dynamic of voltage gates strongly depends upon the ionic concentration, nature of stimulation, voltage activated receptors, neurotransmitters and temperature. These factors determine the threshold variability of the neural system. Thus, even two neurons with identical anatomical and morphological features behaves in a quite different manner for identical inputs [7].

Recent years have witnessed a boom of massive creations, demanding efficient models of neural networks for better utilization. With the success of deep learning, Artificial Neural Networks (ANNs) have gradually become the mainstream paradigms for large scale simulation models of brain. While ANNs can achieve delightful performances, problems concerning computational and structural complexity hinder the further application of these models in real-world scenarios. The event-driven Spiking Neural Networks (SNNs) can process temporal information with high speed and low energy consumption, which provide a promising alternative for real-time scenarios [8]. To make a paradigm for brain simulation and restore success in machine learning areas, we need to propose a unified excitable cell model that can comprehensively utilize the rich neural temporal information.

In past few years, many attempts were made to model the large scale neural network of a brain quantitatively and qualitatively on neural simulators (NEST, NEURON, Brain2) and hardware accelerators such as SpiNNaker. The models utilized behind the simulation to generate spike are either constant threshold or computationally complex to simulate the large-scale population of neurons. Quantitative models contain the set of nonlinear differential equations describing the dynamics of resistance, capacitance and ion channels in terms of intracellular and extracellular interactions. Computational complexity and homogeneous intra-regional limitations make such models prohibitive for large scale simulation of brain. On the other hand, qualitative models are based upon neurocomputational features without considering the dynamics of complex parameters. This greatly reduced computational cost in terms of floating operations per second (FLOPS). However, heterogeneous inter-regional communication across all brain regions still not supported by these models [9]. Cross regional communication is a very important aspect of brain's simulation without which we can understand the limited features of cognitive abilities of a brain through senses. Therefore, the primary focus of this study is the homogeneous intra-regional and multiple, heterogeneous inter-regional communication between neurons of different parts of brain in terms of neurocomputational features [10].

To solve this problem, static model parameters with adaptive threshold are assumed and introduced in integrate and fire model. The motivation behind static parameters is drawn from the fact that at large scale network level time constant of network almost remains constant [11]. The ion channel dynamics is like switching semiconductor diode with adaptive threshold

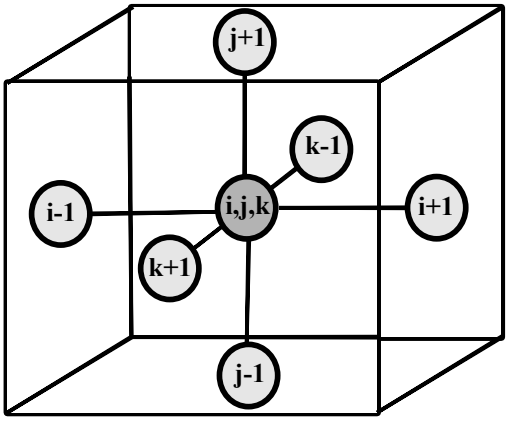


Figure 1.1 Fixed point neuron (FPN) computation from six neighboring neurons in cubical structure.

potential. Thus, exponential curve of threshold can be approximated with straight line over a small differential portion of the curve as the time constant of network is large enough as compared to an individual cell [12]. For this reason, adaptive threshold of a neuron is approximated with constant voltage drop model of semiconductor diode within small linearly differential portion [13].

Fixed Point Neuron (FPN) computation is introduced in which randomly generated noisy input, is available to each neuron with one thousand synapses. Fixed point neuron (FPN) computation from six neighboring neurons in cubical structure, where central neuron is labeled as (i, j, k) is assumed at the center of cube and remaining six neurons are labeled as $(i + 1, j, k)$ and $(i - 1, j, k)$ along x-axis, $(i, j + 1, k)$ and $(i, j - 1, k)$ along y-axis and $(i, j, k + 1)$ and $(i, j, k - 1)$ along z-axis. Each neuron can receive synaptic input current from one thousand neurons (not drawn here), thus each FPN computation is done by seven thousand synaptic connections, out of which only strengthen weight have been plotted according to Hebbian learning rule. Instead of computing dendritic responses from all neurons, soma computes the response based upon noisy input from six (fixed points) immediate neighboring neurons (six neurons for 3D visualization and four neurons for 2D) by finite difference method as illustrated in Figure 1.1. Six fixed points have been assumed by considering cubical neural distribution within brain. This assumption further simplifies the computation associated with calculation of neuron index. The approach can be equally valid for deep neural networks where each neuron out of six can be taken from different cortical layers [14].

Our approach is different from state-of-the-art models in three aspects.

- Qualitative features of action potential are considered instead of quantitative features and points of activation are traced by straight line. The inspiration behind this assumption comes from the fact that at large scale network level time constant is very large and exponential curve of threshold can be approximated by straight line. Therefore, asymptotic behavior of limit cycle attractor that defines hyperpolarization of neural activity, converge faster than the exponential model [15].

- Fixed point computation adopted at network level by considering six immediate neighboring neurons instead of evaluating response from all the neurons connected with arbitrary neuron. The motivation behind this assumption is the 3D distribution of brain cells. For sake of simplification cubical structure have been taken instead of drawing actual brain surfaces.

This approach can also be equally valid by simulation of brain network with respect to six cortical layers having cross regional communication [16].

- Adaptive feature of threshold of neuron is integrated at network level, previously available in adaptive models at cell level only. State of the art models are the manifestation of Hodgkin and Huxley model by assuming constant threshold. However, after recording neural response experimentally against noisy input synaptic current, adaptive threshold is universally accepted by neuroscience community [17].

1.2 Motivation

Machine learning algorithms are gaining popularity in the field of computational neuroscience to investigate qualitative models for extraction of animal behavior from experimental recordings of electrophysiological dataset [18]. While performing large scale brain simulation, two significant features of qualitative model are: (i) model must be able to replicate enriched neurocomputational features of biological neuron in response to identical current and (ii) model is capable of homogeneous intra-regional and heterogeneous inter-regional communication of different parts of brain. Unfortunately, qualitative models deviate from in-vivo and in vitro recordings when stimulated by time varying current. A good qualitative model must exhibit almost all the known neurocomputational features of biological neuron as the Izhikevich model do. Hence, this research will provide alternate solutions to the computer scientists to process neural data more effectively without understanding the complex biological processes behind the behaviour [19].

Simulation of human brain level large-scale neural network, containing one hundred billion neurons in terms of firing patterns, is a challenging task. State of the art models are either complex at single cell level and cannot be extended to the network level or applicable to certain brain region only. Thus, the modeling and simulation of network of human brain with one hundred billion neurons and one thousand trillion synapses is possible only if we propose a unified neuron model applicable to all brain regions. This statement can be confined to two research questions:
i. How to define the neuron model applicable to all the brain regions in terms of all the known anatomical and neurocomputational features?
ii. What is the simplest possible morphology of neurons to construct the neural network of one hundred billion neurons?
The most significant contribution of this research is studying the dynamics of the human brain at single cell level as well as at network level with cross regional communication. The motivations of study can be summarized as follows:

- Simplified model of neuron containing homogeneous intra-regional and heterogeneous inter-regional communication between different parts of a brain.
- Simulation of most important neurocomputational features related to intelligence and cognition, with biologically realistic parameters.
- Extension of the proposed model on large scale brain network of the order of one hundred billion cells with one thousand trillion synaptic connections.

- Spatial representation of different brain regions with respect to neurocomputational features.

1.3 Problem Statement

Modeling and simulation of human brain with complex biological parameters and enriched neurocomputational features is a challenging task. To perform biologically meaningful brain simulation, biologically comprehensive and computationally simple model of neuron is required. State of the art models in literature are either complex in terms of parameters or limited to homogeneous intra-regional connections. Therefore, to understand the information processing mechanism of brain, we need to bridge the functional interactions between brain and organs by unification of intra-regional and inter-regional features, by biologically detailed computational model. In this work, a unified model of excitable cells is proposed that can represent the electrophysiological details of neurons and cardiac myocytes.

1.4 Aims and Objectives

The aim of this research is to derive a simple configuration of neurons with other excitable cells to understand the bidirectional communication between brain and organs in real time. The objectives of current research are listed below:

- To perform the key indicators of neural configuration in terms of connections, communication protocols and governing computational model. Performance can be evaluated at two levels of abstraction: i. Cell level ii. Network level. The best model must be efficient at both levels at the same time.

- To simulate the human brain containing one hundred billion neurons with one thousand trillion synapses. Simulation of such a large-scale neural network with Hodgkin and Huxley model (HH model) require exascale computers capable of executing quadrillion operations per second. The largest neural simulation conducted so far contains one billion neurons, 1% of human brain. The simulation performed on Japanese flagship $K-computer$ (derived from Japanese word *kei* meaning quadrillion 10^{16}) by implementing tile partitioning method [20]. Although electrical spikes are simulated by neurons effectively, however, still we are far away to know how the brain functions. Even the most complex and comprehensive models of the brain leave out many details.

- To perform the biologically meaningful simulation of the human brain by integrating the appropriate model parameters related to complex biological processes. There are many details of biological processes that cannot be integrated practically into any model of neuron. Such details include the receptor binding, intracellular and extracellular interactions. Therefore, researchers can never gather the data associated with such interactions for the human brain down to the molecular level. However, by applying some algorithms some features of brain can be extracted under certain constraints as imposed by for large scale brain models [21].

- To improve the speed of learning in brain simulation by approximating the complex biological processes with computationally simple model parameters. Unfortunately, there is no

technology that can run large scale simulation faster than real time. Therefore, the synaptic connections developed in human brain defined by well-known rules such as Hebbian learning rule may be more complex than expected [22].

- To integrate the neural dynamics of different brain regions and extract the behavior. In past decades many neural models were developed limited to certain brain regions. A model representing the neuron of brain overall is not explicitly available [23]. Thus, to model the functions performed by the human brain, smaller models of brain regions need to be integrated into large scale networks of brain. Combining top-down and bottom-up models will essentially achieve speed, flexibility and efficiency, however, it is challenging because we lack a strong theory, how the brain process information [24].

1.5 Contributions

The major contributions of this study are summarized as follows:

- Simplified model of neuron containing computational efficiency as well as biological plausibility is proposed. The model extended to the different excitable cells and their electrical behavior is predicted accurately.
- Simulation of most important neuron features with minimum possible and biologically realistic parameters is performed. The model is applicable to simulate the electrical activity of cardiac myocytes and pancreatic cells.
- Extension of proposed model on large scale brain neural network to study the behaviour of different organs and response of brain to deliver the control signal.
- Identification of different features from electrical response of neural network to predict heart rate variability.

1.6 Thesis Structure

The research work presented in this document comprises of six chapters as follows:

- Details of literature review of computational models of neuron is provided in chapter 2. Our approach of modeling the dynamics of neuron is based upon leaky integrate and fire model, therefore, we restricted our discussion around the variants of computational models derived from leaky integrate and fire neuron. In this chapter, ion channel dynamics is discussed in detail with respect to molecular, intracellular and extracellular interactions. The effects of ions transportation across neural membrane in terms of membrane potential fluctuations is described in detail.
- Chapter 3 is dedicated to explain the step by step development of proposed model. Mathematical equations and simulation are provided in this chapter to cover the basic concepts related to computational neuroscience. The ion channel dynamics with mathematical formulation is provided along with simulation results. The dataset and their explanation is provided along with baseline approaches. Formulations of statistical analysis at cell level and network level are illustrated in this chapter.

- In Chapter 4 results of the study are elaborated. The model performance analyzed in terms of coincidence factor at cell level and in terms of firing rate coefficient at network level. Proposed model compared with augmented multi-scale adaptive threshold model, generalized integrate and fire model and quadratic integrate and fire model.
- In Chapter 5 proposed model is applied on heart cell to illustrate the electrical activity of cardiac myocytes. A network of 1000 cardiac myocytes are coupled with a neural network and heart rate variability is accurately determined.
- In Chapter 6 conclusion of study and future directions are provided in detail.

1.7 Summary

In this chapter a brief overview of large-scale brain simulation framework is provided. Computational neuroscience community mainly concerns neural circuits and their electrical activity towards animal behavior. Extracting animal behavior from composite neural response is challenging task due to superposition of neural activity at small signal level. State of the art models developed to study the electrical response of neurons in terms of spikes are either complex that cannot simulate large population of neurons or oversimplified that cannot capture the biophysical details of neurons. Therefore, we need to develop a computationally simple and bio-physically comprehensive model of neuron that can exhibit enriched neurocomputational features and biological plausibility of real neuron.

KEY TAKEAWAYS

- Large-scale brain simulation needs a neuron model that is **biologically comprehensive** yet **computationally simple**; current models offer one or the other.
- The adaptive threshold is approximated by a straight line over small intervals, in the spirit of the constant-voltage-drop model of a semiconductor diode.
- **Fixed Point Neuron (FPN)** computation evaluates each neuron from its six immediate neighbours in a cubic lattice instead of from all of its synapses.
- The goal is a **unified excitable cell model** that covers both neurons and cardiac myocytes, so that brain–organ communication can be simulated.

CHAPTER 02

Literature Review

> *If I have seen further it is by standing on the shoulders of giants.*
>
> — Isaac Newton

QUESTIONS TO EXPLORE

1. How do the membrane, axon, threshold and dendrites decide when a neuron fires?
2. How do ion channels generate an action potential, and how did Hodgkin and Huxley capture it mathematically?
3. Why do spiking neural networks promise faster, lower-energy computation than conventional artificial neural networks?
4. What do the integrate-and-fire, FitzHugh–Nagumo and Izhikevich models gain, and what do they lose?

IN THIS CHAPTER

2.1 Neural Structure 10
2.2 Action Potential 11
2.3 Synaptic Transmission 14
2.4 Neural Networks 14
2.5 Neural Computation 15
2.6 Summary 16

Computational neuroscience deals with the neural circuits and their computational features by modeling and simulation of brain. Neurons in the brain are covered by semipermeable membranes on which the active ion transportation generates membrane potential to determine the firing of a spike. Considering the various transportation mechanisms, biological neurons can be abstracted for corresponding information processing. This chapter will cover the basic concepts related to neural structure and information processing mechanism briefly along with state-of-the-art computational models.

2.1 Neural Structure

The basic concept of information processing of brain starts with the understanding of neuron. Neurons are the basic building blocks of the brain, specialized for information processing through spikes. A typical neuron receives input current from a few to ten thousand neurons through treelike structure, dendrite. The input current approaching to neuron is superposed to transform a composite current, sufficient to activate the voltage sensitive gates. These gates act like an amplifier to enhance the level of input in the form of transformed potential. This transformation of potential is abrupt change in membrane potential, therefore referred to as spike or action potential.

A typical neuron contains three components: cell body, dendrites and an axon. Neurons capture the stimulus from its surroundings through dendrites, process the information in cell body and transmit the processed signal through axon to other neurons. The signal processing in biological neurons takes place by different ion channels and neurotransmitters. The type of ion channel and neurotransmitter determines the nature of information to be processed [25]. Before a neuron is fired, the concept of threshold is important to understand. The threshold of neuron is the potential barrier that the input current must hold to cross the potential barrier. In other words, threshold is the potential barrier that an ion must hold to cross the neural membrane. Once the ions can cross the neural membrane, the spike is generated that can propagate through an axon.

The firing of neuron not only depends upon threshold, but also on the frequency and amplitude of stimulus. In biological neurons whenever frequency of input current is below the resonance frequency of neuron, determined by time constant of neuron, spike is not initiated. Such neurons are referred to as resonators and are important during natural language processing. The spiking neuron model appropriately balance biological reality with computational feasibility, whereby the respective advantages of integration and resonance mechanism that can be fully utilized when processing temporal signals [26]. A significant distinction between integrator and resonator neurons lies in their sub-threshold dynamics in response to spike stimuli. The two neurons are activated in quite different ways, having discriminating spike temporal preferences. Neurons are intensity-sensitive and likely to be activated by spikes with shorter intervals, as well as timing-sensitive with spikes separated by intervals around its refractory period [27].

2.1.1 Membrane

Neural membrane is composed of phosphoric and fatty acid with voltage sensitive gates integrated in it. The purpose of these gates is to allow the ion transportation under certain conditions. These voltage sensitive gates are also referred to as ion channels. Neural membrane keeps the neuron intact with sodium, calcium, potassium and chloride ions which are responsible for generation of nerve impulse. Neural membrane is semi-permeable for these ions

and allows the transportation of ions under certain potential. Depending upon the value of stimulus, a potential difference across neural membrane is created. If the potential difference approaches the threshold potential of ion channels, a nerve impulse is initiated that travels along axon to trigger the other neurons [28].

Initially, the membrane potential of neuron remains at -80 millivolts, termed as resting membrane potential. Due to transportation of leakage ions, resting potential fluctuates slightly between -80 millivolts to -60 millivolts. Whenever external stimulus approaches the neural membrane, resting potential tends to increase towards the threshold potential -40 millivolts. If resting potential is increased to approach threshold, a spike of potential is fired. This spike of potential is called nerve impulse.

2.1.2 Axon

Axon contains narrow and long micro tubules which transmit the ions and neurotransmitters. Under resting condition, fluid inside these micro tubules remains static. Whenever, nerve impulse is generated, due to electrostatic interactions, fluid inside micro tubules travels according to the type of electrostatic force. Therefore, the purpose of axon is to transport information in the form of neurotransmitters to the target neuron, also referred as postsynaptic neuron [29].

2.1.3 Threshold

The minimum membrane potential change that causes neuron fire is called threshold. A typical neuron contains four types of ions: sodium, potassium, calcium and chloride ions. The first three ions are positively charged while the fourth is negatively charged. Inside neuron potassium ions are bounded by negatively charged protein. Outside neural membrane sodium and calcium ions are in higher concentration. This constitutes an electro-chemical equilibrium across the neural membrane. Whenever, stimulation current approaches the neural membrane, depending upon positive ion concentration outside the cell creates a potential barrier. This potential barrier is referred to as a threshold. The strength of threshold varies depending upon the extracellular and intracellular ionic concentration [30]. Therefore, in biological neurons, no hard limit of threshold can be defined. However, for simplicity we assume the average value of threshold when a large number of neural firing recorded.

2.1.4 Dendrite

The cell body of neuron contains large number of fibers called dendrites. The dendrites of a typical neuron range from 1,000 to 10,000 depending upon its activity. A neuron with larger synaptic plasticity contains a greater number of dendrites. The purpose of dendrites is the formation of neural network when information is provided in the form of electrical potential. The point of contact between two neurons where dendrites meet is called synapse. Whenever, a neuron is activated, it transmits its information to other neurons through these synapses [31]. Depending upon types of synapses, neurons can be excitatory or inhibitory. If synapse increases the activation of target neuron, it is referred as excitatory neuron and vice versa.

2.2 Action Potential

The waveform of electric potential along axon due to activation of neural membrane is called action potential (AP). The membrane potential is generated by the interactions of sodium and

potassium ions across the neural membrane [32]. Neuron models are important due to two aspects (activation function and simulation) with respect to their vast applications in the field of medical and engineering. Simulations of different parts of brain in real time as in various simulators used in field of medical technology as well as in the field of engineering such as neural networks, deep learning, and recognition involves the neuron models [33]. Nature of problem and accuracy of results defines the neuronal model to be used. In engineering problems, we need neuron models for training networks and finding the values of target variables under certain conditions while in medical field neuron models are used to study the behavior of neuronal systems under certain conditions defined by the medicines injected.

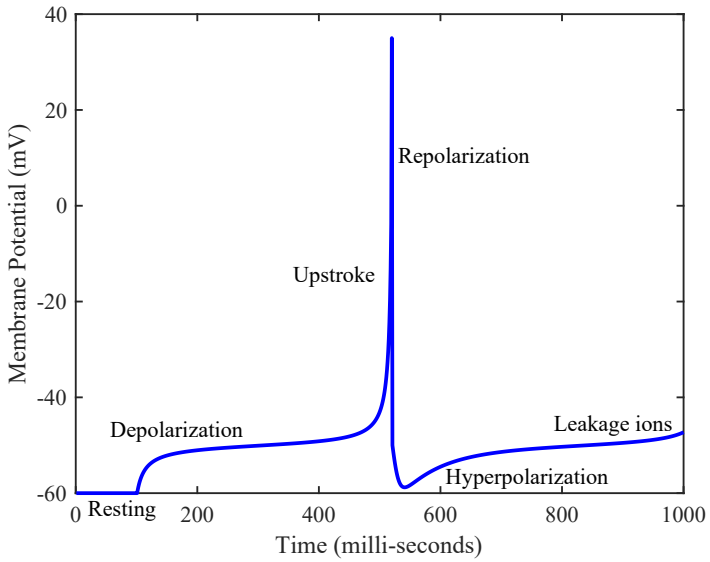


Figure 2.1 Action potential of neuron due to activation of ion channels.

Neurons are the excitable cells that can receive a brief input pulse and produce an amplified signal of action potential as depicted in Figure 2.1. The electrical activity of neurons is based upon four types of ions sodium (Na^{+1}), potassium (K^{+1}), calcium (Ca^{+2}) and chloride (Cl^{-1}). The extracellular medium contains high concentration of sodium and chloride ions while intracellular contains high concentration of potassium and negatively charged protein molecules. These protein molecules are the receptors of voltage (voltage activated gates) and can be activated by a certain voltage level thus are called ion channels. They allow certain type of ions to flow across the membrane at potential called activation potential and stops the flow at another particular potential called inactivation potential [34]. For example, the protein molecules that allow sodium to cross the membrane are called sodium channels activate at -30mV and inactivate at 40mV. The dynamics of ion channels can be expressed mathematically as:

$$\frac{dn}{dt} = (1-n)\alpha_n - n\beta_n \tag{2.1}$$

Where n is ion channel gating parameter. The parameters α_n and β_n can be defined as:

$$\alpha_n = 0.01\frac{10-V}{exp(\frac{10-V}{10})-1} \tag{2.2}$$

$$\beta_n = 0.125exp(\frac{-V}{80}) \tag{2.3}$$

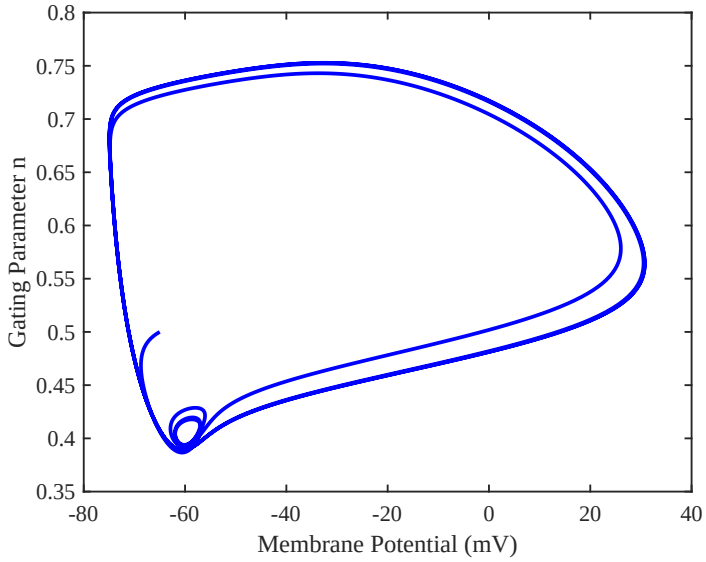


Figure 2.2 Phase portrait of gating parameter n against membrane potential V.

The phase portrait of gating parameter against membrane potential is plotted in Figure 2.2. Initially, when neuron is in a resting state, only leakage ions are capable of transportation across the membrane. Under resting state, all inward ionic currents that causes membrane depolarize, is balanced by the outward ionic currents that hyper-polarize the neural membrane [35]. This causes small perturbations of potential across membrane which are shown by the smaller circles in Figure 2.2. This state of the neuron is referred to as equilibrium or quiescent or stable state. Whenever, a strong stimulation current approaches the neural membrane, the stability of neural membrane shifts towards positive direction. This increases the activity of gating parameter n and more ions transported across the membrane [36]. As a result, a spike of potential is generated that travels across the axon to the postsynaptic neurons.

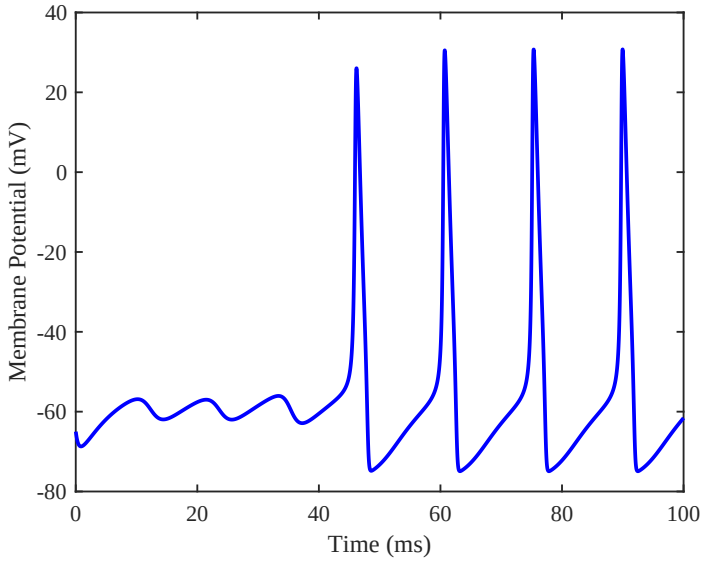


Figure 2.3 Action potential generated by Hodgkin and Huxley model.

In the middle of twentieth century, the most comprehensive neuron model was developed by Andrew Hodgkin and Alan Huxley known as Hodgkin and Huxley model (HH model). This

model is considered as standard in the field of computational neuroscience [37]. HH model defines the neuron as:

- Differentiator with certain values of resistance and capacitance
- Voltage regulated gates called ion channels with activation at certain voltage levels
- Thresholds at which neuron get fire
- Obeys the differential equation with linear terms involving $\frac{dv}{dt}$ and v.
- An amplifier

Mathematically, nerve impulse generation can be approximated by Hodgkin and Huxley model as:

$$\frac{dV}{dt} = \frac{1}{C}[I(t) - g_{Na}(E - E_{Na}) - g_k(E - E_K) - g(E - E_L)] \tag{2.4}$$

Where V is membrane potential, t is instant of time, C is membrane capacitance, I is input synaptic current, g_{Na} is conductance of sodium ion channels, g_k is conductance of potassium ion channels, g is conductance of leakage ion channels, E_{Na} is potential of sodium ion channels, E_k is potential of potassium ion channels, E_L is potential of leakage ion channels [38]. The waveform of action potential generated by HH model is manipulated in Figure 2.3.

HH model equation is a nonlinear differential equation with gating parameters which makes the equation very complex to solve it analytically, moreover numerical solutions are computationally very complex even for simulating few neurons we require super-computing and cannot be translated on hardware in the form of circuit.

2.3 Synaptic Transmission

Neural information is the most complicated and sophisticated entity in the study of information processing mechanism of the brain. The synaptic transmission of neuron depends upon governing ion channels, neurotransmitters and adrenergic receptors. In static condition, neural membrane offers high resistance and acts as capacitor to store electric charge. Whenever a stimulus approaches neural membrane, inward movement of sodium ion increases the membrane potential towards positive side of action potential. This increase in potential reaches its apex at 40 millivolts. At this point potassium channels are open. As a result, outward flow of potassium drops the membrane potential towards negative side of action potential. Thus, is transportation of sodium and potassium ions are responsible for the generation and propagation of synaptic transmission in the form of action potential through axon [39].

2.4 Neural Networks

Artificial neural networks (ANNs) have made great progress in the past decade or so. They have shown excellent results in information processing of various modalities and even exceeded the accuracy of human recognition in some fields. However, since the high-precision model of the ANN model needs to be obtained at the cost of high energy consumption, its deployment on edge devices has been greatly hindered. Spiking neural networks (SNNs) are neural networks inspired by biological neurons. Compared with traditional artificial neural networks, they can

provide lower energy consumption and faster inference speed on neuromorphic hardware. SNN obtains information by transmitting spikes through synaptic connections between neurons. The membrane potential information is stored inside a single neuron. When the membrane potential accumulates to a threshold, it sends spikes to the lower-layer neurons and resets them. Since the spike of a neuron can only have two states: firing or not, this binary information has more advantages in energy consumption and can be inferred quickly on neuromorphic hardware [40].

In fact, unlike ANN, which can update the weight information of the model through gradient backpropagation to train the neural network, SNN is affected by signal discontinuity and non-differentiable spikes, which makes training an SNN model relatively difficult. Currently, the mainstream methods of obtaining a trained SNN model mainly use the surrogate gradient method and the synaptic plasticity method to directly train the SNN model, or by converting a trained ANN model into an SNN model. The common disadvantage of these two methods of directly training SNN models is that there is a large overhead in computational complexity and training time during training [41]. The SNN model obtained in this way usually relies on extremely long inference time steps to match the accuracy of the source ANN model. In this method, there is a trade-off between inference time step and accuracy, and in order to achieve high accuracy, extremely long inference time will still affect the practical application of SNN. After that, the proposal of normalization factors, threshold balancing and other methods greatly improved the accuracy of SNN models at low time steps. At the same time, considering the various sources of conversion errors in ANN-to-SNN, better results are also obtained by modifying the source ANN model activation values and then performing conversion. However, the problem of SNN inference latency caused by longer time steps still exists, and the performance gap with ANN still needs to be solved [42].

Therefore, this work proposes an event-driven method based on adaptive threshold potential. This method regards the single release of the neuron at a certain time stamp of the spiking neural network for the special event and relies on this event to end the inference towards final prediction. In this way, the redundancy of time step in the traditional method of judging based on the average firing rate in the total time step is reduced, and the inference time step is shortened.

2.5 Neural Computation

Neural computation in the brain takes place with propagation of nerve impulses. A simplified form of neuron model is integrated and fire model. It follows differentiator property, thresholds and linearity of $\frac{dv}{dt}$ and v makes it possible to design circuit as hardware, however there is no information of ion channels and amplification. As a result, model is not capable of producing enriched features of neuron. FitzHugh-Nagumo (FHN) model is good approximation of Hodgkin and Huxley model containing tunnel diode as threshold. However, it violates the basic property of neuron equation, the linearity in terms of $\frac{dv}{dt}$ and v, rather it possesses v^3. The Izhikevich model is the reduction of FHN model near the bifurcation and contains the term v^2 instead of v. Hence, these models are good in terms of producing firing patterns of neuron as well as enriched behaviors but theoretically, there exists gap to be covered as proposed in Hodgkin and Huxley model [43].

A good simplified neuron model can be obtained by combining few properties of each model.

For example, we can pick the resistance capacitance property from integrate and fire model, diode from FHN model and computational simplicity from Izhikevich model. Of course, such a model would be the most convenient in terms of theoretical background as well as computational efficiency. Izhikevich model, being one of the most important qualitative models, is efficient to replicate almost all neurocomputational features of spiking neurons in response to constant input current. This model is simple in terms of mathematical formulation and can be extended at large scale brain neural network level. Although, Izhikevich model is computationally efficient (exhibit almost all known neurocomputational features with fewer parameters), yet it is poor predictor of spike timing in the presence of correlated noise (time varying stimulus) as observed in biological neural network of brain. To understand the animal behavior extracted from a computational model, we need to extend the model at different brain regions in the presence of neural correlated noise. Unfortunately, this feature is not explicitly available in Izhikevich model that can perform homogeneous intra-regional and heterogeneous inter-regional simulation of brain in time varying input current environment [44]. Thus, the focus of this study includes the large-scale simulation of brain neural network by time varying stimulus, covering the different brain regions simultaneously.

The recent advancements in computational algorithms and specialized hardware designed to simulate the large-scale models of brain are gaining attention of neuroscience community. Such advancements include large-scale brain simulators like NEST, NEURON, Brain2, The Virtual Brain etc. These simulators are based upon realistic neural networks, however, support only a handful population of neurons. The synaptic connection hierarchy and memory limitations to store the neural data of current and previous synapse, for next iteration are the main challenges to be resolved. On the other hand hardware architecture includes GPU, FPGA and neuromorphic chips like SpiNNaker are specialized for fast neural computations, however, functionality of each processor independently require synchronization challenges of the synaptic data.

The neurocomputational features of neuron and behavior is very important in case of decision making phenomenon, as there is small fraction of neurons responsible for decision making observed in basal ganglia. Yet, their behavior cannot be ignored in the presence of one million firings of cortical neurons versus one firing of basal ganglion cell. Unfortunately, such models are not explicitly available that can illustrate the different regions of the brain and communication between them simultaneously. Hence, modifications in existing models can reproduce the neurocomputational features of different brain regions.

2.6 Summary

In this chapter basic properties of neuron and framework of building large-scale neural network is provided. A typical neuron is made up of semipermeable membrane that can transport certain ions all the time. These ions are called leakage ions. Leakage ions are responsible for sub-threshold oscillations. Under resting state, intracellular fluid contains potassium ions and extracellular fluid contains sodium ions in high concentration. The ion channels that keep these ions intact are sodium channels and potassium channels. These channels are made up of protein molecules carrying negative charge of strength -2. The strength of the major ions that are responsible for action potential, can be manipulated as sodium ions (Na^{+1}), potassium ions (K^{+1}), chloride ions (Cl^{-1}) and calcium ions (Ca^{+2}). These ions remain either in intracellular fluid or extracellular fluid depending upon the potential of neural membrane.

Once the potential of neural membrane is disturbed by external stimulus, transportation of ions takes place across membrane.

KEY TAKEAWAYS

- A neuron fires when stimulation lifts its membrane potential from rest across the threshold set by its ion channels.
- The **Hodgkin–Huxley** model is the reference standard, but its non-linear gating equations are far too costly for networks of billions of cells.
- **Spiking neural networks** transmit binary events, which saves energy, but they are harder to train than conventional ANNs.
- The **Izhikevich** model reproduces most firing patterns cheaply but predicts spike timing poorly under time-varying, noisy input. That is the gap this thesis addresses.

CHAPTER 03

Methodology

> *All models are wrong, but some are useful.*
>
> — George E. P. Box

QUESTIONS TO EXPLORE

1. How can a single set of equations describe both neurons and cardiac myocytes?
2. What roles do the adaptive threshold, neurotransmitters and adrenergic receptors play in the Hybrid Excitable Cell (HEC) model?
3. Which fourteen neurocomputational firing patterns can the model reproduce, and with which parameters?
4. How is accuracy measured, both for single cells and for the whole network?

IN THIS CHAPTER

3.1 Hybrid Excitable Cell Model 19
3.2 Neurocomputational Features 22
3.3 Experimental Settings and Dataset 31
3.4 Baseline Approaches 32
3.5 Performance Evaluation Measures 35
3.6 Summary 37

In this chapter we review the neurocomputational features of cortical neurons and build the generalized model of spiking excitable cells. The governing procedure is inspired by biological neurons by integrating the detailed computational models. In past decades, conductance-based models and computational models were distinguished by their accuracy and complexity of implementation. However, in this chapter we tried to bridge the gaps between conductance-based models and computational models.

3.1 Hybrid Excitable Cell Model

The electrical response of excitable cells is predicted by the spikes generated inside the cell membrane that propagates through axons to other cells. In current study our focus is limited to neurons and cardiac myocytes. The neural response of neuron is denoted by V_N and cardiac myocyte by V_C.

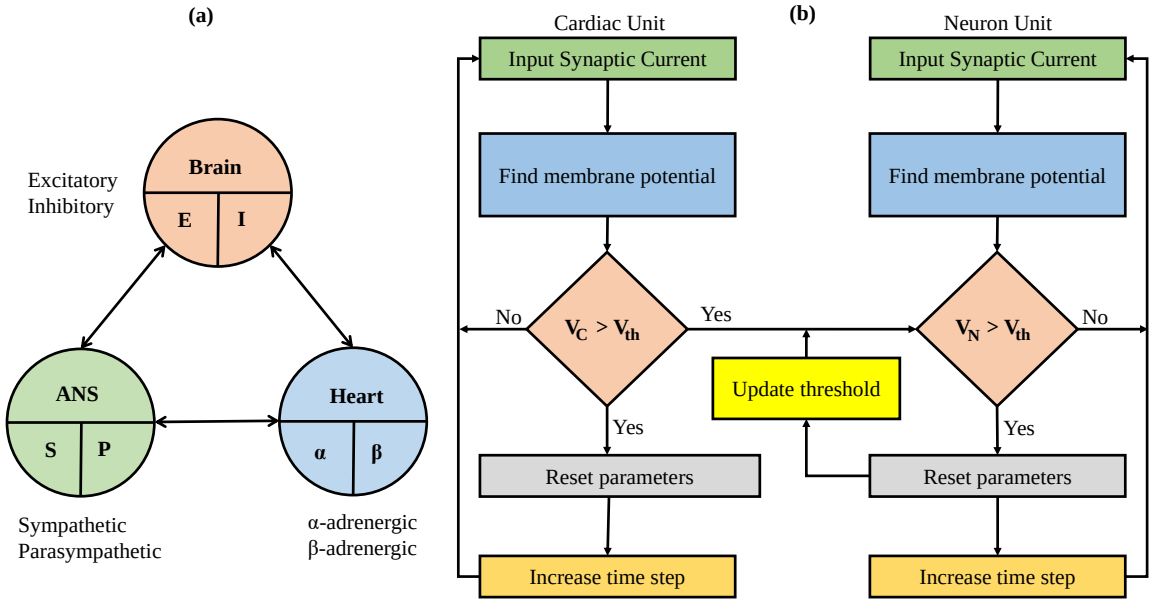


Figure 3.1 Functional hierarchy of brain-heart interactions: (a) Communication between brain (excitatory and inhibitory neurons) and heart (α and β-adrenergic receptors) by the autonomic nervous system (sympathetic and parasympathetic). (b) Communication between neuron and cardiac myocyte by electrical spikes.

The functional hierarchy of proposed model to describe the brain-heart interface is illustrated in Figure 3.1. Figure 3.1(a) elucidates the interaction between the brain and heart via the autonomic nervous system (ANS). The two-way arrow represents a bidirectional communication signal, sharing information between organs. In the brain, two variants of neuron, excitatory and inhibitory were simulated, while for ANS sympathetic and parasympathetic neurons were simulated, and finally, in the heart, α-adrenergic and β-adrenergic receptors (variants of adrenaline and nor-adrenaline hormones) dependent cells were simulated. Figure 3.1b depicts the interaction between neuron and cardiac myocyte by action potential pulses V_N and V_C respectively. Whenever cardiac myocyte fires action potential V_C, depending upon firing frequency (tachycardia or bradycardia), α-adrenergic or β-adrenergic receptors are activated which are associated with hormonal variants of adrenaline and nor-adrenaline. These

receptors fire neurons in ANS and feedback current is communicated to the brain. Thus, control signals are generated by the brain and ANS to control the heart rate via α-adrenergic and β-adrenergic receptors. The hybrid nature of excitable cell comes from the fact that model can reproduce the firing patterns of excitable cells. The important aspect of excitable cells is threshold variability. Unlike the Izhikevich model, excitable cells hold variable thresholds. Moreover, neurotransmitters and adrenergic receptors play a vital role in spike generation. The membrane potential generated by hybrid excitable cell model in response to the input current I can be expressed as:

$$\tau v^{'} = k(v - V_r)f(v - V_{th}) - u + RI \tag{3.1}$$

Where τ is membrane time constant (product of membrane resistance and capacitance) $\tau = RC$, v is membrane potential with initial condition $v(0) = V_r$, V_r is resting membrane potential, $^{'}$ represents first order derivative with respect to time, k is constant to control the strength of slope of membrane potential, f is firing parameter to control the frequency of firing of excitable cell, V_{th} is threshold potential, u is membrane potential recovery parameter after spike is fired, R is membrane resistance and I is input synaptic current. The membrane potential recovery parameter u can be defined as:

$$\tau u^{'} = a(bv - u) \tag{3.2}$$

Where a and b are constants that define the slope of membrane potential recovery parameter u towards positive and negative sides of threshold respectively. The initial condition of membrane potential recovery parameter is $u(0) = d$, called the step size of u towards membrane recovery potential. The waveform of membrane potential v is depicted in Figure 3.2 by blue solid line, while membrane potential recovery parameter u is manipulated by red solid line. It is clear from Figure 3.2 that every time when spike is generated, membrane potential recovery parameter u also generates spike, that gradually decay depending upon the values of a and b. The value of u is feedback negatively to membrane potential v to reset its value after spike is fired as illustrated in Equations 3.1 and 3.2.

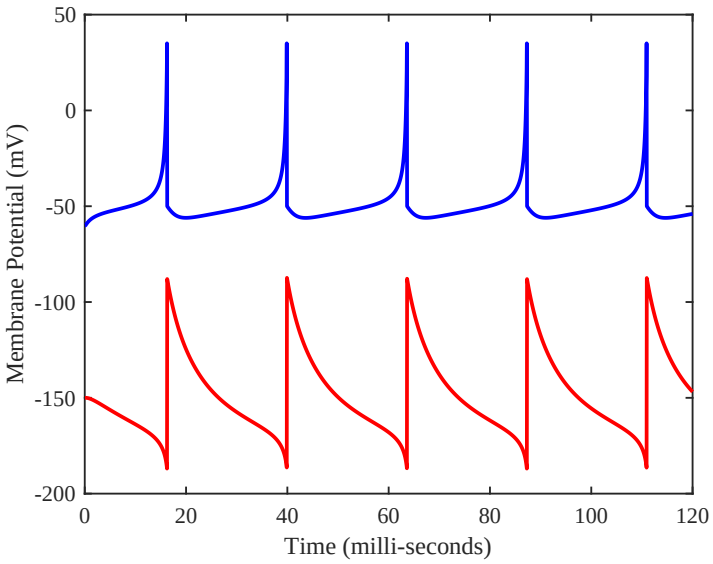


Figure 3.2 Relation between membrane potential v (blue) and membrane potential recovery parameter u (red).

The effect of neurotransmitters and adrenergic receptors on synaptic current can be expressed

as:

$$I_x = \bar{g}_x(\upsilon - V_x)e^{(t_s - t)/\tau_x} \tag{3.3}$$

The description of parameters in Equation 3.3 is:
υ = Membrane potential
V_x = Gating potential
$\bar{g}_x$ = Mean gating conductance
t_s = Index of most recent spike
τ_x = Neurotransmitter and hormonal time constant
The numerical values of parameters $\bar{g}_x$ and V_x are assumed stationary in current study for simplicity purpose, however, the values of these parameters are time varying in neural systems. Readers interested to find details of these parameters are encouraged to consult [45]. The after-spike reset values of membrane potential are:

$$\text{If } \upsilon \geq V_{th}\ ; \ \text{ then } \upsilon = \begin{cases} V_p & \forall\ t \\ V_r & \forall\ (t+1) \end{cases} \tag{3.4}$$

$$V_{th} = Ae^{(t_s - t)/\tau} - \theta \tag{3.5}$$

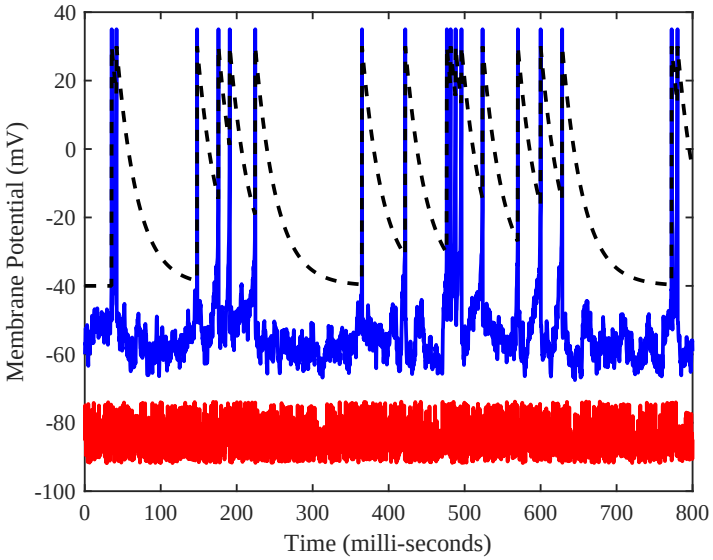


Figure 3.3 Membrane potential simulated by hybrid excitable cell model (blue), threshold (black), and input synaptic current (red).

To find the membrane potential, by implementing Equations 3.1, 3.2, 3.3, 3.4 and 3.5, Euler method is utilized (Algorithm 1). The mathematical form of forward Euler method can be expressed as:

$$\upsilon(k+1) = \upsilon(k) + h\upsilon'(k) \tag{3.6}$$

Parameters in Equation 3.6 can be manipulated as:
$\upsilon(k+1)$ = Membrane potential for current iteration
$\upsilon(k)$ = Membrane potential of previous iteration
h = Step size in time domain for milli second resolution
$\upsilon'(k)$ = First order derivative of membrane potential with respect to time
The waveform of membrane potential is plotted in Figure 3.3 by blue solid line. The input

Algorithm 1: Hybrid Excitable Cell (HEC) model

Input: $a,\ b,\ d,\ k,\ f,\ V_p,\ V_r,\ V_{th},\ \tau,\ R,\ I$

Output: v

Initialize parameters

for $k \leq n$ **do**

  $v^{'}(k) = 1/\tau(k(v(k) - V_r)f(v(k) - V_{th}) - u(k) + RI(k))$

  $u^{'}(k) = 1/\tau(a(bv(k) - u(k)))$

  $v(k+1) = v(k) + hv^{'}(k)$

  $u(k+1) = u(k) + hu^{'}(k)$

  if $v(k) \geq V_{th}$ **then**

    $v(k) = V_p$

    $v(k+1) = V_r$

    $u(k+1) = u(k) + d$

    update V_{th}

Plot results v

synaptic current is plotted by red solid line and threshold function is plotted by black broken line. Whenever, membrane potential touches the black broken line, a spike of action potential is generated as depicted in Figure 3.3. Readers interested to find the details of model implementation and a detailed description of parameters can consult [46]. It should be noted that for simplicity details of dendrites and multi-compartmental morphology of neuron is ignored. Moreover, time dependent synaptic plasticity of model is incorporated in adaptive threshold that fires the next iteration neuron depending upon the time information of previous spike.

3.2 Neurocomputational Features

Neurocomputational properties of neurons are based upon the patterns of firing according to the input current. In general, neural firing is of two types, spiking and bursting. However, depending upon neurotransmitter nature and adrenergic features, neural responses are listed in Table 3.1 with corresponding parameter values for simulation. The parameters were considered from Izhikevich model and fine tuning carried empirically to match the electrophysiological behavior of neurons.

3.2.1 Regular Spiking

Regular spiking neurons are commonly located in cortex. This type of neurons fire spikes of regular periods under the application of steady state current as depicted in Figure 3.4. The typical values of model parameters for regular spiking neuron are: membrane capacitance C=100; resting membrane potential V_r=-60; sensitivity parameter k=0.7; time scale of recovery parameter a=0.03; sensitivity of recovery parameter b=-1.5; after spike reset value of membrane potential c=-50; after spike reset value of recovery parameter d=100; peak value of spike V_{peak}=35 [47]. The neural activity of regular spiking neurons is illustrated in Figure 3.4.

Table 3.1 Values of model parameters for simulation of neurocomputational features of neurons.

Neurocomputational Features	a	b	V_r	d
Regular Spiking	0.03	-1.5	-50	100
Fast Spiking	0.1	-2	-50	100
Class-I	0.01	-0.01	-55	10
Class-II	0.02	0.26	-65	0.1
Intrinsic Induced Bursting	-0.02	-1	-45	2
Intrinsic Induced Spiking	-0.02	-1	-60	8
Mixed Mode	0.02	0.1	-55	3.5
Phasic Spiking	0.02	0.20	-65	6
Phasic Bursting	-0.02	-2	-55	1
Resonator	0.10	0.26	-60	-1
Tonic Bursting	0.02	0.20	-50	2
Tonic Spiking	0.02	0.25	-65	6
Spike Frequency Adaptation	0.01	0.25	-65	8
Spike Latency	0.02	0.20	-65	6

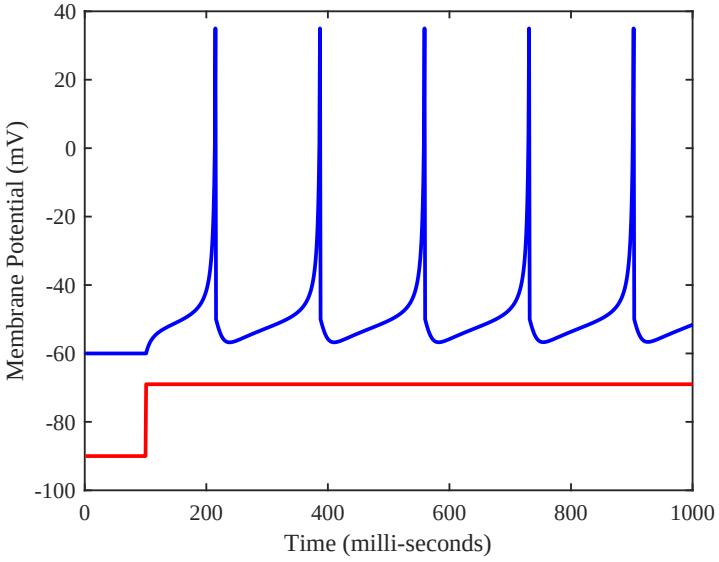


Figure 3.4 Regular Spiking neuron in response of constant steady state current.

3.2.2 Fast Spiking

Fast spiking neurons are similar to regular spiking neurons except for the fast-firing frequency. The time scale of recovery parameter a of fast spiking is of much higher value than regular spiking [48]. The typical values of model parameters for fast spiking neurons are depicted in Table 3.1 and corresponding neural activity is delineated in Figure 3.5. Fast spiking neurons generate high frequency action potential pulses with fast membrane recovery potential. This feature makes fast spiking neurons more precise and accurate towards inhibition and excitation.

3.2.3 Class-I Excitability

Class-I excitable neurons are weakly coupled with stimulation. Any change in stimulation alters the neural response insignificantly. In general, Class-I excitable cells are independent

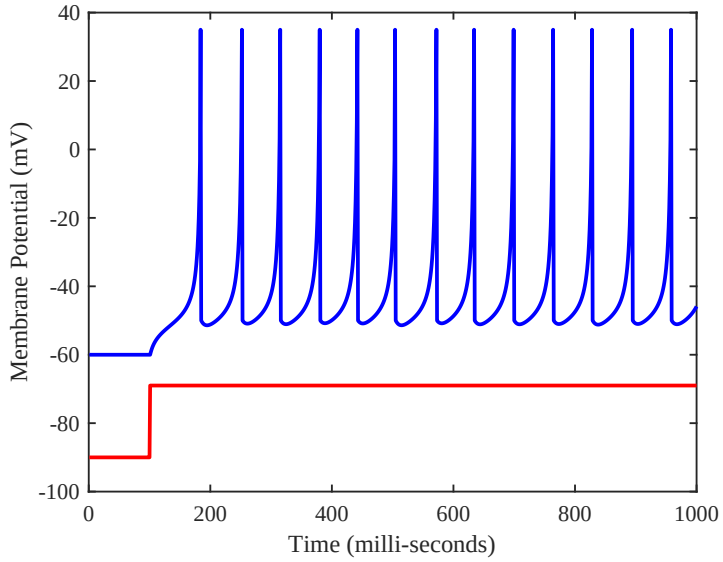


Figure 3.5 Fast Spiking neurons fire spikes of high frequency in response of steady state constant current.

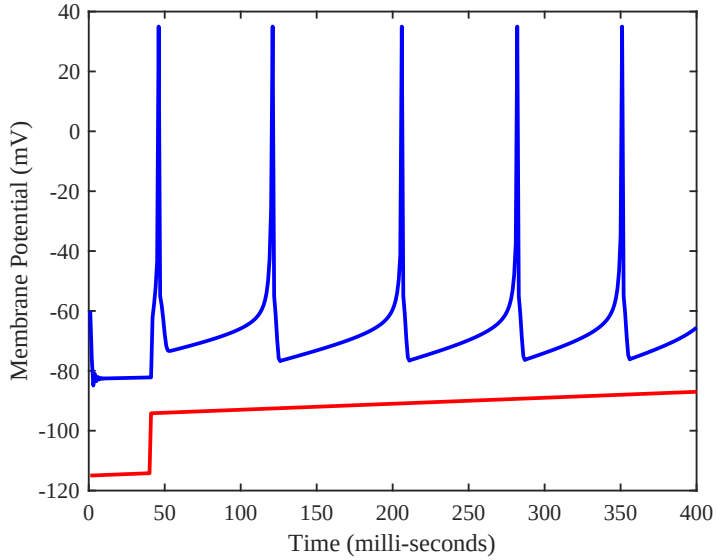


Figure 3.6 Class-I excitability of neural activity is independent of variations in input current.

from the nature of input current. This characteristic makes Class-I excitable cells unique for information processing mechanism [49]. The typical values of model parameters for Class-I excitable neurons are depicted in Table 3.1 and corresponding neural response is manipulated in Figure 3.6.

3.2.4 Class-II Excitability

Class-II excitable neurons are strongly coupled with stimulation. Any change in stimulation alters the neural response significantly. In general, Class-II excitable cells are good predictors of input current. This characteristic makes Class-II excitable cells unique for recognition and classification of input current. The typical values of model parameters for Class-II excitable neurons are listed in Table 3.1 and corresponding neural response is depicted in Figure 3.7.

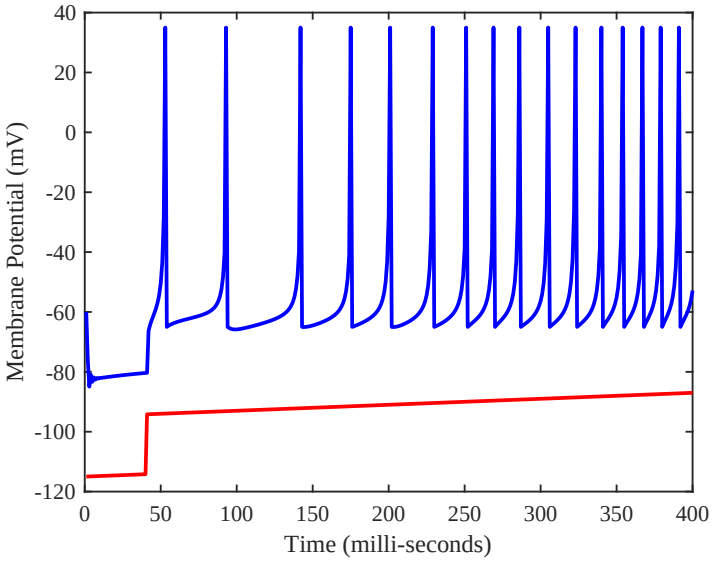


Figure 3.7 Class-II excitability of neural activity depends upon input current and can be implemented for prediction of type of input current.

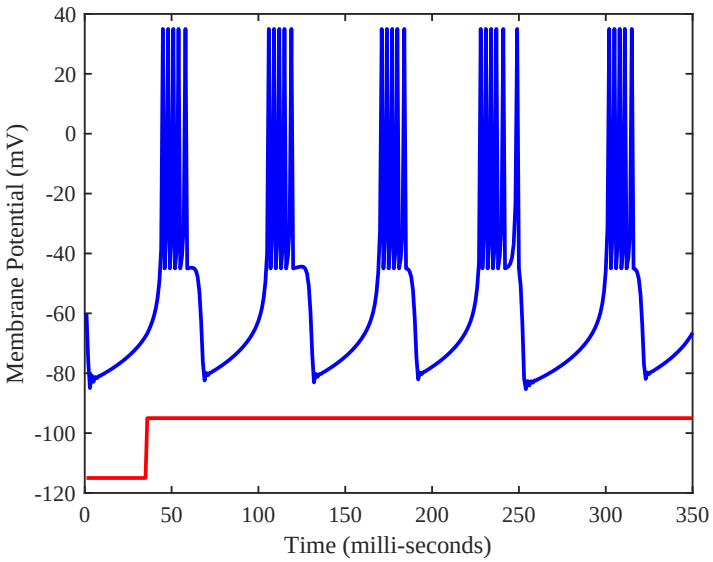


Figure 3.8 Intrinsic Induced Bursting

3.2.5 Intrinsic Induced Bursting

Bursting is an important neurocomputational feature of neurons. In this type of neural activity, very closely spaced spikes are fired followed by a short inhibition interval. Bursting mode of neurons is the fast-paced information processing mode [50]. The typical values of model parameters for intrinsic induced bursting neurons are listed in Table 3.1 and corresponding neural response is depicted in Figure 3.8.

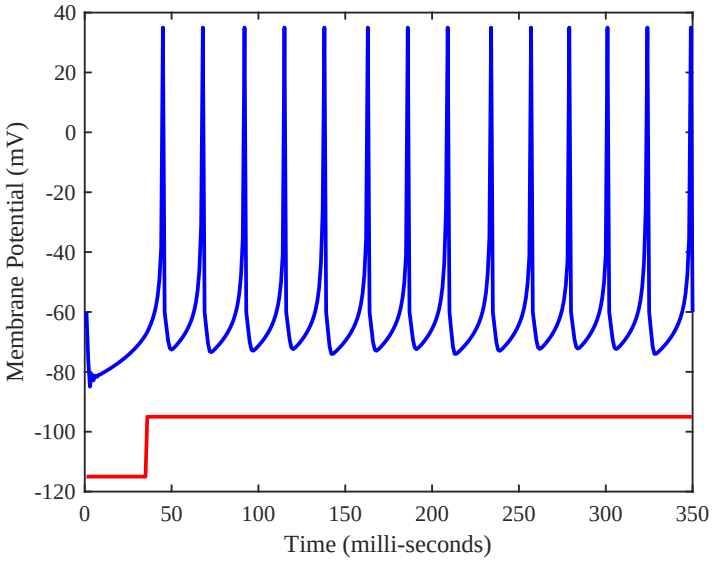


Figure 3.9 Intrinsic Induced Spiking

3.2.6 Intrinsic Induced Spiking

Intrinsic induced spiking mode of neurons is inhibitory mode of neural activity. Unlike fast spiking neurons with are excitatory, intrinsic induced spiking neurons suppress the successor neural activity [51]. The typical values of model parameters for intrinsic induced spiking neurons are listed in Table 3.1 and corresponding neural response is depicted in Figure 3.9.

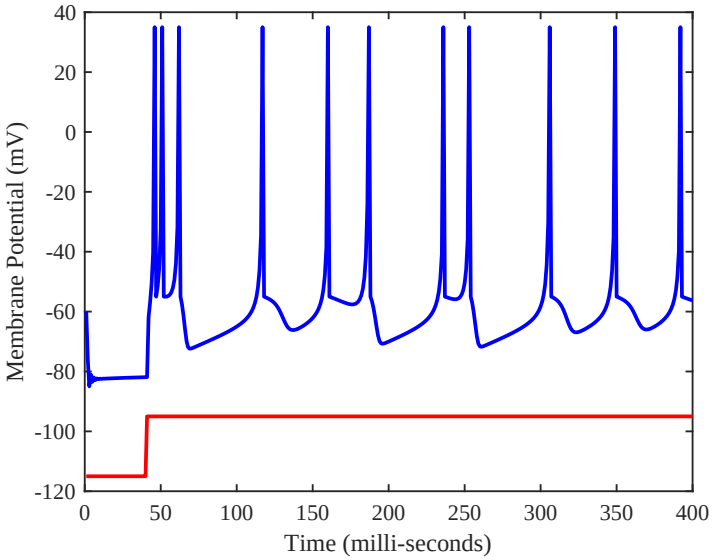


Figure 3.10 Mixed mode

3.2.7 Mixed Mode

An important feature of neural activity is mixed mode. In this type of neural response, neuron fires bursts of spikes followed by a combination of regular spiking and fast spiking alternative mode [52]. The typical values of model parameters for intrinsic induced spiking neurons are listed in Table 3.1 and corresponding neural response is depicted in Figure 3.10.

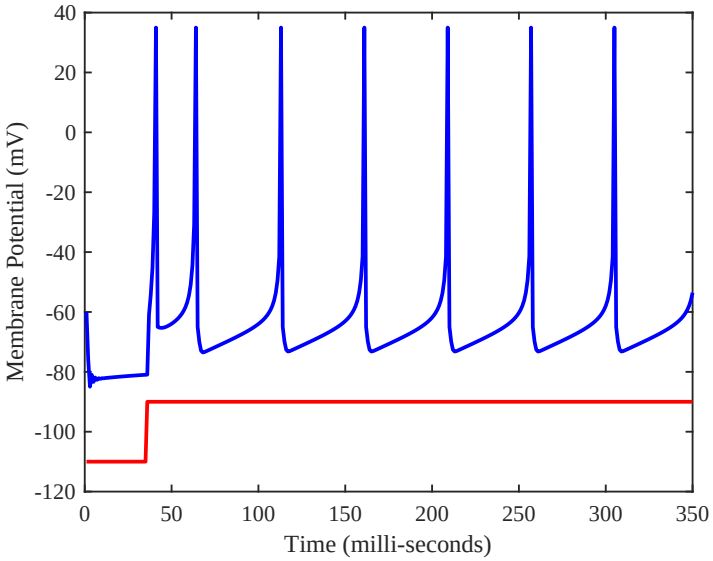


Figure 3.11 Phasic spiking

3.2.8 Phasic Spiking

Phasic spiking neuron starts neural activity from fast spiking followed by regular spiking. The initial fast spiking mode of neural activity is due to threshold variability and negative value of time scale recovery parameter of membrane potential [53]. The typical values of model parameters for phasic spiking neurons are listed in Table 3.1 and corresponding neural response is depicted in Figure 3.11.

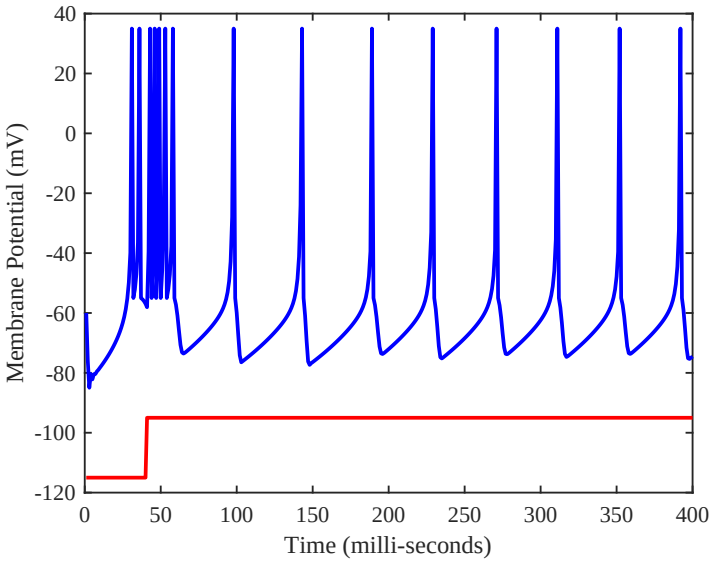


Figure 3.12 Phasic bursting neuron fires burst of action potential initially followed by regular spiking.

3.2.9 Phasic Bursting

Phasic bursting neuron fires burst of spikes at beginning of neural activity followed by regular spiking. The main reason for initial burst firing is the sensitivity of neuron towards intrinsic potential. From basic circuit theory, we know that neuron is differentiator [54]. Any abrupt change in input current causes a significant change in output response. Due to leakage ions

transportation across neural membrane, a leakage ion potential is developed across membrane. This potential combines with the stimulation current and causes one time burst when neuron is activated. The typical values of model parameters for phasic bursting neurons are listed in Table 3.1 and corresponding neural response is depicted in Figure 3.12.

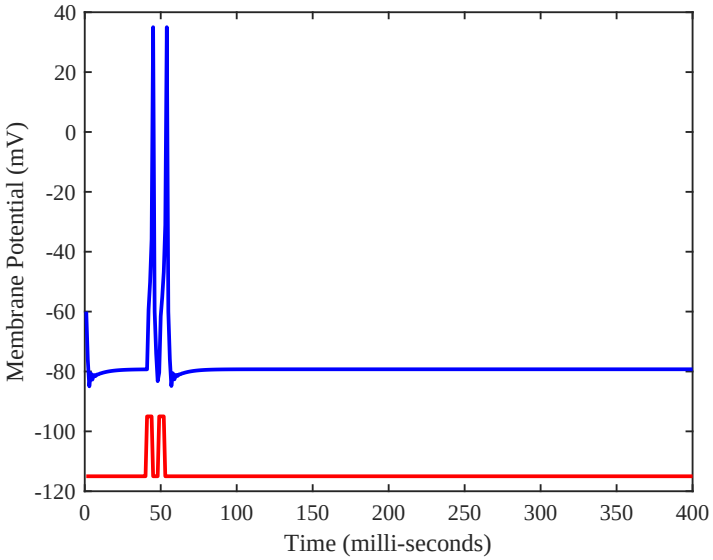


Figure 3.13 Resonator neuron is activated if the frequency of stimulation is matched with firing frequency of neuron.

3.2.10 Resonator

Resonator is the most important mode of neural activity. This mode is related to the frequency of stimulation. In this mode of neural activity, time interval between input current pulses is monitored. If the frequency of stimulation is greater than the firing frequency of neuron, a neural response is initiated. Unlike regular spiking and fast spiking mode of neural activity, resonator is related to the frequency of input current pulses [55]. Whenever input current pulses are closely packed in time domain, the pulses responses are added up and a strong stimulation is generated. This strong stimulation makes the neuron fired depending upon the frequency of stimulation. The typical values of model parameters for resonator neurons are listed in Table 3.1 and corresponding neural response is depicted in Figure 3.13.

3.2.11 Tonic Bursting

Tonic bursting neuron fires bursts of spikes regularly spaced from each other. The main reason for burst firing is the sensitivity of neuron towards intrinsic potential. From basic circuit theory, we know that neuron is differentiator. Any abrupt change in input current causes a significant change in output response. Due to leakage ions transportation across neural membrane, a leakage ion potential is developed across membrane [56]. This potential combines with the stimulation current and causes one time burst when neuron is activated. The typical values of model parameters for tonic bursting neurons are listed in Table 3.1 and corresponding neural response is depicted in Figure 3.14.

3.2.12 Tonic Spiking

Tonic spiking neuron starts neural activity from fast spiking followed by regular spiking. The initial fast spiking mode of neural activity is due to threshold variability and negative value of

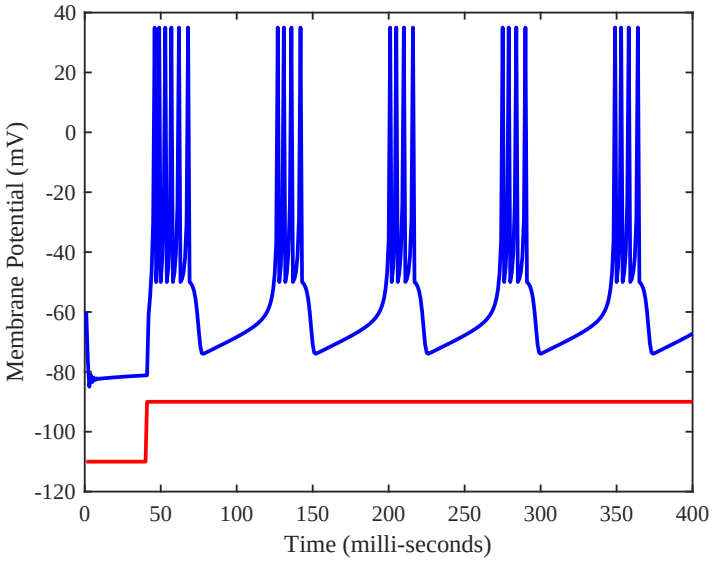


Figure 3.14 Tonic bursting

time scale recovery parameter of membrane potential. The typical values of model parameters for tonic spiking neurons are listed in Table 3.1 and corresponding neural response is depicted in Figure 3.15.

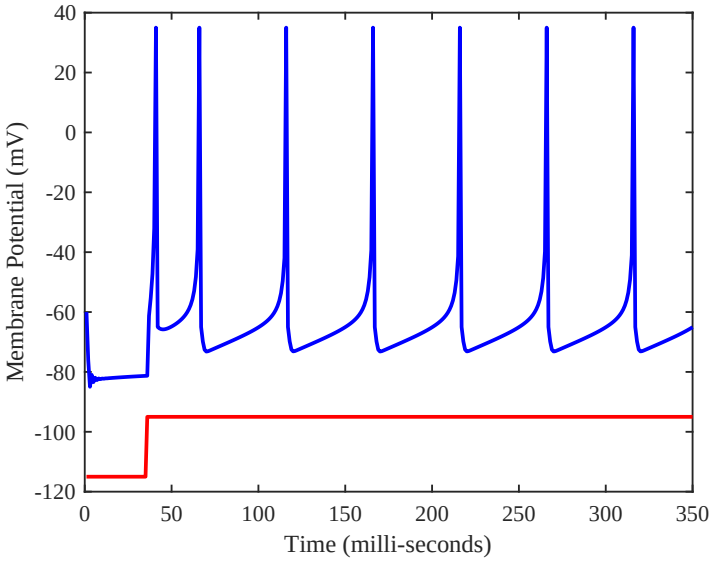


Figure 3.15 Tonic spiking

3.2.13 Spike Frequency Adaptation

Spike frequency adaptation is like tonic spiking mode. The main difference in tonic spiking and spike frequency adaptation is absence of initial fast spiking mode. The spike frequency adaptation neuron starts neural activity from slow spiking mode followed by regular spiking mode with equal intervals of time. The initial fast spiking mode of neural activity is due to differentiator nature of neuron and negative value of time scale recovery parameter of membrane potential [57]. The typical values of model parameters for spike frequency adaptation neurons are listed in Table 3.1 and corresponding neural response is depicted in Figure 3.16.

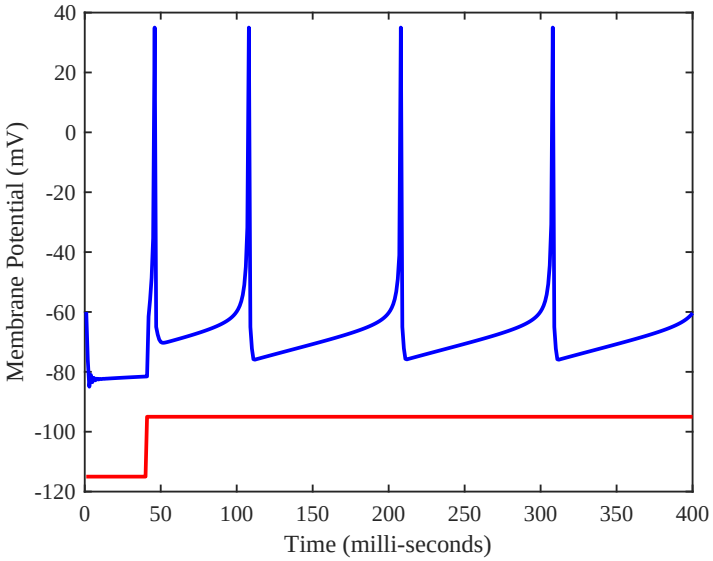


Figure 3.16 Spike Frequency Adaptation

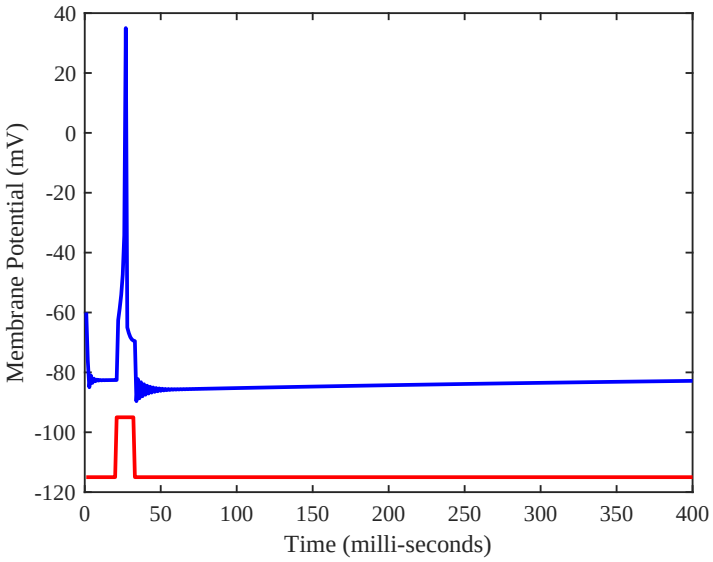


Figure 3.17 Spike Latency neuron resonates after firing spike.

3.2.14 Spike Latency

Spike latency mode of neural firing is like resonator. In spike latency, duty cycle of stimulus plays a vital role. Latency of output impulse depends upon the spread of pulse appearing as input to neuron. Spike latency mode may be positive or negative edge triggered, or level sensitive edge triggered, or edge sensitive level triggered [58]. In particular example provided in Figure 3.17, spike latency neuron is positive edge sensitive, and level triggered due to positive slope of differentiator mode. The typical values of model parameters for spike latency neurons are listed in Table 3.1 and corresponding neural response is depicted in Figure 3.17.

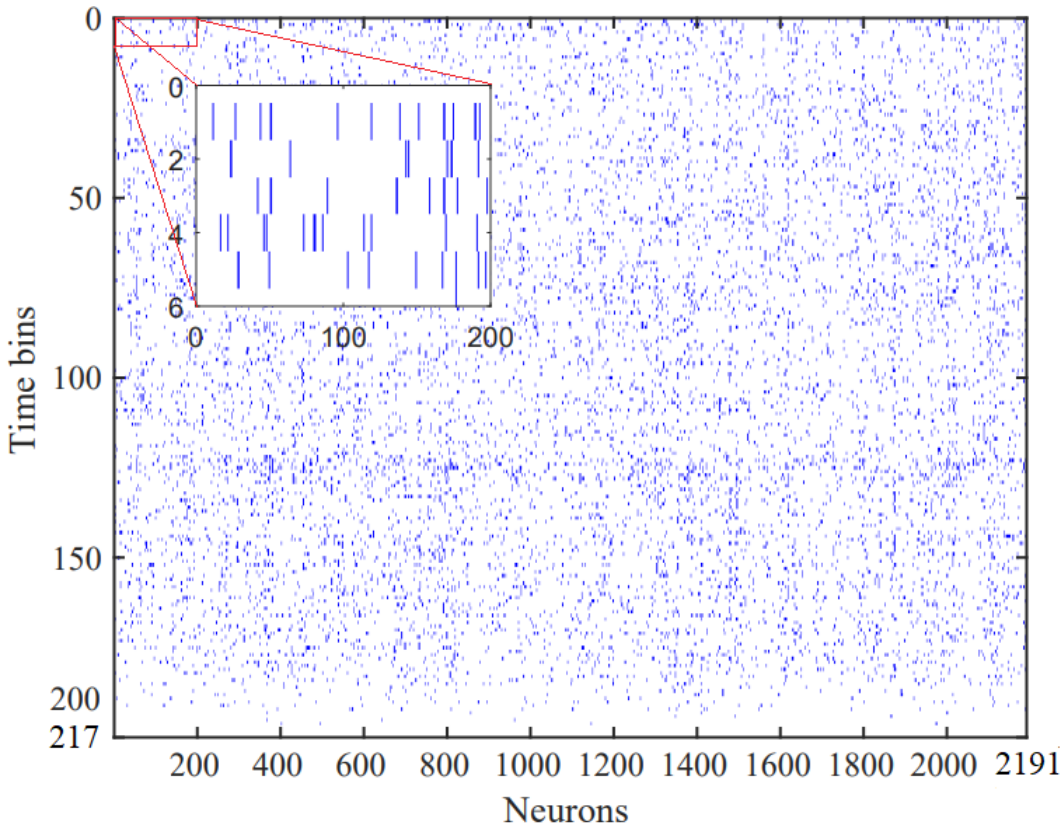


Figure 3.18 Spikes of dataset of single trial containing matrix of size (2191×217) with 2191 neurons and 217 time bins.

3.3 Experimental Settings and Dataset

Dataset contains the electrophysiological recordings of 2191 neurons from mouse visual cortex area. The neurons have been stimulated by optically generated photo-current as input and corresponding response is recorded [59]. The electrophysiological recordings of mouse brain under the action of predefined set of stimuli contain 2191 neurons, 217-time steps and process is repeated for 14 times. The dataset obtained in this way contains three-dimensional matrix with dimensions $N \times T \times TB$.
First dimension N represents number of neurons = 2191 Neurons
Second dimension T represents number of trials = 14 Trials
Third dimension TB represents time bins = 217 Time-bins
Therefore, three-dimensional matrix takes the form $2191 \times 14 \times 217$ with total 6,656,258 entries. To store data in MATLAB variable for processing, each entry requires 64 bits or 8 bytes. Thus, to store the mouse data in memory, we require about 53.3 megabytes of memory. For displaying dataset, we analyzed each entry in time domain to reconstruct spikes from neural ensembles as depicted in Figure 3.18. The vertical lines in Figure 3.18 represents the spike generated by neuron.

3.4 Baseline Approaches

For comparison, we assume spike generation models of the same category, leaky integrate and fire neuron. The variants of leaky integrate and fire neuron include generalized leaky integrate and fire model, multi-scale adaptive threshold model and quadratic integrate and fire model. A brief description of each model is presented below.

3.4.1 Generalized Leaky Integrate and Fire (GLIF) Model

This model contains the set of linear differential equations to estimate the membrane potential. The linearity of model equations and simplicity of computational dependencies of parameters, are key features to extend the model for large scale brain simulation. The membrane potential of GLIF model depends upon the strength of depolarization potential. The dendrites of neuron are assumed in the form of capacitive coupled resistance. This enables us to recognize the GLIF neuron as differentiator. In resting state, large amount of sodium ions is located outside the cell membrane with little concentration of calcium ions. The electrostatic force of repulsion between positively charged sodium and calcium ions constructs a potential barrier [60]. To overcome this potential barrier, a stronger stimulation current is required to depolarize the membrane. The chemical interactions of neuron in terms of potential can be expressed by the depolarization potential V_{dep}. When a brief and strong enough rheobase current, capable of generating a potential greater than potential barrier of neuron established by sodium ions, approaches the dendrites of neuron, protein molecules are dispersed. This dispersion of protein molecules creates enough room for sodium ions to rush into the neuron. As a result, membrane potential rises in positive direction. The protein molecules that provided the path to enter the sodium ions inside the cell are referred to as sodium channels. The membrane potential υ in terms of depolarization potential established by sodium ions, calcium ions and negatively charged protein molecules, can be expressed as:

$$\upsilon' = \frac{1}{C_m}\left(\frac{C_m}{\tau_m}(\upsilon - V_{dep}) - V_{adap}\right) + IR \tag{3.7}$$

The description of parameters in Equation 3.7 is, as follows:
C_m = membrane capacitance
R = membrane resistance
τ_m = membrane time constant
$\tau_m = RC_m$
I = strong stimulation current that can cause membrane depolarization
V_{adap} = adaptation potential due to electrostatic interactions between positively charged ions and negatively charged protein molecules.
The adaptation potential V_{adap} comes into action due to the recovery of membrane potential after spike is initiated. When sodium ions rush into neuron, potential increases in positive direction. This causes the potassium channels to release the potassium ions from inside the cell outside due to electrostatic force of repulsion developed between sodium and potassium ions. The opening of potassium channels re-polarizes the membrane. This potential that re-polarizes the membrane is V_{adap} and is expressed as:

$$V'_{adap} = k_1(\upsilon - V_{dep}) - k_2 V_{adap} \tag{3.8}$$

Where k_1 and k_2 described in Equation 3.8 are depolarization and adaptation constants respectively, to be determined by the time constant of sodium and potassium channels.

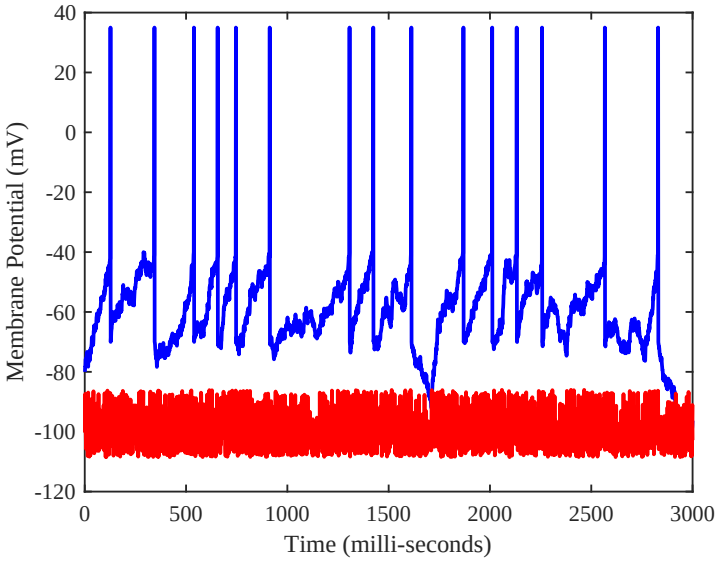


Figure 3.19 Generalized Leaky Integrate and Fire Model

The spike generation of GLIF model is illustrated in Figure 3.19 where input current is delineated by red and corresponding neural response is plotted in blue. From Figure 3.19, it is clear that threshold of neuron is constant. This property of GLIF model makes it static in terms of threshold variability.

3.4.2 Multi-scale Adaptive Threshold (MAT) Model

The key feature of MAT model is adaptive threshold function which makes the model more accurate than GLIF model in terms of spike time predictions. MAT model assumes three types of ions at resting state.

i. Sodium ions located outside the cell membrane

ii. Potassium ions reside inside the cell membrane

iii. Leakage ions that can propagate through cell membrane without any barrier all the time

The potential due to leakage ions is denoted by E_L. In MAT model, leakage ions are responsible for building the potential barrier that can perform transportation across the neural membrane. When positive stimulation current approaches the neural membrane, transportation of leakage ions across membrane is disturbed. This causes the sodium ions to be more sensitive to input current. The repulsive force between input current and sodium ions tends to open the sodium channels by providing enough room to rush inside the cell. The membrane potential v generated by MAT model can be expressed as:

$$v^{'} = \frac{1}{\tau_m}(v - E_L) + \frac{1}{C_m}I \tag{3.9}$$

The description of parameters in Equation 3.9 is, as follows:

C_m = Membrane capacitance

τ_m = Membrane time constant

$\tau_m = RC_m$

R = Membrane resistance

I = Stimulation current that can cause membrane depolarization

The opening and closing of sodium channels is nonlinear in nature. Therefore, the free path available for sodium ions to cross the sodium channels is not constant. As a result, potential

barrier undergoes variations in potential. This causes a variable potential barrier for the next spike. The variable potential barrier is referred as adaptive threshold expressed in Equation 3.10 as:

$$V_{th} = \sum_{k} H(t - t_k) + \beta \int_{-\infty}^{t} K(s)v'(t - s)ds + w \tag{3.10}$$

$H(t - t_k)$ = Exponential function of adaptive threshold shifted at t_k

$$H(t) = (\alpha_1 e^{-t/\tau_1} + \alpha_2 e^{-t/\tau_2})h(t) \tag{3.11}$$

Where parameters in Equation 3.11 can be depicted as:
α_1 = Amplitude of potential generated by sodium ions
α_2 = Amplitude of potential generated by potassium ions
τ_1 = Time constant of sodium channels
τ_2 = Time constant of potassium channels
$h(t)$ = Unit step function
e = Base of natural logarithm
β = Maximum amplitude of potential barrier
s = Time index of most recent spike fired
$K(s)$ = Function describing the ion channel dynamics

$$K(s) = se^{-s/\tau_v}h(s) \tag{3.12}$$

w = Weight vector describing the strength of input current as manipulated in Equation 3.12.

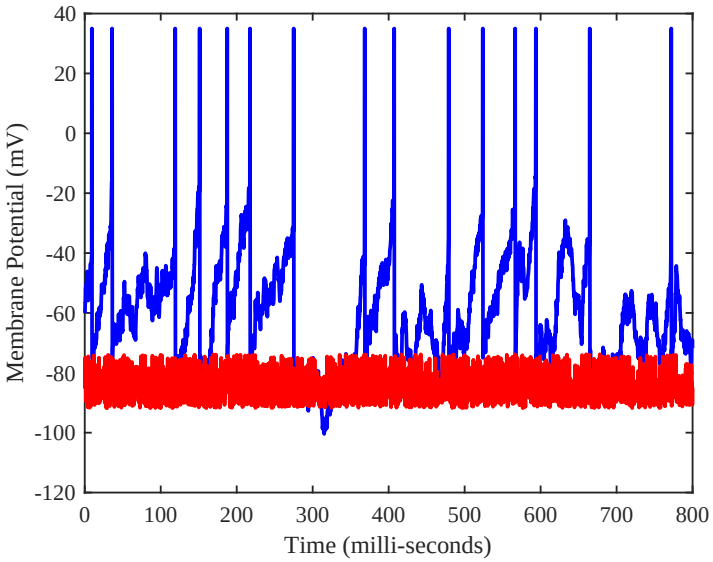


Figure 3.20 Multi-scale Adaptive Threshold Model

The action potential generated by MAT model is depicted in Figure 3.20, where red traces represent input current and blue elucidates corresponding response. Unlike GLIF model, hyperpolarization phase of MAT model is more significant due to adaptive threshold function. Each time spike is generated by MAT model, threshold potential is changed for next spike due to exponential nature of threshold.

3.4.3 Quadratic Integrate and Fire (QIF) Model

This model contains set of nonlinear differential equations with constant threshold function. The key feature of the model is the membrane recovery parameter u that controls the membrane potential after each spike is fired. QIF model assumes two types of ion channels:
i. Intracellular ion channels that allow the inward movement of sodium ions
ii. Extracellular ion channels that allow outward movement of potassium ions
Besides intracellular and extracellular ion channels, QIF assumes a membrane recovery parameter that acts after each spike is fired. Under resting state, QIF neuron remain quiescent. When a brief but strong synaptic input current approaches dendrites of QIF neuron, a composite stimulation current is generated. This causes the membrane to depolarize, and sodium channels are opened. As a result, sodium ions move into the cell causing an increase in membrane potential. The increase in membrane potential is controlled by membrane recovery parameter denoted by u. Therefore, membrane potential v generated by QIF model by synaptic current I and recovery parameter u, can be expressed in Equation 3.13 as:

$$v' = 0.04v^2 + 5v + 140 - u + I \tag{3.13}$$

It should be noted that QIF model is inspired by curve fitting technique. Therefore, by defining parameters we end up with constants coefficients of v^2 and v. The membrane recovery parameter is negative feedback in nature due to the fact that it controls the growth of increasing membrane potential. When neuron fires a spike of action potential, recovery parameter generates similar scaled spike and subtracted from membrane potential. This causes the membrane potential to reach the hyperpolarization phase. The recovery parameter can be depicted by Equation 3.14 in terms of membrane potential as:

$$u' = a(bv - u) \tag{3.14}$$

u = membrane recovery parameter after spike is initiated
a = time constant of membrane recovery parameter for intracellular interactions with ion channels
b = time constant of membrane recovery parameter for extracellular interactions with ion channels
Due to intracellular and extracellular interactions of ion channels, membrane potential abruptly fluctuates between positive and negative values. Therefore, after spike reset potential is defined as:

$$\text{If } v \geq V_{th}\ ; \ \text{ then } v = \begin{cases} V_p & \forall\ t \\ V_r & \forall\ (t+1) \end{cases}$$

The action potential generated by QIF model is depicted in Figure 3.21. The constant threshold of model can be observed by spike generation mechanism.

3.5 Performance Evaluation Measures

3.5.1 Coincidence Factor

Coincidence factor measures the performance of two sequences (experimental and predicted) of data. If the outcomes of both sequences are coincident, performance is maximum and vice versa. The coincidence factor Γ can be, defined as:

$$\Gamma = \frac{2(N_m - \langle N_p \rangle)}{\rho(N_m + N_d)} \tag{3.15}$$

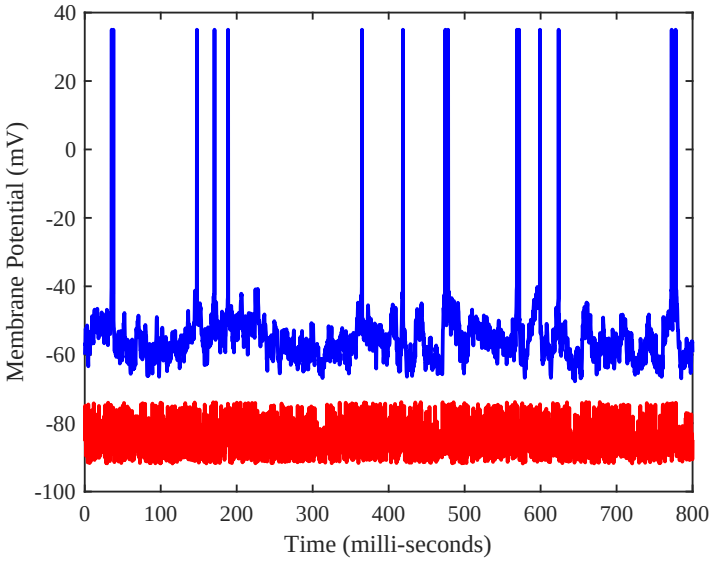


Figure 3.21 Quadratic Integrate and Fire Model

The parameters in Equation 3.15 are described as:
N_m = Total neural firings of model data
$\langle N_p \rangle$ = Mean value of neural firings estimated by Poisson spikes with frequency identical to model frequency
$\langle N_p \rangle = 2\omega\Delta N_d$
N_d = Total neural firings of dataset
ρ = Normalization factor
$\rho = 1 - 2\omega\Delta$
ω = Frequency of mean firings of dataset
$\omega = N_d/T$
T = Time period of observation
Δ = Time interval that determines the coincidence of two spikes
The value of the coincidence factor as unity ($\Gamma = 1$) manipulates the exact convergence of the model to experimental data [61].

3.5.2 Firing Rate Coefficient

Firing rate coefficient represents the neural firings in terms of correlation and variance of model data and dataset. For a large number of neural ensembles, evaluation of coincidence factor is cumbersome and may encounter inappropriate results due to bias sensitivity. In such cases, the normalized correlation coefficient for the firing rate of the network is a better choice for performance evaluation and can be defined as:

$$\eta = \frac{Cov(x, y)}{\sqrt{Var(x)Var(y)}} \tag{3.16}$$

Where x stands for experimental data, y elucidates predicted data. η is less sensitive to bias and only deals with neural variability because the mean is subtracted in the evaluation of covariance and variance. The value of η approaching 1 indicates the exact convergence of the model to experimental data while approaching 0, results in poor prediction [62].

3.6 Summary

The electrical response of neuron can be predicted by computational models. To perform large scale brain simulation in real time, computationally efficient and biologically comprehensive model is required. For this purpose, hybrid excitable cell model is proposed and different neurocomputational features are simulated. The hybrid excitable cell model is proposed by assuming exponentially decaying threshold function in accordance with the biological neuron holds. The membrane potential of neuron is evaluated by considering dynamics of ion channels in terms of potential rather molecular interactions. This assumption simplified the model equations by introducing the potential values to estimate membrane potential.

KEY TAKEAWAYS

- The **HEC model**: $\tau v' = k(v - V_r)f(v - V_{th}) - u + RI$, with recovery $\tau u' = a(bv - u)$ and an exponentially adaptive threshold $V_{th} = Ae^{(t_s - t)/\tau} - \theta$.
- Neurotransmitter and adrenergic effects enter as a gated synaptic current $I_x = \bar{g}_x(v - V_x)e^{(t_s - t)/\tau_x}$.
- Fourteen firing patterns, from regular spiking to spike latency, are reproduced by tuning only a, b, V_r and d.
- The model is validated on a $2191 \times 14 \times 217$ mouse dataset against the **GLIF, MAT and QIF** models, using the coincidence factor Γ and the firing-rate coefficient η.

CHAPTER 04

Results and Discussions: Neuron

> *What I cannot create, I do not understand.*
>
> — Richard P. Feynman

QUESTIONS TO EXPLORE

1. How closely does the HEC model reproduce real spikes recorded from 2191 mouse visual-cortex neurons?
2. How does it compare with the GLIF, MAT and QIF models under identical input?
3. Does that accuracy hold up when we move from single cells to the whole network?
4. How can one hundred billion neurons be simulated on a desktop computer?

IN THIS CHAPTER

4.1 Cell Level Performance 39
4.2 Network Level Performance 45
4.3 Building Large Scale Model of Human Brain 47
4.4 Limitations 49
4.5 Homogeneous and Heterogeneous Spatial Firing Distribution 51
4.6 Summary 52

This chapter is dedicated to the implementation of proposed model and validation against the experimental dataset. The proposed model is stimulated by time varying current and corresponding response is recorded. State of the art models including Generalized Leaky Integrate and Fire (GLIF) model, Multi-scale Adaptive Threshold (MAT) model and Quadratic Integrate and Fire (QIF) model are also stimulated by identical time varying current. The results of models are compared with dataset and proposed model is observed to be more efficient in terms of accuracy at cell level and computing simplicity at network level.

4.1 Cell Level Performance

Neurons are excitable cells that can propagate electrical response through axon. The electrical activity of neuron in the brain can be recorded by applying brief time varying current. For this purpose, experimental framework is designed where neurons are stimulated by identical current and corresponding response is recorded. The experimental recordings of neural activity contain 2191 neurons of mouse brain. The neurons are activated by photo current and corresponding response along with strength of photo current is recorded. The values of neural response is recorded at constant rate of one recording after each 0.275 seconds [63]. The process of recording neural activity continues 217 times. The photo current exposure to all neurons is identical due to constant intensity of light source. The intensity of photo source is converted into electrical signal by photo sensors to record the activation current. This process of neural recording is repeated 14 times. Therefore, we obtained a dataset comprises of neural activity of 2191 neurons, for 217-time bins repeated for 14 trials. The dataset recorded in this way comprises of a three-dimensional matrix with dimensions $2191 \times 14 \times 217$.

For fair comparison, we stimulated state-of-the-art models with identical current as recorded by photo sensors. The stimulated models include generalized leaky integrate and fire model, multi-scale adaptive threshold model, quadratic integrate and fire model and hybrid excitable cell model. Each model is stimulated by identical current and corresponding firing patterns are stored in computer memory. The model data recorded by each model comprises of a three-dimensional matrix of size $2191 \times 14 \times 217$. To find the performance of each model with respect to dataset, we need to find coincidence factor at single cell level. The neural ensembles of each neuron are compared with dataset in terms of spike firing occurrence. By implementing Equation 3.15, depicted in Algorithm 2, coincidence factor is evaluated as follows:

- A mask vector with dimensions five is initialized to zero for precision of ±2 elements on each side of central element of mask vector.
- The mask vector is loaded with five elements of model data for comparing the spikes with dataset.
- Select the first element of dataset and compare with spike train of mask vector.
- In case if dataset selected represents spike, and any of five elements of mask also hold a spike, the matching of spike is confirmed.
- By detecting the coincidence of spikes by analyzing the firing patterns of each neuron over 217 time bins, coincidence counter is increased by 1 each time.
- Repeat the iterations until dataset is completely compared with model data.

Table 4.1 Comparison between hybrid excitable cell model, quadratic integrate and fire model, multi-scale adaptive threshold model and generalized leaky integrate and fire model.

	Coincidence Factor Γ			Firing Rate Coefficient η		
Model	Dataset	Prediction	Γ	Dataset	Prediction	η
GLIF	84	48	0.692066	787	488	0.554943
MAT	84	53	0.733302	787	492	0.612716
QIF	84	58	0.774240	787	539	0.674387
HEC	**84**	**70**	**0.862579**	**787**	**655**	**0.826825**

The performance of models in terms of coincidence factor can be expressed as:
Hybrid Excitable Cell (HEC) Model = 86%
Quadratic Integrate and Fire (QIF) Model = 77%
Multi-scale Adaptive Threshold (MAT) Model = 73%
Generalized Leaky Integrate and Fire (GLIF) Model = 69%
Readers interested to find the details of implementation of Equation 3.15 and corresponding computations of each trial, are encouraged to consult [64].

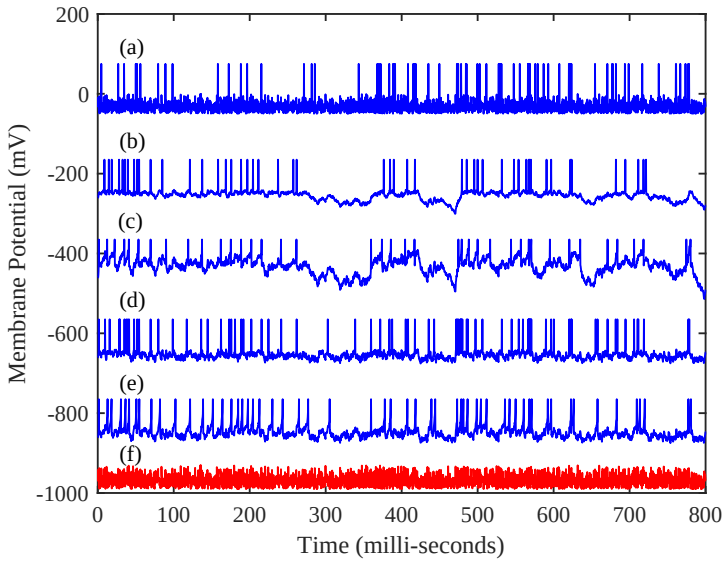


Figure 4.1 (a) Dataset (b) GLIF (c) MAT (d) QIF (e) HEC Model (f) Input current.

Baseline models including Generalized Leaky Integrate and fire (GLIF) model, Multi-scale Adaptive Threshold (MAT) model, and Quadratic Integrate and Fire (QIF) model, are stimulated by identical input current as depicted in Figure 4.1. Figure 4.1a represents the spike train of dataset recorded for mouse brain neurons, activated by optically generated synaptic current. The dataset comprises of electrophysiological recordings of 2191 neurons, for the period of 800 milli-seconds. The response of single neuron of dataset is plotted in Figure 4.1a.

Figure 4.1b illustrates the response of Generalized Leaky Integrate and Fire (GLIF) model for identical input synaptic current as provided for recording the dataset. GLIF model assumes the set of ionic currents responsible for depolarization of membrane potential. Therefore, the effect of hyperpolarization currents is not depicted by GLIF model. As a result, the spike prediction of GLIF model is poor when compared with dataset.

Algorithm 2: Coincidence Factor

Input: mouse data, Δ, T, t
Output: Γ

Initialize parameters
for $m \leq trials$ **do**
  for $k \leq neurons$ **do**
    Initialize neural parameters
    Find indices of spikes from the dataset (N_d)
    $data(k) = find(V_{data} \geq 30)$;
    Find indices of spikes from models (N_m)
    $model(k) = find(V_{model} \geq 30)$;
    Find the coincidence of spikes as:
    for $i \leq N_m$ **do**
      for $j \leq N_d$ **do**
        $Q = model(i)/data(j)$
        if $Q == 1$ **then**
          $N_C = N_C + 1$
    $n_{model}(k) = N_C$;
    $\omega(k) = (T \times t)/n_{model}(k)$;
    $N = 2\omega(k)\Delta N_d$;
    $N_{model}(k) = 1 - 2\omega(k)\Delta$;
    $\Gamma(k) = 2 \times (n_{model}(k) - N)/(N_{model}(k) \times (data(k) + n_{model}(k)))$;
  $\Gamma(m) = mean(\Gamma(k))$;
Save results in output file

Multi-scale Adaptive Threshold (MAT) model assumes the leakage ions in prediction of membrane potential. The effect of hyperpolarization potential is integrated in adaptive threshold function that can update after each spike is fired. The neural response of MAT model is depicted in Figure 4.1c. Due to variable time constants associated with ion channels, membrane potential moves more towards hyperpolarization phase. As a result, membrane recovery of neuron takes longer time to fire the next spike for same input synaptic current as delineated in Figure 4.1c.

Quadratic Integrate and Fire (QIF) model assumes intracellular and extracellular interactions of ion channels. The composite effect of ionic currents is provided to model for activation of neuron. The membrane recovery is integrated by the model parameter u, instead of threshold. In the QIF model, hyperpolarization phase of action potential is modeled by membrane recovery parameter. The response of QIF model by application of identical input synaptic current is illustrated in Figure 4.1d.

Hybrid Excitable Cell (HEC) model combines the features of GLIF, MAT, and QIF models to predict the neural response [65]. In HEC model, the effect of positive and negative ions on membrane potential is manipulated by adaptive exponential threshold function. Moreover, the membrane potential recovery parameter is assumed from the QIF model. As a result, spike prediction of HEC model is better than GLIF, MAT and QIF models when compared with dataset, as illustrated in Figure 4.1e. The input synaptic current to stimulate the models is

depicted in Figure 4.1f.

Table 4.2 Numerical values of coincidence factor for 10 neurons out of 2191 neurons of first trial of dataset out of 14 trials.

Neurons	N_{data}	N_{qif}	Γ_{qif}	N_{mat}	Γ_{mat}	N_{glif}	Γ_{glif}	N_{hec}	Γ_{hec}
1	74	49	0.76	45	0.72	40	0.67	61	0.86
2	88	49	0.68	45	0.64	41	0.60	69	0.83
3	60	35	0.71	32	0.66	30	0.63	48	0.85
4	96	76	0.83	73	0.81	61	0.73	89	0.91
5	90	61	0.76	56	0.73	47	0.65	72	0.84
6	98	50	0.64	46	0.61	39	0.54	71	0.79
7	66	49	0.81	44	0.76	38	0.69	59	0.89
8	86	53	0.72	46	0.66	45	0.65	72	0.86
9	83	68	0.85	61	0.80	52	0.73	75	0.89
10	76	55	0.79	52	0.77	45	0.71	65	0.87

The numerical values of coincidence factor of 10 neurons out of 2191 neurons of dataset is listed in Table 4.2. The values listed in Table 4.2 is from first trial of dataset out of 14 trials. In Table 4.2, first neuron of dataset fired 74 spikes on 217-time bins, where each time bin is of 0.275 seconds. Therefore, the first neuron of dataset is observed for 217×0.275=59.7 seconds. During this time, first neuron of dataset fired 74 spikes. Only 49 spikes of Izhikevich neuron model coincided with dataset, with coincidence factor of 0.76. Similarly, spike coincidence of MAT and GLIF models are 45 and 40 spikes respectively. The coincidence factor for MAT model is 0.72 and for GLIF model 0.67. The spikes coinciding with experimental data by HEC model contains 61 spikes with highest coincidence factor of 0.86 as depicted by row 1 of Table 4.2.

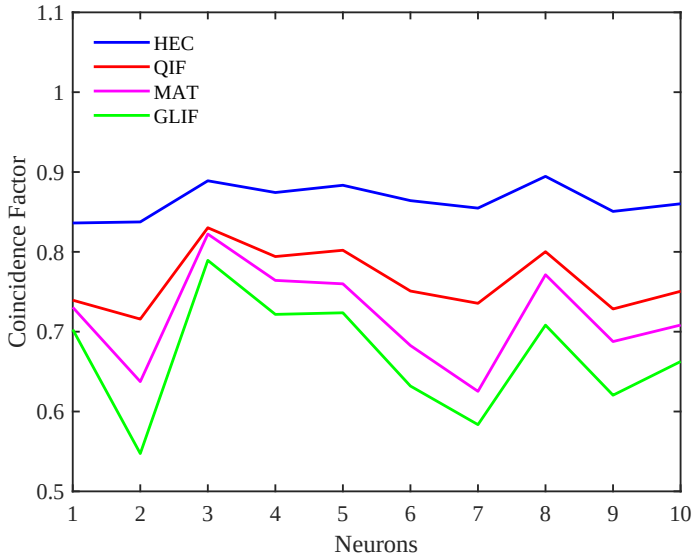


Figure 4.2 Graphical representation of coincidence factor of 10 neurons out of 2191 neurons from first trial of dataset out of 14 trials.

Figure 4.2 illustrates the graphical representation of coincidence factor of first 10 neurons of dataset. The dataset contains 2191 neurons, with neural recordings conducted over 217-time

bins. Therefore, a single trial of neural responses is represented by the matrix with dimensions 2191×217. The graphical representation of neural responses of 2191 neurons over 217-time bins produces a complicated plot. For simplicity, we plotted the response of first 10 neurons for better illustration. In Figure 4.2, coincidence factor of neural responses changes over time rapidly. The fluctuations in neural response are due to correlated noise that arises from dendritic neural structure which captures the signal from other neurons.

Table 4.3 Average numerical values of coincidence factor of 14 trials with each trial containing 2191 neurons.

Trials	N_{data}	N_{qif}	Γ_{qif}	N_{mat}	Γ_{mat}	N_{glif}	Γ_{glif}	N_{hec}	Γ_{hec}
1	84	59	0.78	54	0.74	50	0.70	71	0.86
2	87	61	0.78	56	0.74	52	0.70	74	0.86
3	86	60	0.78	55	0.74	50	0.69	73	0.86
4	82	57	0.77	52	0.73	48	0.69	69	0.86
5	79	54	0.77	50	0.73	46	0.68	66	0.86
6	77	53	0.76	48	0.72	44	0.68	64	0.86
7	76	51	0.76	47	0.72	43	0.67	63	0.85
8	75	51	0.76	47	0.72	42	0.68	62	0.86
9	74	50	0.76	46	0.72	42	0.67	62	0.85
10	74	50	0.76	45	0.71	41	0.67	61	0.85
11	74	50	0.76	45	0.71	41	0.67	61	0.85
12	74	50	0.76	45	0.71	41	0.67	61	0.85
13	74	50	0.76	45	0.71	41	0.67	61	0.85
14	74	50	0.76	45	0.71	41	0.67	61	0.85
Mean	78	53	0.77	49	0.73	44	0.68	65	0.86

Table 4.3 manipulates the numerical values of coincidence factor for 14 trials of dataset. The dataset contains 2191 neurons, with neural responses taken over 217-time bins. The time span of each time bin is 0.275 seconds. The neural responses of 2191 neurons over 217-time bins constitute a single trial. The mean values of coincidence factor for 14 trials of dataset are listed in Table 4.3. First row of Table 4.3 represents that, on average 84 spikes per neuron observed, for which 59 spikes of Izhikevich model, 54 spikes of MAT model, 50 spikes of GLIF model and 71 spikes of HEC model coincided. Therefore, HEC model performance is better than Izhikevich, MAT and GLIF models.

Figure 4.3 illustrates the graphical representation of coincidence factor of 14 trials. The matrix representing 14 trials of dataset can be expressed as 2191×14×217. The analysis of such large value dataset is complicated in three-dimensional space. Therefore, we implemented the mean values of each trial for simplicity and better illustration of dataset. From Figure 4.3, it is clear that average value of coincidence factor is approximately constant. Therefore, the mean value of coincidence factor effectively elucidates the trend of neural firing of model data in comparison of dataset.

The spike generation mechanism of neuron involves abrupt changes in membrane potential. To compensate for the changes in membrane potential after spike is fired, membrane potential recovery parameter is introduced. This parameter behaves like an exponentially decaying function of membrane potential from peak value. Whenever, action potential spike is generated, membrane potential recovery parameter is negatively feedback to membrane potential. As a

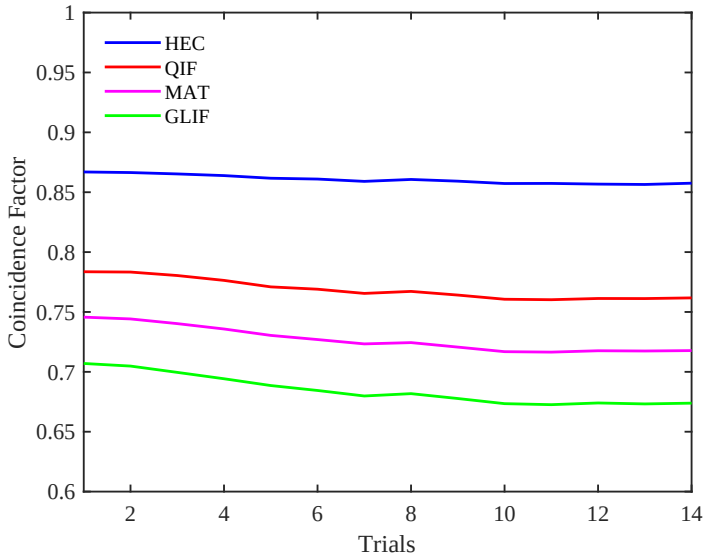


Figure 4.3 Graphical representation of average value coincidence factor of 14 trials with each trial containing 2191 neurons.

result, membrane potential tends to decay towards resting conditions. The effect of leakage ions is encountered in model as static threshold and hyperpolarization potential values. The effects of hormonal and adrenergic receptors also included in model in terms of excitation current.

Models	Biological Details	Regular spiking	Fast Spiking	Class-I	Class-II	Intrinsic Induced Bursting	Intrinsic induced spiking	Mixed mode	Phasic spiking	Phasic bursting	Resonator	Tonic Bursting	Tonic spiking	Spike Frequency Adaptation	Spike Latency	Cardiac Myocyte	Ventricular Fiber	Purkinje Fiber	Number of FLOPS
Generalized Leaky Integrate and Fire (GLIF) Model	-	+	+	+	+	+	+	+	+	+	-	+	+	-	-	-	-	-	14
Multi-Scale Adaptive Threshold (MAT) Model	-	+	+	+	+	+	+	+	+	+	+	+	+	-	-	-	-	-	26
Quadratic Integrate and Fire (QIF) Model	-	+	+	+	+	+	+	+	+	+	+	+	+	+	+	-	-	-	13
Hybrid Excitable Cell (HEC) Model	+	+	+	+	+	+	+	+	+	+	+	+	+	+	+	+	+	+	21
Hodgkin-Huxley Model	+	+	+	+	+	+	+	+	+	+	+	+	+	+	+	-	-	-	1200

Figure 4.4 Comparison of baseline models with proposed model in terms of computational complexity.

The proposed model is extended to simulate the different neurocomputational features. The neurocomputational features are the different firing patterns of neurons. These firing patterns are determined by the release of different types of neurotransmitters and adrenergic receptors. The complexity of each baseline model along with neurocomputational features is listed in Figure 4.4. To validate the proposed model against experimental dataset, we need to consider the identical conditions. For this purpose, electrophysiological recordings of mouse brain are assumed as dataset. The dataset comprises of electrophysiological recordings of 2191 neurons, over 217 time-bins for 14 trials. This forms the matrix with dimensions $2191 \times 14 \times 217$. The baseline models to compare the accuracy of proposed model include generalized leaky integrate and fire model, multi-scale adaptive threshold model and quadratic integrate and fire model with identical dimensions as dataset. The performance evaluation of proposed model

with baseline approaches is carried out in terms of coincidence factor at single cell level and normalized correlation coefficient at network level.

The comparison of neural responses at cell level for small population of neurons in terms of coincidence factor is effective metric. However, for large scale neural ensembles, such comparison is not possible. Moreover, coincidence factor strongly depends upon step size within which neurons fired are considered as coincident. In short, at large scale network level, calculation of coincidence factor is computationally prohibitive, therefore, normalized correlation coefficient is better choice at large population of neurons.

4.2 Network Level Performance

Large-scale simulation of brain neural network involves the firing of individual neuron as well as communication between other neurons. The behavior of neurons in terms of neurocomputational features may vary within intra-regional and inter-regional communication. Under such circumstances, coincidence factor is difficult to manipulate the information flow between neurons. Therefore, normalized correlation coefficient is good choice for performance evaluation of model data against dataset. The normalized correlation coefficient assumes two vectors of same dimensions. The correlation between both vectors can be calculated by evaluating covariance of both vectors normalized by variance of each vector. This normalization restricts the value of correlation coefficient within the range of +1 to -1. In current study, negative correlation between neural firings do not exist, therefore, correlation coefficient lies between 0 to 1 [66].

To find the correlation coefficient, we assume dataset in the form of single trial. The dataset is composed of a three-dimensional matrix of type $2191 \times 14 \times 217$. We decomposed dataset into individual trial of dimensions 2191×217. A vector of dimensions 217 is defined and each entry of vector contains firings of 2191 neurons. Similarly, a vector of dimensions 217 is defined for each model data and firings of 2191 neurons of each model is added and resultant firings are stored in corresponding element of vector. Readers interested to find the details of implementation of Equation 3.16 and related computations are encouraged to consult [67].

The firings of 2191 neurons of dataset calculated over 217 time bins are plotted in Figure 4.5 by black solid line. The fluctuations in neural firings indicate that for each time bin different number of neurons fired exhibiting the transfer of information between neurons. Similarly, firings of hybrid excitable cell model is plotted by blue, quadratic integrate and fire by red, multi-scale adaptive threshold by magenta and generalized leaky integrate and fire by green solid line as depicted in Figure 4.5.

Table 4.4, row 1 manipulates the computation of first trial of dataset in terms of mean firings of 2191 neurons averaged over 217-time bins. For trial 1, dataset fired 846 spikes averaged over 217-time bins. The average spikes fired by QIF, HEC, MAT and GLIF models are 596, 714, 549 and 504 respectively. The firing rate coefficient for QIF, HEC, MAT and GLIF models by implementing Equation 3.16 is 0.69, 0.83, 0.63 and 0.58 respectively. The mean values of 14 trials are depicted in last row of Table 4.4. It should be noted that the performance of the HEC model is better than QIF, MAT and GLIF models due to biological details of parameters implemented for HEC model.

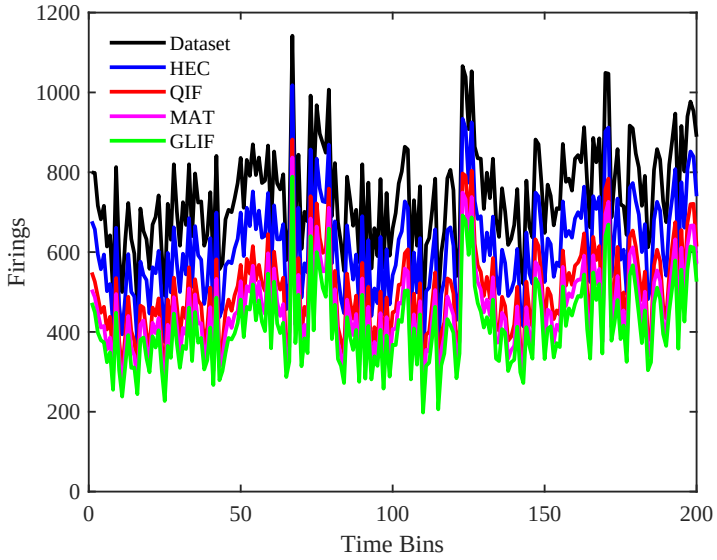


Figure 4.5 Graphical representation of firings of 2191 neurons per time bin over 217 time bins for first trial of dataset.

Table 4.4 Mean firings of 2191 neurons averaged over 217 time bins for each trial of dataset.

Trials	Dataset	QIF	HEC	MAT	GLIF	η_{qif}	η_{hec}	η_{mat}	η_{glif}
1	846	596	714	549	504	0.69	0.83	0.63	0.58
2	882	620	745	569	521	0.68	0.83	0.62	0.57
3	868	609	733	557	509	0.68	0.83	0.62	0.56
4	831	577	698	528	482	0.68	0.83	0.61	0.56
5	800	550	668	504	460	0.67	0.82	0.61	0.55
6	780	534	650	488	444	0.67	0.82	0.61	0.55
7	763	518	632	472	429	0.66	0.82	0.60	0.54
8	759	516	631	470	428	0.67	0.82	0.60	0.55
9	752	508	623	463	421	0.66	0.82	0.60	0.54
10	747	502	616	456	414	0.66	0.81	0.59	0.54
11	748	502	617	456	414	0.66	0.82	0.59	0.54
12	746	501	615	456	415	0.66	0.81	0.60	0.54
13	748	503	616	458	415	0.66	0.81	0.60	0.54
14	746	503	617	457	415	0.66	0.82	0.60	0.54
Mean	787	539	655	492	448	0.67	0.82	0.61	0.55

The firings of 2191 neurons per time bin are depicted in Figure 4.5. The firing rate coefficient for each trial is calculated by evaluating the correlation between entries of model data with respect to dataset. The average value of firing rate coefficient η for each model is listed in Table 4.4. The graphical representation of mean firing rate coefficient for each trial is illustrated in Figure 4.6. It should be noted that mean firing rate coefficient for all trials is approximately constant. This shows that the neural responses entirely depend upon the stimulus regardless the correlated noise encountered by the neurons [68].

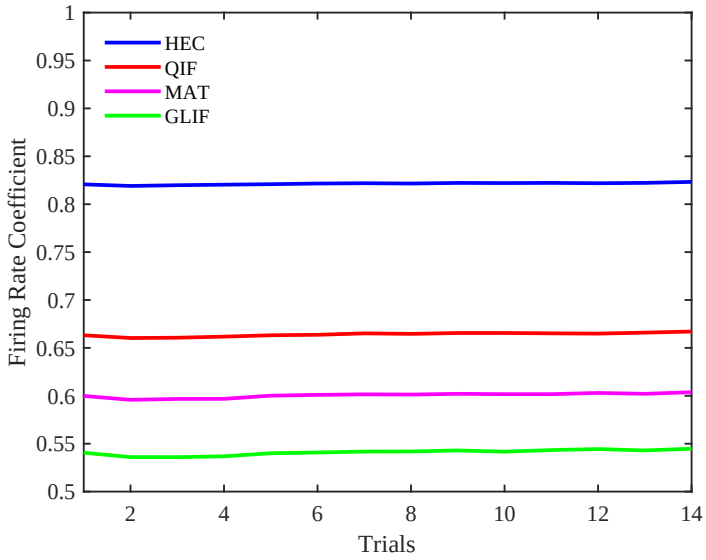


Figure 4.6 Graphical representation of firing rate correlation coefficient of 2191 neurons averaged over 217 time bins for 14 trials.

4.3 Building Large Scale Model of Human Brain

The human brain contains about 100 billion neurons with more than 1000 trillion synaptic connections. Each neuron is linked with other neurons by 1000 to 10,000 synaptic connections. Building the neural network of such an extraordinary organ is quite a challenging task. The first barrier is memory required to build the computational basis of model. Conventional methods of brain simulation require super computing resources with petaflops of computing capacity and terabytes of storage capacity. The second barrier in human brain simulation is development of connections between neurons to build the largest neural network of brain. Even modern supercomputers are not able to hold the computing facility to simulate the human brain in real time by conventional methods of brain simulation [69].

To build the large scale model of human brain, we assume the binary behavior of individual neuron. A neuron in the brain can hold only two states, either fired or not fired. If a neuron is fired, it corresponds to binary state 1 and if neuron is not fired, it corresponds to binary state 0. Therefore, if we assume a variable to locate the memory location for membrane potential, it will consume 64-bits per memory location depending upon the architecture. Thus, a single bit will represent the neuron, and variable will represent a cluster of neurons with 64 neurons per cluster. If we define a variable in MATLAB with dimensions 1000×1000 containing 64-bits per entry, we end up with 64 million bits, representing 64 million neurons. Figure 4.7(a) represents 1000×1000 matrix containing decimal entries defined in MATLAB. By definition, each decimal number in MATLAB is represented by equivalent 64 bits binary number. Therefore, 1000×1000 matrix is in fact a three dimensional matrix in binary format 1000×1000×64 as depicted in Figure 4.7(b). The bit stream of decimal number into equivalent binary number with 64 bits is elucidated in Figure 4.7(c). Details of computation are depicted in Algorithm 3 for illustration.

To simulate 100 billion neurons, we assumed four spiking features of neurons, regular spiking, fast spiking, tonic spiking and phasic spiking. We initialized 1000×1000 matrix to zero and

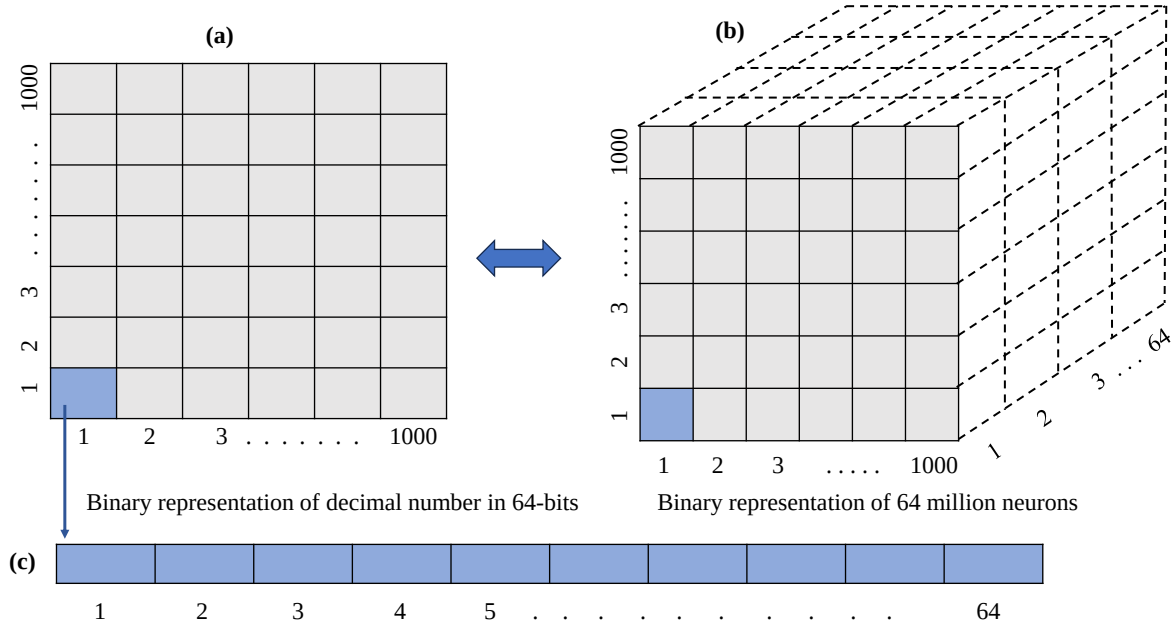


Figure 4.7 Binary representation of 1000×1000 matrix to manipulate 64 million neurons. (a) 1000×1000 matrix (b) Splitting of 1000×1000 matrix with each decimal number into 64 bits binary number. (c) 64 bit binary representation of decimal number.

decomposed each number to a bit stream of 64. Synaptic current from 1000 neurons is superposed and a composite value of current I is generated. This current I is passed through the model equations to evaluate membrane potential v. The value of membrane potential is compared with threshold potential V_{th}. If membrane potential exceeds threshold potential, corresponding bit is set to 1. The simulation procedure is summarized in Algorithm 3 for illustration.

Simulation of 1000×1000 matrix yields 64 million bits, equivalent to 64 million neurons. This procedure is repeated in a loop for 16 times to end up one billion bits (1000×1000×64×16) per spiking feature. In our case, we assumed four features, therefore, total 4 billion bits or neurons are simulated in this way. To achieve the 100 billion neurons, we need to execute the procedure in another loop of 25 repetitions. Hence, we end up with 100 billion neurons with 100 trillion synaptic connections to simulate on desktop processor. The simulation results takes about 1 hour, 23 minutes and 42 seconds on Intel(R) Core(TM) i5-2410M CPU with 2.30 GHz containing 4GB RAM. The parameters of simulation are summarized below:
Features = 4
Grid size = 1000×1000
Bits per entry = 64
Trials = 16
Rank = 25
Total Bits = $4 \times 1000 \times 1000 \times 64 \times 16 \times 25 = 1.024 \times 10^{11}$ bits
Total Firings = 102019
Total Time = 1.395 hours = 1 hour, 23 minutes, 42 seconds
System Specifications = Intel(R) Core(TM) i5-2410M CPU 2.30 GHz 4GB RAM

Algorithm 3: Evaluation of binary matrix for 64 million neurons

```
Input: N, Data matrix D(1000,1000)
Output: Firings
Initialize parameters
for i ≤ N do
    for j ≤ N do
        Initialize 64 bit vector B(1,64)
        for k ≤ 64 do
            Calculate v
            if v ≥ V_th then
                B(k) = 1
                Firings = Firings + 1
                D(i, j) = D(i, j) + 2^(k−1)
Plot and save results in the output file
```

Simulation results are plotted in Figure 4.8 after each firing is initiated. The parameters of four classes (Blue: regular spiking, Red: fast spiking, Magenta: tonic spiking, Black: phasic spiking) of spiking neurons were initiated and corresponding values are stored in bit stream vector B defined in Algorithm 3. For each firing of neuron, we plotted a dot with specific color code corresponding to the firing feature at location defined by index value (i, j, k).

The largest neural network simulated so far, reported about 1 billion neurons (1% of brain), on Japanese flagship K-computer (K is derived from Japanese word *Kei* stands for quadrillion 10^{16}) by tile partitioning method [70]. This neural network is the most detailed network of cortical neurons simulated over 82,944 computational nodes with realistic anatomical and physiological parameters. The large-scale simulation of brain depends upon the computational model implemented, details of biological features and computing resources available. The detailed neural models that can capture the dynamics of neurons down to ion channels, are computationally expensive. Hence, we need to optimize the trade-off between biological features and computing resources. In our case, computing resources are limited, therefore, we implemented the simplest neural architecture. For simplicity, we assumed bit stream of data rather tile partitioning, which reduced the memory allocation and corresponding weight storage. Moreover, representation of neural responses in bits reduced the complicated computations related to the data structures implemented for brain simulation.

4.4 Limitations

Due to limited computational resources available, biological details of neurons related to morphological and electrophysiological features are not included in simulation. For simplicity, these details are generated by random numbers within the actual biological range of parameters. The limitations of large-scale simulation of the human brain reported in this study, are listed below:

- This work is intended to claim the simulation of largest spiking neural network of human brain on desktop. Therefore, approximations are necessary in this regard to meet the

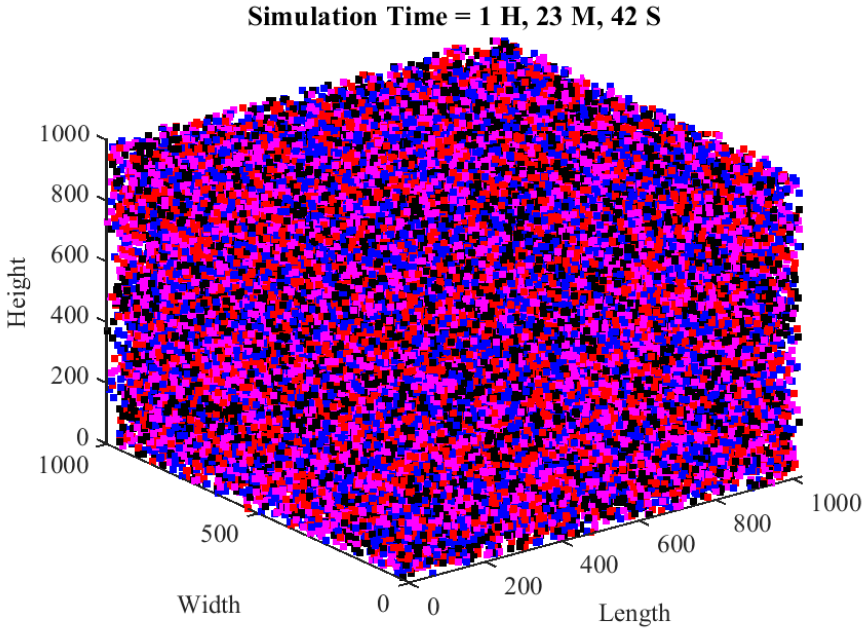


Figure 4.8 Simulation results of 100 billion neurons with 100 trillion sparsely coupled synaptic connections.

capacity of limited resources available. The standard benchmarks such as the Allen Brain Observatory spiking data or BrainScaleS data are of prime importance while dealing with detailed compartmental models with morphological features.

- The simulation of human brain is performed by assuming point neuron with no dendritic connections to communicate with other neurons. After each iteration, values of model parameters are initialized to efficiently utilize the limited memory available for computation.
- The synaptic connections developed in simulation are sparsely coupled, without any resemblance with biological neurons. Therefore, the effect of neural signal propagation in the form of neural network cannot be identified in current scenario.
- Detail of membrane potential variations are not included in simulation of large-scale brain simulation. Therefore, we cannot extract the electrophysiological details from simulation.
- The values of synaptic currents and membrane potential are processed in digital format for simplicity. Therefore, temporal features of neural activity in terms of neurocomputational features are lost.
- Mathematical models to extract the higher-level features such as gamma oscillations or traveling waves can enhance the computational complexity of model. Moreover, we need to integrate electrophysiological features and spatial distribution of neurons into entirely different frameworks such as spike raster models to detect neural oscillations. This study is limited to point neuron modeling only; therefore, spike raster treatment is not generated here.

4.5 Homogeneous and Heterogeneous Spatial Firing Distribution

In this section expected neural distribution of one million cells is presented with sparsely coupled neuron as the exact connections of neurons are unknown. Large scale brain simulation can be identified by different visualisation techniques such as local field potentials (LFPs), electrocorticographic signals (ECoGs), voltage sensitive dye imaging (VSDI) signals, electroencephalography (EEG) and magnetoencephalography (MEG). Each technique contains different model mechanism at back end for specific patterns to be visualised. Hence, the model choice and limitations plays vital role in large scale brain simulation to extract the animal behaviour. In our case, point neuron model is adopted, thus we can expect only neural distribution in the form dots as depicted in Figure 4.9 by assuming five neurocomputational features due to limited computational power available. A grid of one million neurons is initialized to resting membrane potential of -80mV, having one thousand synaptic connections per neuron, defined by Equation 4.1.

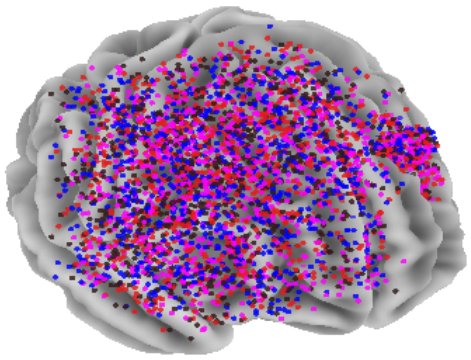


Figure 4.9 Neural activity across different brain regions in terms of neurocomputational features of brain with heterogeneous inter regional communication represented by different colours, previously reported for excitatory and inhibitory neurons [71].

$$I_{synaptic} = sum(0.2 * rand(1, 1000)) \tag{4.1}$$

The value 0.2 is derived from experimental data set with correlation noise coefficient centred at 0.2. Assumption behind considering 1000 synaptic connections comes from original Izhikevich model to make the comparison between identical trials. By applying finite difference method technique, value of membrane potential at each neuron is evaluated. The neurons having membrane potential greater or equal to 30mV are plotted by dot depending upon the index value (i, j, k). Figure 4.9 elucidates the homogeneous spatial distribution of five features of neurons by HEC model, with parameter values defined in [72, 73].

Same procedure can be applied for different brain regions to evaluate heterogeneous spatial neural distribution as depicted in Figure 4.9, mapped on brain surfaces. Due to limited computational resources available, we restricted our simulations to million scale only. However, modern supercomputers (Spinnaker [74] or Japanese Flagship K-computer [75]) can be able to define the neural network of the order of brain that can be viewed on brain surfaces. Each coordinate on brain surface describes the certain neuron number with simultaneous firings. Thus, the neurons fired instantaneously are depicted by dot on brain surface and assumed to

form network. Figure 4.9 illustrates the spatial distribution of neuron firings on brain surfaces in the form of oscillatory activity.

The oscillatory activity of neuron firings consists of multiple propagating waves with different excitation frequencies depending upon governing neurocomputational features. These waves spontaneously appear and disappear at various locations of brain surfaces due to sparsely coupled neural network (one thousand synaptic connections in this case) reported by [71]. Once the connections between neurons are developed with realistic model (unknown at this time), we can generate realistic propagating waves patterns. The simulated signals plotted on brain surfaces can be correlated with human subjects observed in vivo and in vitro under various constraints [76, 77].

4.6 Summary

In this chapter performance of hybrid excitable cell model is compared with state-of-the-art models at single cell level and at network level. At single cell level, performance of models is determined by coincidence factor. At network level, the performance of hybrid excitable cell model is determined by firing rate coefficient. Firing rate coefficient represents the normalized correlation coefficient evaluated by analyzing firings of model in comparison to dataset. Due to limited memory space and computation power available, we are not able to store the synaptic information for the next iteration. However, neural response can be stored in memory as bit stream because one hundred billion neurons in bit format can occupy 13 gigabytes of memory space.

KEY TAKEAWAYS

- **Cell level:** coincidence factor $\Gamma = 0.86$ for HEC, against 0.77 (QIF), 0.73 (MAT) and 0.69 (GLIF).
- **Network level:** firing-rate coefficient $\eta \approx 0.83$ for HEC, against 0.67 (QIF), 0.61 (MAT) and 0.55 (GLIF).
- Treating each neuron as one **bit** lets 1.024×10^{11} neurons be simulated in about 1 h 24 min on a Core i5 laptop with 4 GB of RAM; storing the whole brain needs about **13 GB**.
- The trade-off is that binary coding discards membrane-potential detail and temporal features.

CHAPTER 05

Results and Discussions: Cardiac Myocyte

> *The heart has its reasons which reason knows nothing of.*
>
> — Blaise Pascal

QUESTIONS TO EXPLORE

1. How must the HEC model change to capture the long plateau of a cardiac action potential?
2. Which ionic currents and calcium fluxes shape each phase of a heartbeat?
3. Why do cardiac action potentials differ between human, dog, cat, zebrafish, guinea pig, rabbit, mouse and rat?
4. How can a cardio-neural network of 1000 cells be used to predict heart rate variability?

IN THIS CHAPTER

5.1 Cardiac Myocytes 54
5.2 Cardiac Currents 57
5.3 Calcium Fluxes 68
5.4 Cardiac Action Potential of Different Species 72
5.5 Cardio-Neural Network 80
5.6 Pancreatic Cells 82
5.7 Summary 83

In this chapter we extended Hybrid Excitable Cell model to cardiac myocytes. Cardiac myocytes are excitable cells in the heart that can link electrical activity to mechanical function. The excitation and contraction in the heart is due to systolic and diastolic pressure generated due to blood flow. The electrical response of cardiac myocyte network predicts the excitation-contraction coupling and abnormalities related to the heart response. In this chapter, our focus is to model the electrophysiological activity of cardiac myocytes and extend the concept of single cell to the network level.

5.1 Cardiac Myocytes

Cardiac myocytes are excitable cell that produces action potential due to mechanical functioning of cardiac activity. The electrophysiological activity of cardiac myocytes is initiated by local pacemaker cells located in sin-atrial (SA) and atrioventricular (AV) node. Unlike neurons, cardiac myocytes hold a large amount of calcium ions reserved in sarcoplasmic reticulum. Whenever pace-making cells initiate an electrical activity, it propagates in the form of circular waves toward the cardiac myocytes. These electrical pulses act as stimulus to activate the cardiac myocytes action potential [78]. The electrical activity of cardiac myocyte in terms of membrane potential variations can be manipulated as:

$$\tau V^{'} = k(V - V_r)f(V - V_{th}) - u + V_{AV} + V_{SA} + RI \tag{5.1}$$

$$\tau u^{'} = a(bV - u) \tag{5.2}$$

V_{AV} = Potential pulse through AV node = $V_\beta e^{-(t-n\tau)/T_k}$
V_{SA} = Potential pulse from SA node = $V_{Ca}e^{-(t-n\tau)^2/T_{Ca}}$
$I = I_{Na} + I_{NaL} + I_{to} + I_{CaL} + I_{Kr} + I_{Ks} + I_{K1} + I_{NaCai} + I_{NaCass} + I_{NaK} + I_{Kb} + I_{Nab} + I_{Cab} + I_{pCa} + J_{leak} + J_{rel} + J_{tr} + J_{up} + I_{stim}$
The activation of cardiac myocyte membrane potential towards upstroke and plateau phase can be expressed as:

$$\text{If } V \geq V_{th}\ ;\ \text{then } V = \begin{cases} V_\beta e^{-(t-n\tau)/T_K} & \forall\ t \\ V_{Ca}e^{-(t-n\tau)^2/T_{Ca}} & \forall\ (t+1) \end{cases} \tag{5.3}$$

The hyperpolarization and resting potential can be represented as:

$$\text{If } V \leq V_{APD_{50}}\ ;\ \text{then } V = \begin{cases} V_r e^{-(t-n\tau)/T_L} & \forall\ t \\ V_\alpha e^{-(t-n\tau)/T_{Na}} & \forall\ (t+1) \end{cases} \tag{5.4}$$

A brief description of parameters in Equations 5.1, 5.2, 5.3 and 5.4 are listed in Table 5.1. Stimulation current I is of prime importance in generation of action potential in cardiac myocytes [79]. A detailed discussion of cardiac currents is provided in Section 5.2 for illustration.

Cardiac action potential can be divided into six phases termed as stimulation, upstroke, polarization, plateau, repolarization, and resting [80]. The brief description of each phase is provided below.

- Stimulation: In this phase cardiac myocyte remain in resting state unless a brief potential from SA node or AV node approaches the fibers of cardiac myocyte [81]. Under this condition, leakage ions ($V_r e^{-(t-n\tau)/T_L}$) are active and can travel across the cell membrane. Due to this ionic transportation, cardiac membrane potential fluctuates and ready to capture stimulation as depicted in Figure 5.1a.

Table 5.1 Brief description of model parameters, notations and symbols used for cardiac myocytes

Symbols	Description
V	Cardiac action potential
k	Cardiac firing constant with respect to resting potential
V_r	Resting membrane potential
f	Cardiac firing constant with respect to threshold potential
u	Membrane recovery potential
V_{AV}	Potential generated by AV node
V_{SA}	Potential generated by SA node
R	Membrane resistance
I	Input current
V_α	Potential due to $\alpha-$adrenergic receptors
V_β	Potential due to $\beta-$adrenergic receptors
V_{Ca}	Potential due to calcium ions
n	Number of cardiac pulses
τ	Duration of cardiac pulse
a	Time constant of membrane recovery parameter
b	Time constant of membrane potential

- Upstroke: When local potential generated by SA node and AV node approaches the cardiac myocyte, sodium channels are opened [82]. As a result, a rapid influx of sodium ions ($V_\alpha e^{-(t-n\tau)/T_{Na}}$) takes place across cardiac membrane. This causes a rapid increase in membrane potential towards the positive side of action potential. Due to deposit of sodium ions inside the cardiac myocyte, an electric force of repulsion generated on intra-cellular calcium ions. The electrostatic gradient induces the force on adrenergic receptor gates and release the $\beta-$adrenergic receptors. The neurons sensitive to adrenergic receptors are triggered and signal is communicated to central nervous system by nerve impulse as depicted in Figure 5.1b. Due to slow movement of calcium ions, decay of $\beta-$adrenergic receptors is quite slow (Figure 5.1d). This gradually releases calcium ions from internal reserve of calcium called sarcoplasmic reticulum as illustrated in Figure 5.1a.

- Polarization: Due to rapid inward movement of sodium ions, sarcoplasmic reticulum channels are opened and calcium influx ($V_{Ca}e^{-(t-n\tau)^2/T_{Ca}}$) takes place along with release of potassium ions ($V_\beta e^{-(t-n\tau)/T_K}$). Since potassium ions are lighter than calcium, therefore, potassium efflux is more significant than calcium influx. As a result, membrane potential drops toward negative side [83]. This phase is called polarization of cardiac membrane as elucidated in Figure 5.1a.

- Plateau: Due to larger size of calcium ions, their influx is slower as compared to sodium and potassium ions. Therefore, membrane potential gradually decreases towards negative side. This stable state of membrane potential is called plateau phase. Plateau phase plays important role in synchronization of cardiac myocytes during excitation contraction coupling as depicted in Figure 5.1a. During plateau phase when membrane potential remains constant, release of beta-adrenergic receptors is blocked. As a result, a gradual decline of membrane potential occurs after plateau phase [84].

- Repolarization: When large amount of calcium is moved inside the cell, a strong force of

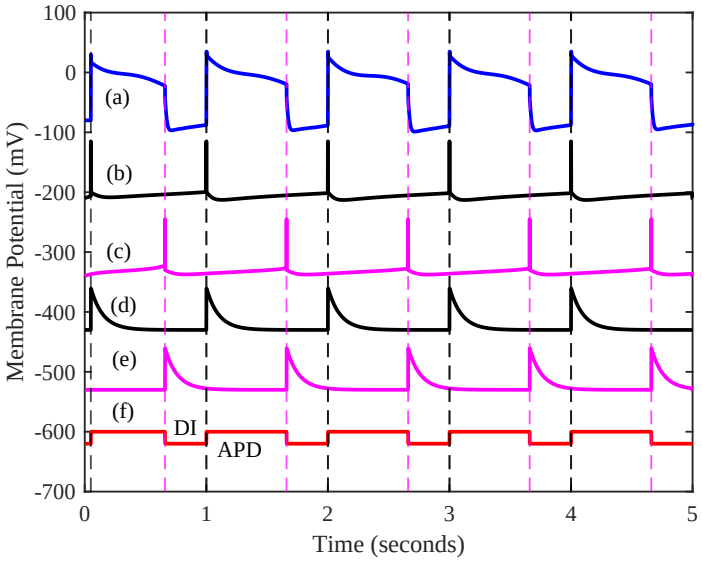


Figure 5.1 a) Action potential pulses generated by single cardiac myocyte (blue) b) Neuron activated by beta-adrenergic receptors (black) c) Neuron stimulated by alpha-adrenergic receptors (magenta) d) Potential pulse generated by release of beta-adrenergic receptors e) Potential waveform activated by release of alpha-adrenergic receptors f) Electrical pulses generated by cardiac myocytes to activate the neural network of brain (red).

repulsion compels potassium to move outward very rapidly [85]. This causes a decrease in membrane potential towards resting state. This negative tendency in membrane potential activates $\alpha-$adrenergic receptors. The neurons associated with alpha adrenergic receptors get fired and corresponding communication signal is delivered to central nervous system through impulses as illustrated in Figure 5.1c,e. Due to transportation of leakage ions ($V_r e^{-(t-n\tau)/T_L}$), membrane potential drops below the resting potential. This state of cardiac myocyte is termed as hyper-polarization [86].

- Resting: Due to transportation of leakage ions across cardiac membrane, action potential returns back to the resting membrane potential [87].

Plateau phase of cardiac action potential is responsible for heart rate variability, one of the key factors to estimate the individual's heart health [88]. In fact, plateau phase determines the action potential duration (APD) and diastolic interval (DI) of the heart cycle. APD is the duration of time for which action potential spike is initiated, while DI is the duration of time for which cardiac myocyte is in resting state. The relation between APD and DI is referred to as cardiac restitution function which determines duration of APD in terms of DI. restitution function is an exponential function that estimates the next APD from relaxing period DI of previous cardiac action potential. Therefore, larger APD is associated with larger DI and smaller APD is triggered with smaller DI [89]. This fact can be verified directly from warm up activity of an athlete. During exercise, the heart beats at faster rate, therefore, diastolic intervals are quite small. As a result, corresponding APDs are also closely packed over time scale. Whenever, heart rate exceeds from a certain limit, adrenergic receptors communicating the central nervous system activates the cardiac neural network. This cardiac neural network activates the sarcoplasmic reticulum reserve of heart to release more and more calcium into cardiac myocyte fluid to slow down the heart rate. Hence, cardio-neural network of brain and

heart interplay an important aspect of brain-heart interface.

This study is limited to electrophysiology replication of cardiac myocytes in the simplest possible manner to test the proposed spiking neural network model to extract the abnormalities from the heart. While dealing with complex morphological features of Purkinje fibers, we need to consider the molecular and cellular level hierarchy of voltage activated gates. This will make the cardiac myocyte model complex computationally as well as morphological while coupling with brain cells. To avoid such complexities, we restricted our assumptions to just the electrophysiological features of cardiac myocytes in their simplest form.

The closed loop control system describing the communication pathway between brain, heart and autonomic nervous system is depicted in Figure 5.2. Excitable cells are recognized as neurons and cardiac myocytes. The models capable of manipulating the electrophysiological details of neurons are described as GLIF, MAT, QIF and HEC model. Details of cardiac myocyte models not presented because we are dealing with neural network computation in current study. The best model in terms of Gamma factor and firing rate coefficients (HEC model in current scenario) is implemented to represent the neural network of autonomic nervous system.

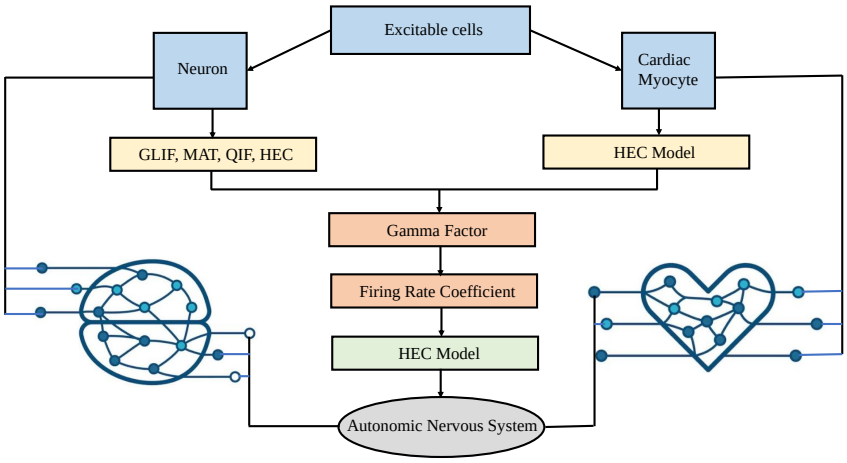


Figure 5.2 Flowchart describing the communication pathway between brain and heart via autonomic nervous system to control the functionality of both organs.

5.2 Cardiac Currents

The cardiac action potential is generated by various ionic current. The major ions that constitute cardiac ionic currents are sodium, potassium and calcium ions [90]. In this section, we discuss briefly the effects of these ionic currents on cardiac action potential.

5.2.1 Inward Sodium Current I_{Na}

The membrane of cardiac myocyte at resting state holds negative potential that varies from -90mV to -80mV depending upon the transportation of leakage ions across membrane. The current generated by pace-making cells from sin-atrial (SA) node and atrioventricular (AV) node reach the cardiac myocyte to stimulate the cell [91]. The membrane of cardiac myocyte contains protein molecules that act as ion channels. These ion channels are voltage sensitive and

can be activated at certain potential. Once the ion channels are activated, the transportation of ions takes place across the membrane. For instance, the activation potential of sodium channels is -40mV. Whenever electric potential of membrane reaches the threshold potential of sodium channels, the protein molecules are activated to allow the sodium ions to rush into the cell. The current generated due to inward movement of sodium ions is called inward sodium current denoted by I_{Na} as depicted in Figure 5.3.

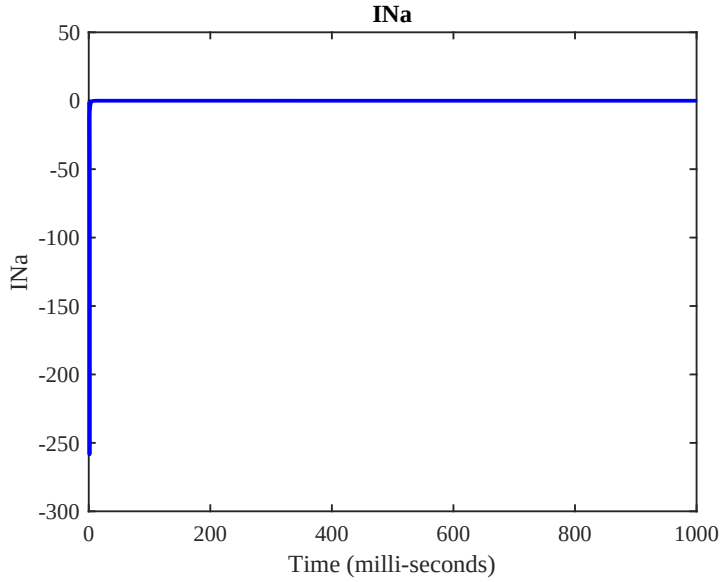


Figure 5.3 Inward sodium current

The sodium current initially starts from zero reference level and produces a negative spike. This spike is due to the interaction of sodium ions with negatively charged protein molecules. Once the sodium channels are opened, the influx of sodium ions attain its steady state level. Thus, the sodium ions constitute the positive upstroke of cardiac action potential. It should be noted here that inward movement of sodium ions is energy consuming [92]. The electrostatic force of repulsion between sodium ions needs to be handled by energy pumps that allow the further movement of sodium ions inside the cardiac myocyte membrane.

5.2.2 Late Sodium Current I_{NaL}

Late sodium ionic current is produced by special type of sodium activated channels. During the resting state of cardiac myocyte, a continuous pulses of current approaches cardiac myocyte membrane from SA node and AV node. These pulses cause membrane depolarization from resting to upstroke. The inward movement of sodium ions takes place due to opening of sodium channels. With an increase in sodium ion concentration inside the cardiac myocyte, membrane potential tends to increase rapidly. Finally, a stage is achieved when intracellular force of repulsion of sodium ions blocks the further transportation of sodium ions through membrane. This force of repulsion reduces the influx of sodium ions [93]. As a result, an impulse of negatively triggered sodium ions is generated, called late sodium current denoted by I_{NaL}. The waveform of late sodium current is plotted in Figure 5.4

The waveform depicted in Figure 5.4 starts from fast sodium current as described in Subsection 5.2.1. Due to rapid transportation of sodium ions inside the cell, electrostatic force of repulsion increased. As a result, the influx of sodium ions decreased due to previously installed positive

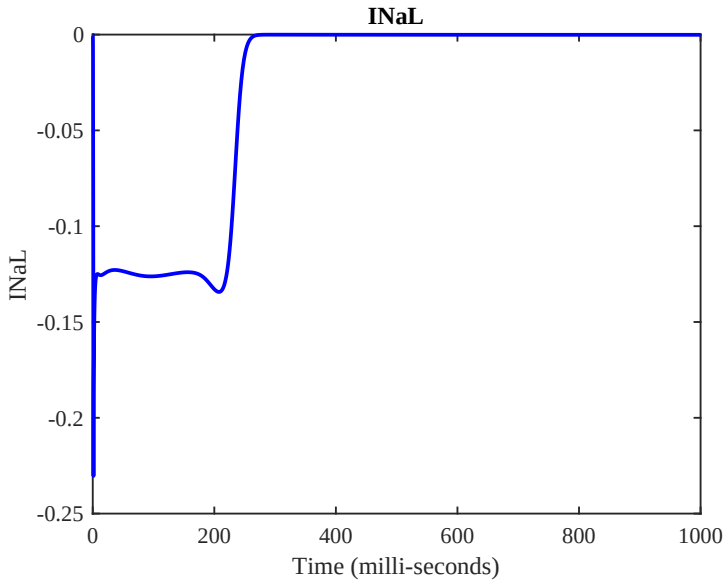


Figure 5.4 Late sodium current

entries of sodium ions. The decrease in sodium ionic current is illustrated in Figure 5.4.

5.2.3 Transient Outward Current I_{to}

The transient outward current is generated due to the electrostatic equilibrium established by sodium ions. The inward transportation of sodium ions through sodium ion channels is ceased when intracellular and extracellular force of repulsion is balanced. This point is the apex of cardiac action potential denoted by +40mV. At this stage, potassium sensitive ion channels are activated, and re-polarization of cardiac membrane takes place. Initially, the cardiac membrane contains a large amount of potassium ions inside the cell. The positive potential of potassium ions is balanced by the negatively charged protein molecules, that act as ion channels for transportation of specific ions. These ion channels are voltage sensitive and are triggered at certain potential [94]. The activation potential of potassium ion channels is 40mV approximately, depending upon temperature and concentration of potassium, sodium and negatively charged protein ions.

The rapid influx of sodium ions tends to increase the membrane potential towards 40mV potential that acts as threshold for activation of potassium ion channels. As a result, potassium ions transportation takes place from intracellular fluid to extracellular. The outward movement of potassium ions decreases the membrane potential towards the negative side. This phase of cardiac action potential is called re-polarization. The decrease in transient outward current is delineated in Figure 5.5. The transient state of ionic current is due to the presence of sodium ions in intracellular fluid [95]. The force of repulsion between positively charged sodium and potassium ions constitutes the re-polarization phase of cardiac action potential. The movement of potassium ions is much slower than sodium ions due to the size and molecular composition of potassium ions. Thus the intracellular movement of sodium ions is faster than the extracellular movement of potassium ions that can be observed from Figure 5.3 (fast movement of sodium influx) and Figure 5.5 (slow movement of potassium efflux).

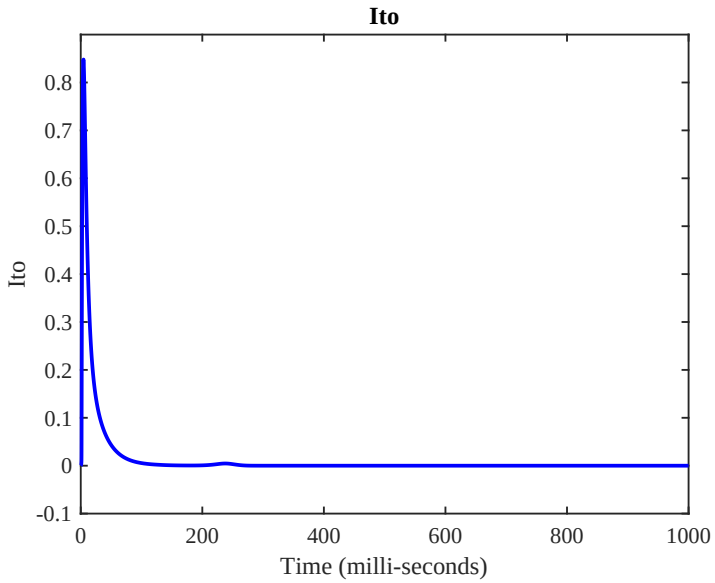


Figure 5.5 Transient Outward Current

5.2.4 L-Type Calcium Current I_{CaL}

The long-lasting calcium current I_{CaL} constitutes the plateau phase of cardiac action potential. In fact the release of calcium ions across the membrane is continuous process that takes long time due to larger size of calcium ions. As the early depolarization of cardiac membrane occurs, calcium channels are opened. This releases the calcium ions into the intracellular fluid of cardiac myocyte [96]. As a result, cardiac action potential takes plateau phase, rather rapidly converging the negative potential values.

L-type calcium current rapidly takes the negative value and gradually increase due to more release of calcium from sarcoplasmic reticulum reservoir of calcium ions [97]. As long as, the calcium channels are activated, the slow movement of calcium ions stabilizes the membrane potential and reaches the steady state value. The change is slope of L-type calcium current can be observed in Figure 5.6.

5.2.5 Rapid Potassium Current I_{Kr}

Rapid potassium current is related to the early re-polarization of cardiac membrane. When sodium ions are moving inside the cardiac membrane and potential tends to increase. At potential value (40mV), that activates the potassium ion channels. As a result, a rapid outward movement of potassium ions takes place. The rapid efflux of potassium is due to the electrostatic force of repulsion between positively charged sodium and potassium ions [72]. The potassium ion channels only allow potassium ions to move outward while blocking the movement of other ions across the cardiac membrane.

The waveform of rapid potassium current is manipulated in Figure 5.7. Rapid potassium current I_{Kr} quickly tends to increase as the potassium ion channels are activated. The increase in I_{Kr} is very rapid from 0 to 0.3 due to strong force of repulsion between positively charged sodium and potassium ions. As the efflux of potassium reduces the concentration of potassium in intracellular fluid. Therefore, potassium current gradually increases up to peak value of current. This gradual increase in potassium current is referred as delayed rectifier current [98].

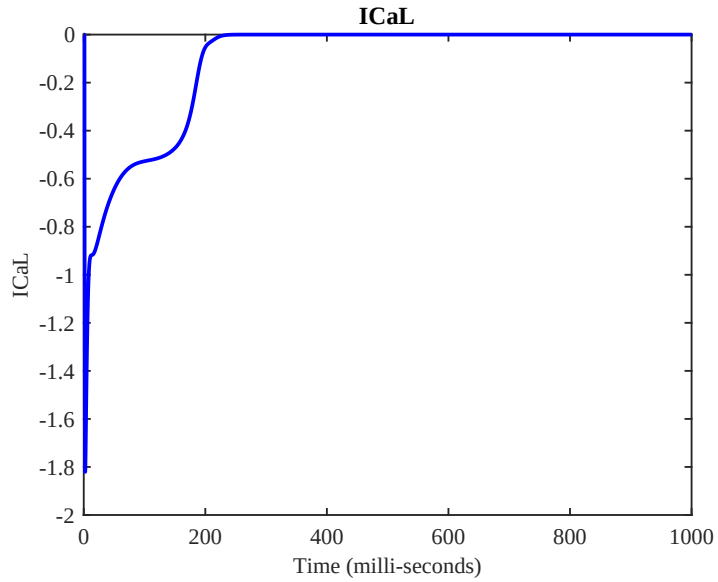


Figure 5.6 L-Type Calcium Current

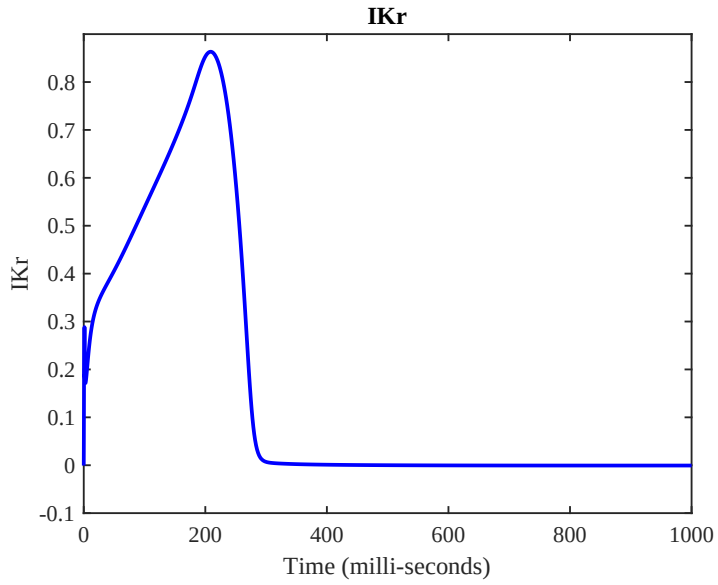


Figure 5.7 Delayed Rapid Potassium Rectifier Current

5.2.6 Slow Potassium Current I_{Ks}

Slow potassium current constitutes the plateau phase of cardiac action potential. During the cardiac action potential formation, extracellular movement of potassium slows down due to reduction of electrostatic repulsion between sodium and potassium ions [99]. The reduction in force of repulsion gives rise in slow potassium current. Slow potassium current gradually increases its amplitude to the maximum value and follows the similar path to decrease. This resembles the half wave rectifier that conducts the positive half cycle of alternating current.

The waveform of slow potassium current is delineated in Figure 5.8. The magnitude of current tends to increase due to movement of potassium ions across the membrane. After reaching the peak value of current, a decline in potassium current is observed. This constitutes the plateau

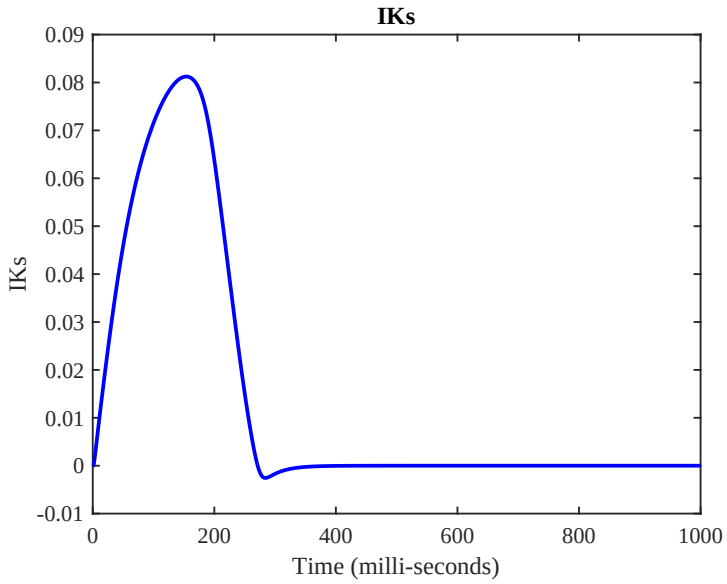


Figure 5.8 Delayed Slow Potassium Rectifier Current

phase of action potential [100].

5.2.7 Inward Potassium Current I_{K1}

Due to extracellular transportation of potassium ions, cardiac membrane lacks the potassium ion concentration to fire the action potential [101]. To recover the cardiac membrane, potassium ions need to move inside the cell to fire the action potential for next stimulation. Thus, inward movement of potassium is energy consuming and is carried by specialized protein channels that pump the extracellular potassium to intracellular fluid of cardiac membrane. Due to inward movement of potassium ions, a positive spike of current is generated [102].

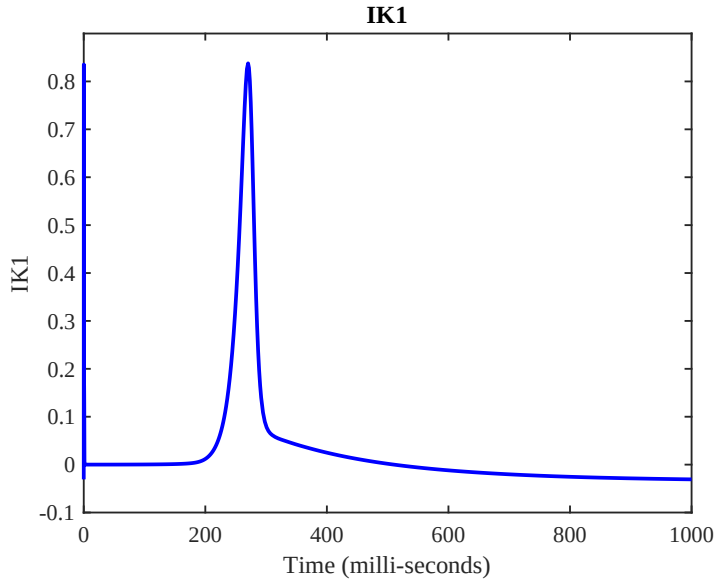


Figure 5.9 Inward Potassium Rectifier Current

The waveform of inward potassium current I_{K1} is depicted in Figure 5.9. The inward potassium current falls suddenly to its lowest value and after small delay it rapidly increase to its peak

value [103]. This rapid increase is due to protein molecules that are energetic to transport extracellular potassium to intracellular fluid.

5.2.8 Sodium-Calcium Exchange Current I_{NaCai}

Sodium calcium exchange current plays a vital role in cardiac action potential down stroke. The down stroke of cardiac action potential is equivalent to the polarization of cardiac membrane [104]. During the first phase when cardiac action potential is initiated, sodium is transported from extracellular to intracellular fluid. Similarly, the effect of calcium ions is opposite to the flow of sodium ions. The negative spike in sodium-calcium exchange current indicates the reverse direction of ionic flow that occurred during phase 1 and 2 of cardiac action potential. The reverse direction indicates the refractory period of cardiac cycle within which no action potential is generated even receiving the strong stimulation current. Therefore, cardiac membrane remains inactive during this period when sodium-calcium ions are being exchanged across the membrane [105]. This process of transportation of sodium and calcium ions is energy consuming. Thus, the energy level of sarcoplasmic reticulum decreases due to pumping of calcium ions along with sodium across the cardiac membrane.

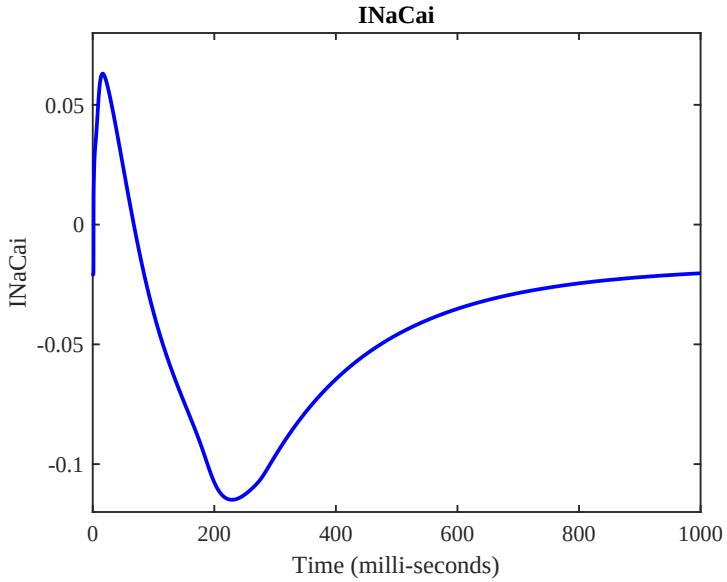


Figure 5.10 Sodium-Calcium Exchange Current

The waveform of sodium-calcium exchange current I_{NaCai} is illustrated in Figure 5.10. The current increases rapidly due to electrostatic force of attraction between sodium-calcium ions and negatively charged protein molecules of ion channels. However, after activation of ion channels, sodium and calcium ions are pumped into the cardiac membrane. This causes a net decrease in sodium-calcium flux and a negative peak of current is reached. From negative peak value, sodium-calcium exchange current increases asymptotically to achieve the equilibrium of cardiac membrane [106].

5.2.9 Subspace Sodium-Calcium Exchange Current I_{NaCass}

This current is due to the existence of residues of calcium leakage ions that can be transported sparsely across cardiac membrane. When cardiac myocyte fires upstroke pulse, these calcium ions are aligned with potassium ions [107]. Although, these calcium ions are labeled as leakage ions, however, after firing the upstroke these ions are now the part of delayed calcium ions.

Due to the presence of positive ions inside the cardiac membrane, an abrupt force of repulsion is experienced by calcium ions. This causes the net outward flow of positive ions across the cardiac membrane, in the form of negative current spike [108].

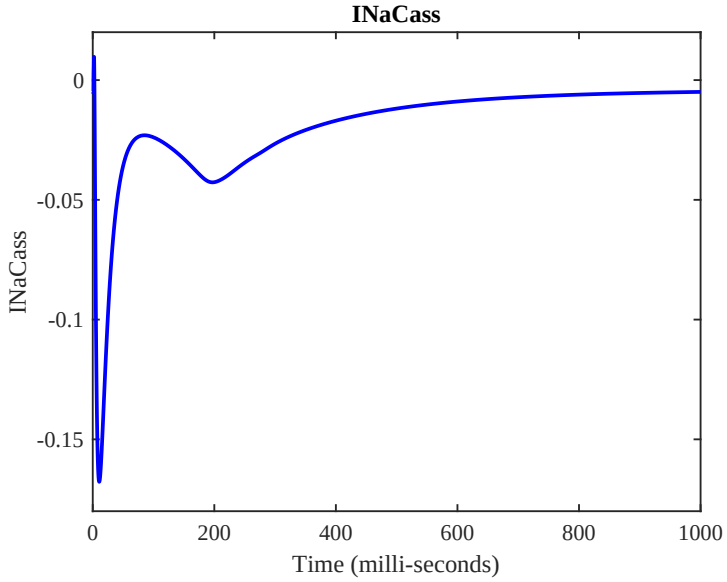


Figure 5.11 Sodium-Calcium Exchange Current of Subspace Component

The waveform of sodium-calcium exchange current of subspace component I_{NaCass} is delineated in Figure 5.11. Observe the negative spike of current due to electrostatic force of repulsion between positive ions. The net outward flow of positive charges creates negative charge inside the cardiac membrane [109]. However, cardiac membrane gains electrostatic equilibrium asymptotically due to slow exchange of calcium ions across the cardiac membrane. It should be noted that transportation of sodium-calcium is an energy consuming process. The protein molecules that transport sodium and calcium ions across cardiac membrane, consume energy extracted from sarcoplasmic reticulum [110].

5.2.10 Sodium-Potassium Exchange Current I_{NaK}

Sodium and potassium are the main constituents of cardiac membrane potential. Under resting condition, cardiac membrane contains intracellular potassium ions and extracellular sodium ions. The activation pulses from SA node and AV node reaching the cardiac myocyte tends to stimulate its membrane [111]. Due to activation of cardiac membrane, sodium ions rush into the cell through sodium ion channels. This causes an abrupt change in cardiac membrane potential in the form of upstroke. After cardiac spike is initiated, sodium ion channels are closed, and potassium channels are activated. As a result, outward movement of potassium ions takes place and down stroke of cardiac membrane is formed. Due to intracellular movement of sodium ions and extracellular movement of potassium ions, cardiac myocytes adopt a high impedance state. Under this state, cardiac myocyte is not able to accept any stimulus. Therefore, cardiac myocyte undergoes a reset process that causes the ejection of internal sodium ions by protein molecules [112]. This ejection of sodium ions from intracellular fluid causes negative current pulse as depicted in Figure 5.12.

The outward movement of sodium ions induces a net negative charge in intracellular fluid. The protein molecules holding negative charge in intracellular fluid attract the potassium

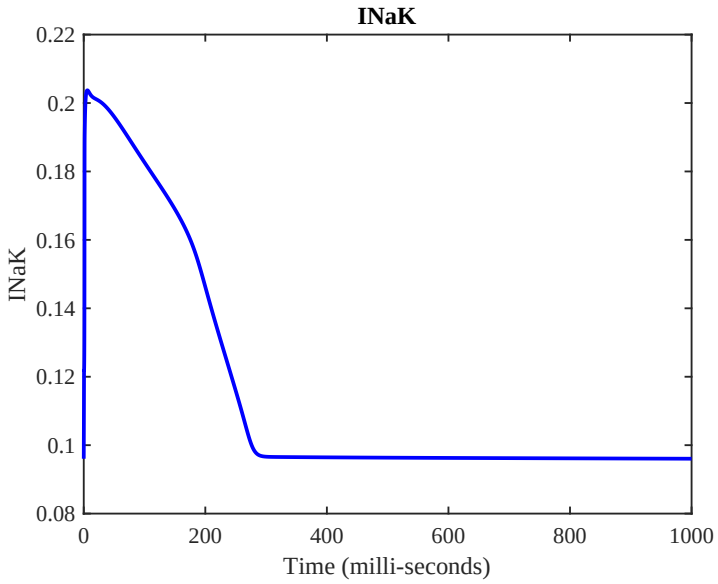


Figure 5.12 Sodium-Potassium Exchange Current

ions. Thus, the bidirectional transportation of sodium and potassium ions takes place until the cardiac membrane attains the equilibrium state [113]. The movement of sodium ions into cardiac membrane and potassium ions outside the membrane is a natural process that consumes a very small amount of energy. However, transportation of these ions in opposite direction is energy consuming. The current that arises due to transportation of sodium and potassium ions across cardiac membrane under the action of protein molecules, is referred as sodium-potassium exchange current.

5.2.11 Potassium Background Current I_{Kb}

The intracellular potassium ions are important to polarize the cardiac membrane after activation. Under resting state, intracellular fluid of cardiac membrane contains higher concentration of potassium ions [114]. When sodium-depending potassium channels are activated by external stimulation, potassium ions are transported from intracellular fluid to extracellular fluid. This causes an abrupt change in cardiac membrane potential towards the negative side. At the same time, when potassium ions efflux is high, a dedicated reservoir of potassium ions is activated to slow down the efflux of potassium ions to create the plateau phase of cardiac action potential. The current that arises due to dedicated reserve of potassium ions is called potassium background current denoted by I_{Kb}.

The waveform of potassium background current is depicted in Figure 5.13. The slope of potassium current is relatively greater as compared to the sodium ions due to the larger molecular mass and larger atomic size of potassium ions. Therefore, the slow transportation of potassium ions across cardiac membrane reduces the firing frequency of cardiac myocytes. This feature of cardiac myocytes is responsible to control the cardiac tachycardia and bradycardia [115].

5.2.12 Sodium Background Current I_{Nab}

Sodium background current is the consequence of upstroke of cardiac action potential. Under resting state of cardiac membrane, sodium ions are in higher concentration in extracellular fluid. After stimulation, sodium channels are activated, and sodium ions approaches the

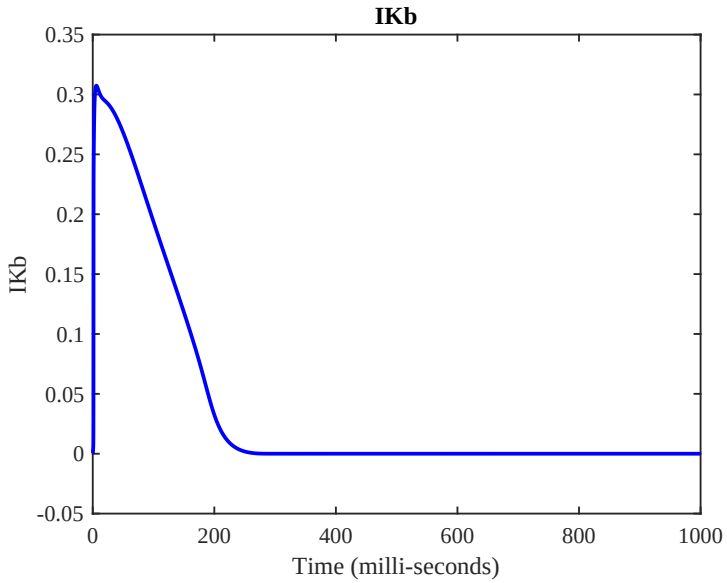


Figure 5.13 Potassium Background Current

intracellular fluid [116]. This causes an abrupt increase in cardiac membrane potential. The inward movement of sodium ions is a natural process that consumes very small amount of energy. Rather this transportation is due to electrostatic interactions between charges. When intracellular fluid is saturated by sodium ions, the further transportation of sodium ions is ceased. This causes the cardiac membrane inactive to further capture the input for activation. This state of cardiac membrane is called high impedance state [117].

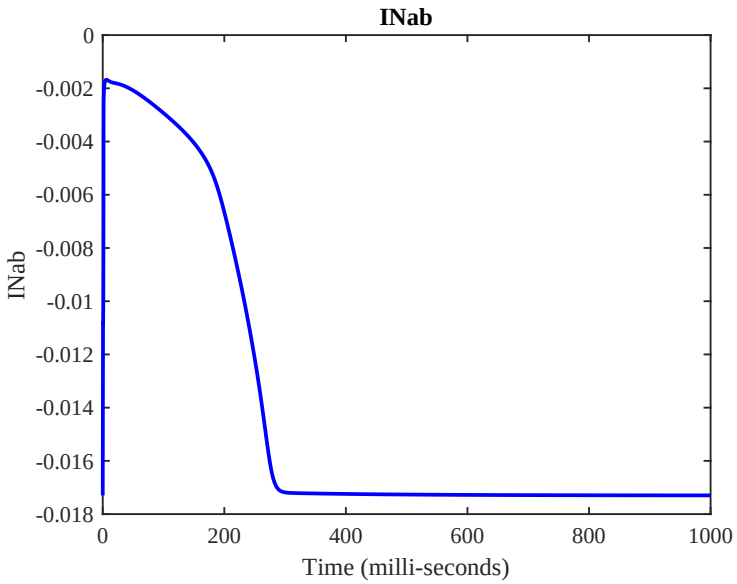


Figure 5.14 Sodium Background Current

Cardiac membrane remains active for the input current until the membrane is polarized. The intracellular transportation of sodium ions causes depolarization of membrane [118]. To repolarize the cardiac membrane, dedicated protein molecules are activated. These protein molecules act as energy pumps to transport the intracellular sodium ions to extracellular fluid. This transportation causes sodium background current I_{Nab} as depicted in Figure 5.14. Initially,

the magnitude of sodium background current is small due to the electrostatic interactions between positively charged sodium ions and negatively charged protein ions. Once the concentration of sodium ions in intracellular fluid is reduced, protein pumps more effectively transport further sodium ions to extracellular fluid. This causes increase in magnitude of slope of sodium background current [119].

5.2.13 Calcium Background Current I_{Cab}

Calcium ions play a vital role in controlling the firing frequency of cardiac myocytes due to their larger size and molecular mass as compared to sodium and potassium ions. During the formation of plateau phase, a net inward movement of calcium ions takes place from dedicated reserve of calcium, sarcoplasmic reticulum (SR). The opening of SR channels decides the duration of plateau phase [120]. Once the calcium is injected into the cardiac membrane, further transportation of calcium from SR is blocked until the calcium is removed from intracellular fluid. The inward movement of calcium is a natural process that consumes very small amount of energy that comes from electrostatic interactions between charges. However, extracellular transportation is energy consuming. Therefore, dedicated protein molecules that act as energy pumps are activated. These energy pumps transport calcium ions from intracellular to extracellular fluid. The transportation of calcium ions is highly energy consuming process due to its heavy and larger molecular size [121].

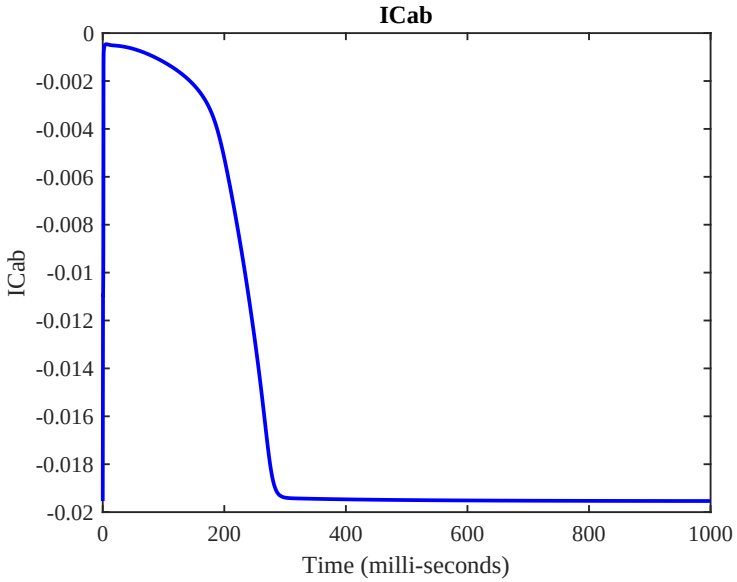


Figure 5.15 Calcium Background Current

The waveform of calcium background current is manipulated in Figure 5.15. Initially the magnitude of slope of I_{Cab} is small due to electrostatic interactions between positively charged calcium ions and negatively charged protein molecules. Once the concentration of calcium ions in intracellular fluid is reduced, protein pumps effectively transport the calcium ions from intracellular to extracellular fluid [122].

5.2.14 Calcium pump Current I_{pCa}

The role of calcium ions in the generation of cardiac action potential is of key importance. Unlike sodium and potassium ions, calcium ions are heavier and larger in molecular size. Moreover, charge on calcium ions is twice that of sodium and potassium ions [123]. Therefore,

transportation of calcium ions across cardiac membrane is slow compared to sodium and potassium ions. However, the effect of calcium ions on cardiac membrane potential is very significant due to twice the magnitude of electric charge. Under the resting state of cardiac membrane, calcium ions can easily be absorbed by the membrane. However, when upstroke of cardiac action potential takes place, cardiac membrane is highly depolarized. This causes a net gradient of electrostatic force of repulsion offered by sodium and potassium ions together, to cease the movement of calcium ions. This repulsive force activates the potassium ion channels. As a result, potassium rush to extracellular fluid by creating space for calcium ions [124]. The calcium ions require energy to overcome the electrostatic force of repulsion. The proteins molecules in the form of energy pumps are activated to transport the calcium ions into the cardiac membrane. The current that arises due to the pumping of calcium ions into cardiac membrane is called calcium pump current.

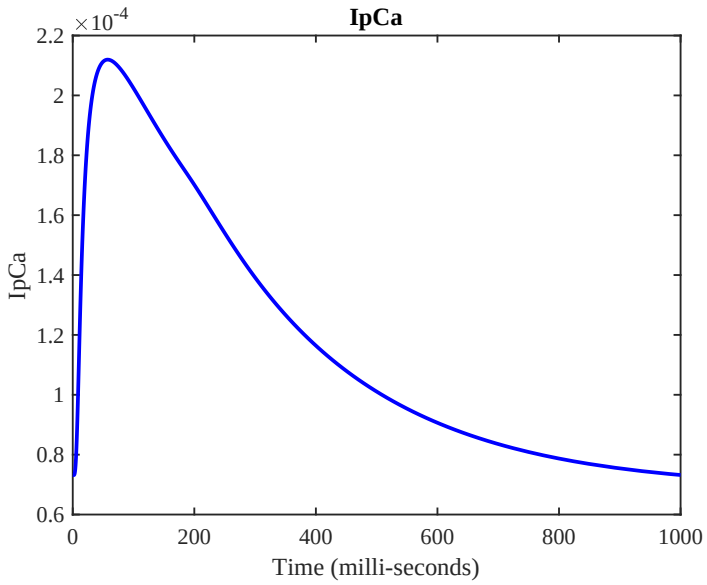


Figure 5.16 Calcium pump Current

The waveform of calcium pump current I_{pCa} is delineated in Figure 5.16. I_{pCa} initially increases abruptly due to concentration gradient. However, depositing calcium ions in intracellular fluid reduces further transportation of calcium ions due to electrostatic force of repulsion. Therefore, the magnitude of calcium pump current decreases asymptotically.

5.3 Calcium Fluxes

The most important feature of cardiac myocytes is the conversion of electrical pulses into mechanical function. The electro-mechanical function of cardiac myocytes is termed as excitation-contraction coupling that involves the complex dynamics of ions exchange. The role of calcium is very significant in excitation-contraction coupling due to its larger atomic size, larger atomic mass and carrying +2 charge on each ion equivalent to the protein molecules that acts as voltage regulators [125]. The calcium fluxes that involve excitation-contraction coupling are described briefly in the following subsections.

5.3.1 Calcium Leakage Flux from Network Sarcoplasmic Reticulum J_{leak}

Sarcoplasmic reticulum is the calcium internal reserve that acts as energy pump during cardiac action potential formation [126]. Under resting state, a small amount of all ions that involves cardiac action potential formation, exists in extracellular fluid. These ions act as signaling current to the ion channels that are activated at particular potential value [127]. The sarcoplasmic reticulum tends to release the small amount of calcium at resting state to maintain the equilibrium of cardiac membrane. This small amount of calcium released from sarcoplasmic reticulum is called calcium leakage flux denoted by J_{leak}.

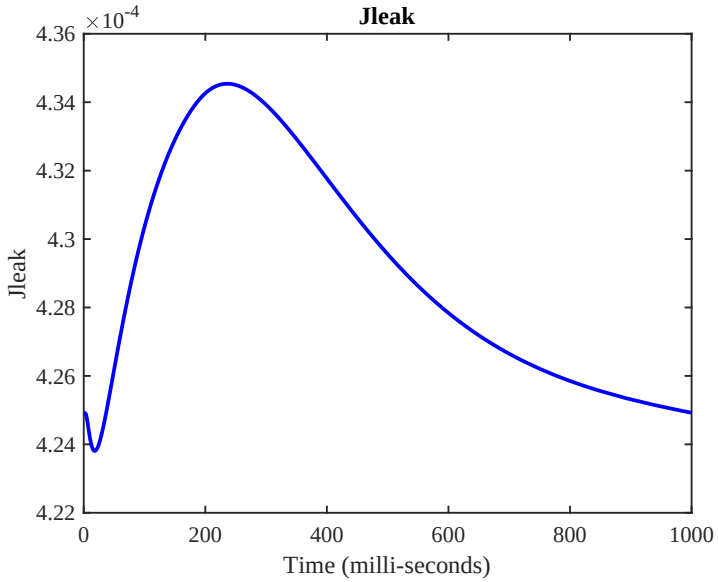


Figure 5.17 Calcium Leakage Flux from Network Sarcoplasmic Reticulum (NSR)

The waveform of calcium leakage flux from network sarcoplasmic reticulum is depicted in Figure 5.17. Initially, J_{leak} follows a short negative pulse due to force of repulsion between calcium ions and leakage ions present in extracellular fluid. The instant when leakage channels of sarcoplasmic reticulum are activated, calcium ions face the repulsive force. Thus J_{leak} is started from negative pulse indicating the opening of leakage channels [128].

Due to larger size and holding +2 charge, calcium repels the positive ions from extracellular fluid. This creates a gap in positive charges in extracellular fluid. As a result, a larger amount of calcium is released from sarcoplasmic reticulum to accommodate the concentration gradient. This causes an increase in J_{leak}, which can be observed in Figure 5.17. Once the concentration gradient of calcium is balanced by leakage ions in extracellular fluid, the electrostatic gradient is activated. Due to electrostatic interactions between positively charged calcium ions and leakage ions, calcium ions gradually became transported into sarcoplasmic reticulum. This causes the net decrease in calcium flux asymptotically that can be observed in Figure 5.17.

5.3.2 Calcium Release Flux from Junctional Sarcoplasmic Reticulum J_{rel}

Cardiac myocytes are strongly coupled with sarcoplasmic reticulum by active junctions. Whenever, sodium ions abruptly transported into cardiac membrane, a signal is transmitted to the sarcoplasmic reticulum to release the calcium ions in proportion to the signal strength [129]. Depending upon the signaling pathway activated by fast inward sodium current, calcium is released from sarcoplasmic reticulum. The flux of calcium released from junctional sarcoplasmic

reticulum is denoted by J_{rel}.

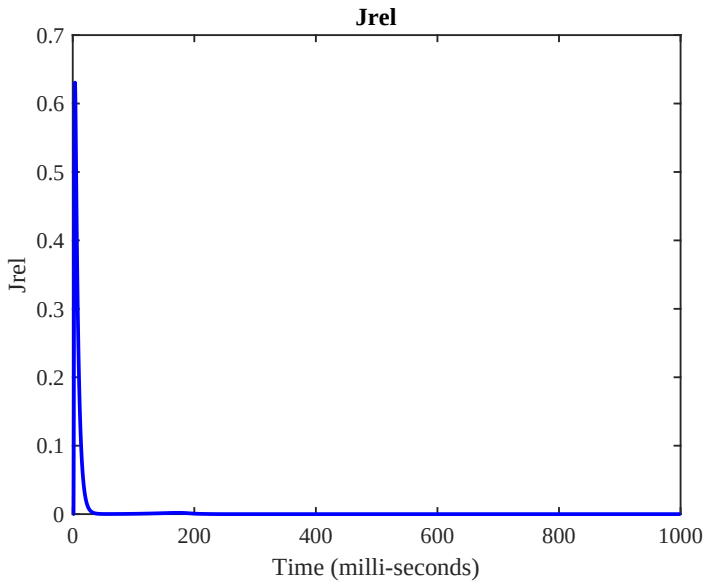


Figure 5.18 Calcium Release Flux from Junctional Sarcoplasmic Reticulum (JSR)

The waveform of calcium release flux from junctional sarcoplasmic reticulum J_{rel} is illustrated in Figure 5.18. The release of calcium in this case depends upon the sodium signaling. Thus J_{rel} is sodium dependent calcium flux. From cardiac action potential formation perspective, we know that sodium ions transported into cardiac membrane abruptly. This causes an upstroke in cardiac action potential. Similar behavior can be observed in J_{rel} depicted in Figure 5.18. Due to rapid inward flux of sodium ions, a strong signaling current is communicated to junctional sarcoplasmic reticulum. The junctional sarcoplasmic reticulum releases the amount of calcium in proportion to the signal strength. Thus a spike of calcium flux is observed in the form of J_{rel} as delineated in Figure 5.18.

Due to the larger size of calcium ions, micro-tubules of cardiac myocyte tend to expand. Moreover, carrying +2 charge repels the intracellular sodium and potassium ions. Thus, the abrupt release of calcium into intracellular fluid from junctional sarcoplasmic reticulum expands the cardiac membrane for short interval of time. This expansion is referred as excitation of cardiac myocyte [130].

5.3.3 Calcium Flux from Network to Junctional Sarcoplasmic Reticulum J_{tr}

The calcium reservoir in sarcoplasmic reticulum is due to the interaction of calcium ions and negatively charged protein ions. Due to sodium signaling, calcium from junctional sarcoplasmic reticulum decreases abruptly. This causes protein molecules to attract more calcium ions to establish electrostatic equilibrium inside sarcoplasmic reticulum [131]. Therefore, due to electrostatic gradient, calcium from network sarcoplasmic reticulum transported towards junctional sarcoplasmic reticulum. This calcium flux is denoted by J_{tr}.

The waveform of J_{tr} is depicted in Figure 5.19. The flux initially increases abruptly due to electrostatic interactions. Once the electrostatic equilibrium is established, the concentration gradient is activated. Therefore, a reverse flux of calcium takes place that reduces the calcium concentration. This process continues until concentration gradient vanishes. Thus the behavior of asymptotic decay is observed in Figure 5.19. The asymptotic behavior of calcium transporta-

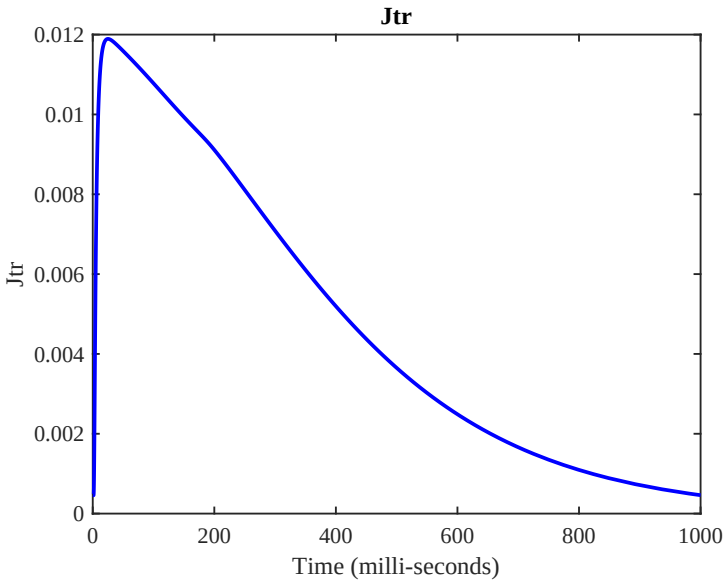


Figure 5.19 Calcium Flux from Network Sarcoplasmic Reticulum (NSR) to Junctional Sarcoplasmic Reticulum (JSR)

tion across sarcoplasmic reticulum enhances the time interval of cardiac excitation. Therefore, network of cardiac myocytes synchronized in this manner can take more blood to pump.

5.3.4 Calcium Uptake Flux from Cytosol to Network Sarcoplasmic Reticulum J_{up}

The transportation of calcium from network to junctional sarcoplasmic reticulum is a natural process that consumes small amount of energy due to electrostatic interactions and concentration gradient. Due to this transportation, calcium concentration in network sarcoplasmic reticulum is reduced. To maintain concentration equilibrium in network sarcoplasmic reticulum, calcium from cytosol reservoir is transported towards network sarcoplasmic reticulum. This transportation of calcium causes contraction of cardiac micro-tubules.

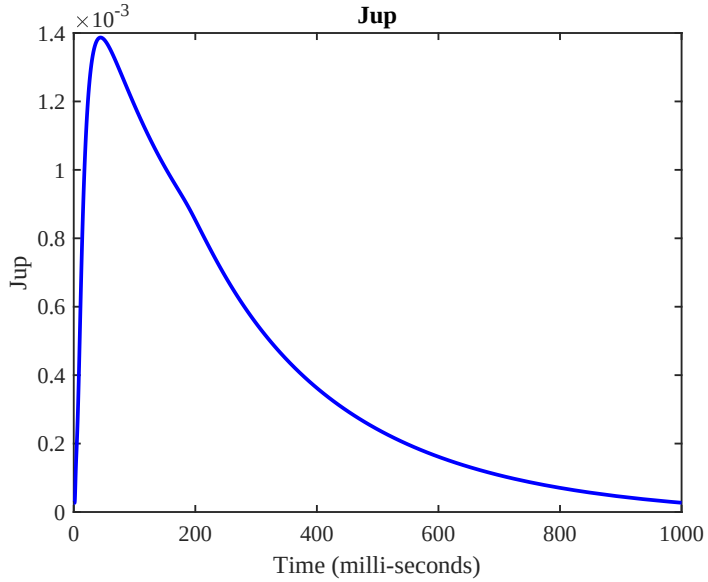


Figure 5.20 Calcium Uptake Flux from Cytosol to Network Sarcoplasmic Reticulum (NSR)

Table 5.2 Values of Model Parameters (MPs) for simulation of cardiac myocytes of different species

MPs	Human	Dog	Cat	Zebrafish	Guinea Pig	Rabbit	Mouse	Rat
a	0.03	0.03	0.07	0.5	0.03	0.03	0.03	0.03
b	-6	-6	-6	3	-2	-2	-2	-2
C	50μF	50μF	50μF	50μF	50μF	50μF	100μF	50μF
d	25	25	25	25	20	5	4	10
k	0.5	0.5	0.5	0.5	0.7	0.5	0.5	0.7
f	0.25	0.25	0.25	0.25	0.15	0.2	0.25	0.5
V_α	-60mV	-60mV	-60mV	-60mV	-46mV	-41mV	-60mV	-60mV
V_β	70mV	70mV	70mV	70mV	70mV	70mV	70mV	70mV
V_{Ca}	45mV	50mV	40mV	45mV	30mV	25mV	0	0
R_k	5MΩ	5MΩ	5MΩ	5MΩ	5MΩ	5MΩ	3.8MΩ	0.2MΩ
R_{Ca}	5MΩ	5MΩ	5MΩ	5MΩ	5MΩ	5MΩ	0	0
R	95MΩ	95MΩ	95MΩ	95MΩ	95MΩ	95MΩ	95MΩ	0

The waveform of calcium uptake flux from cytosol to network sarcoplasmic reticulum J_{up} is depicted in Figure 5.20. J_{up} increases abruptly due to electrostatic interactions between positively charged calcium ions and negatively charged protein ions. As a result positive peak in J_{up} is observed in Figure 5.20. Due to concentration gradient, calcium ions maintain concentration equilibrium gradually and reversibly. The behavior of concentration gradient is asymptotic as observed in Figure 5.20. Therefore, cardiac micro-tubules undergo a contraction process to pump the blood. Hence the electrical signaling from ion channels acts as mechanical function to activate the complex process of excitation-contraction coupling of cardiac myocytes.

5.4 Cardiac Action Potential of Different Species

Cardiac action potential is the electrical signal generated by cardiac myocyte under the action of strong stimulation current. The external stimulation current from sin-atrial node reaching the cardiac membrane activates the ion channels. This process depolarizes the cardiac membrane and action potential pulse is generated. The variation in waveform of cardiac myocyte action potential for different species depends upon the ion channel dynamics. The ion channels behavior under certain conditions is quite different. Therefore, the corresponding cardiac action potential varies from normal waveform as depicted in Table 5.2 for different species. The calcium concentration alters the plateau phase in membrane potential of each species and gradual decrease in calcium ion concentration in the form of calcium potential. In case of mouse and rat, plateau phase is negligible due to very small release of calcium from internal reserve of sarcoplasmic reticulum. Therefore, intra-cellular and extra-cellular dynamics of calcium ions are the key factors in the plateau phase of action potential generation of cardiac myocytes.

5.4.1 Cardiac Myocytes in Human

The action potential of cardiac myocytes in human heart is specialized in linking electrical activity with mechanical function. The mechanical function of cardiac myocytes is complex process that involves the interactions of ion channels in the form of excitation-contraction coupling. To develop the computational model for cardiac action potential of human cardiac

myocytes, we need to distinguish the ionic dynamics in cardiac membrane. The main ions in cardiac membrane potential generation in human cardiac myocytes are sodium, potassium and calcium ions. Sodium and potassium carry +1 electric charge while calcium ions contain +2 electric charge. The pace-making cells in sin-atrial node continuously generate current pulses that reach the cardiac myocytes. Under resting state, intracellular fluid contains potassium while extracellular fluid is enriched by sodium ions [132]. When strong stimulation current approaches the cardiac membrane, sodium channels are activated. This process allows the extracellular sodium to move inside the cell. Thus cardiac membrane tends to depolarize and potential of cardiac membrane increases due to transportation of positive ions into the cell as depicted in Figure 5.21.

Cardiac membrane is saturated by sodium ions and a strong electric potential is developed across membrane. This potential activates the potassium channels, allowing the intracellular potassium to move outside the cell. Meanwhile, sodium channels are closed, to block the outward flow of sodium. The extracellular movement of potassium drops the membrane potential causing the membrane to re-polarize. During re-polarization process, calcium ion channels are activated. A net influx of calcium takes place that gradually decrease the membrane potential as illustrated in Figure 5.21. This process regulates the plateau phase of cardiac action potential. The formation of cardiac action potential is due to three types of ions that generate certain potential across cardiac membrane. While modeling the cardiac membrane potential, we need to consider the potential generated by these ions.

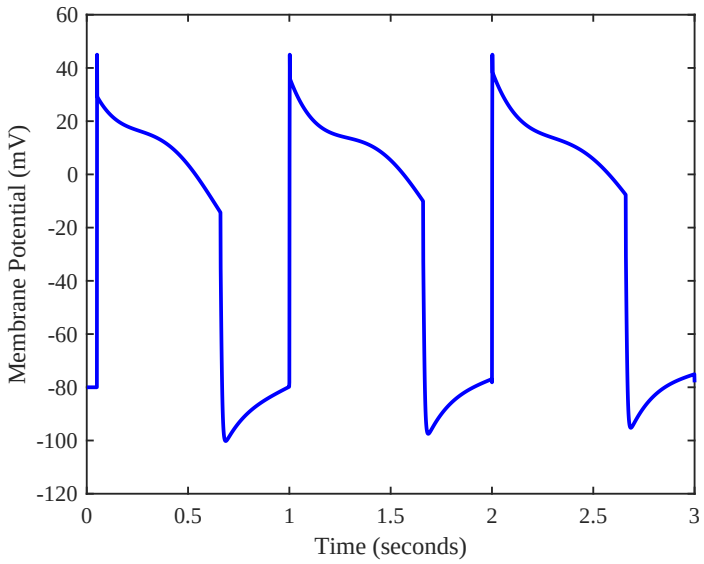


Figure 5.21 Action potential of human cardiac myocyte

The mathematical model of human cardiac myocyte is defined by Equations 5.1, 5.2, 5.3 and 5.4. In Table 5.2, the potential generated by potassium, sodium and calcium ions across cardiac membrane is denoted by V_α, V_β and V_{Ca} respectively. The value to V_α is negative due the fact that although potassium ions are positively charged, however their effect of cardiac membrane in negative. Similarly, the effect of sodium and calcium ions on cardiac membrane is increasing, therefore, V_β and V_{Ca} are taken positive. The effect of calcium potential on plateau phase can be observed in Figure 5.21. For human cardiac myocyte action potential, plateau phase is raised by small amount due to higher concentration of calcium in network and junctional

sarcoplasmic reticulum. The time constant upstroke ions are denoted by a and its value is taken as 0.03. Similarly, the time constant of membrane recovery parameter u is denoted by b and its value is taken as -6. The negative value represents decaying of membrane potential from peak value. The recovery of membrane potential is an energy consuming process, carried by protein molecules that are negatively charged. These protein molecules act as energy pumps to transport the ions across cardiac membrane to recover the polarization of cardiac membrane. Therefore, the value of time constant b for membrane recovery parameter is assumed as negative.

5.4.2 Cardiac Myocytes in Dog

The cardiac action potential in dog is slightly different from human due to higher concentration of calcium. The mechanical function of cardiac myocytes in dog is much faster than human. The excitation-contraction coupling of cardiac myocytes in dog is controlled by calcium ions present in sarcoplasmic reticulum. Under resting state, cardiac membrane is in equilibrium with intracellular potassium and extracellular sodium ions. When cardiac membrane is depolarized by external stimulation current, sodium ions are transported towards intracellular fluid. This causes an upstroke of cardiac action potential. The influx of sodium ions generates a strong signaling pathway for calcium ions in sarcoplasmic reticulum [133]. As a result, a larger amount of calcium is released into intracellular fluid. Higher efflux of calcium raises the plateau phase of cardiac action potential in dog as depicted in Figure 5.22.

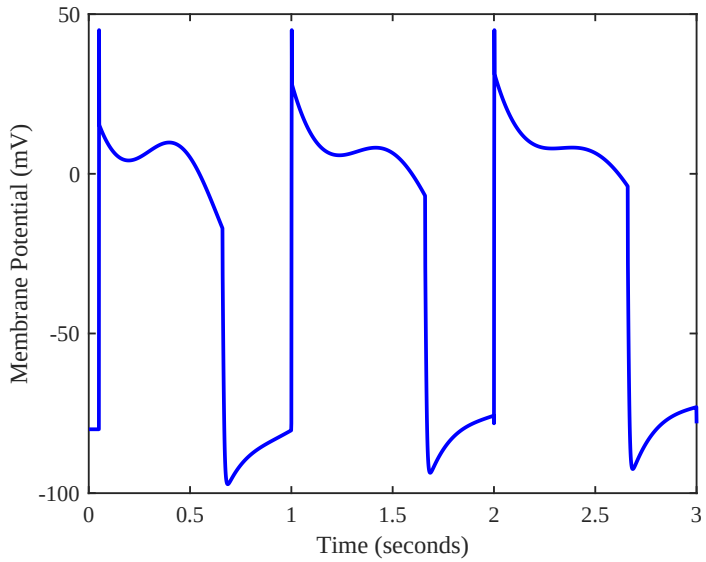


Figure 5.22 Action potential of dog cardiac myocyte

The higher concentration of calcium transported from sarcoplasmic reticulum to cardiac membrane of dog creates a concentration gradient. Moreover, negatively charged protein ions are activated inside the network sarcoplasmic reticulum. This causes a net force to transport calcium into sarcoplasmic reticulum. The strong electrostatic interactions between positively charged calcium ions and negatively charged protein molecules transfer the excessive calcium faster inside the sarcoplasmic reticulum. Moreover, concentration gradient also exerts strong force to transfer calcium ions inside junctional sarcoplasmic reticulum. The abrupt transportation of calcium ions causes the fast excitation-contraction coupling of cardiac muscles in dog. Therefore, the heart rate of dog is more stable than human, under the action of external

stimulation.

5.4.3 Cardiac Myocytes in Cat

Electrical response of cardiac myocytes in cat is due to sodium and potassium ions. The calcium transportation in cat cardiac myocyte is slow, therefore, plateau phase is almost linearly decreasing as illustrated in Figure 5.23. Under resting conditions, sodium ions tend to move inside the cardiac membrane. When strong stimulation current approaches cardiac membrane, depolarization of membrane takes place. Sodium channels are opened, and sodium ions are transported into the cell. This increases the cardiac action potential in positive direction until potential peak is reached. At This point, sodium channels are closed, and potassium channels are activated [134]. As a result, potassium ions are transferred outside the cardiac membrane. This causes cardiac membrane to re-polarize and membrane potential decreases. During this early re-polarization after upstroke, a small amount of calcium is transported into cardiac membrane. This causes a faster decrease in cardiac action potential from plateau phase to down stroke as depicted in Figure 5.23.

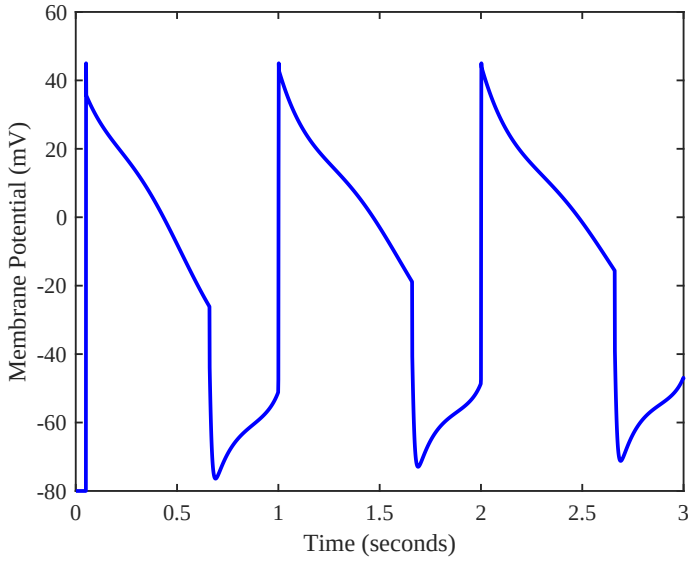


Figure 5.23 Action potential of cat cardiac myocyte

The variation in model parameters a and V_{Ca} for cat cardiac myocytes can be observed in Table 5.2. The value of time constant a that re-polarizes the cardiac membrane after upstroke is increased from 0.3 to 0.7. This causes a gradual inward flow of calcium from network sarcoplasmic reticulum to cardiac membrane. The gradual transportation of calcium from sarcoplasmic reticulum causes electrostatic and concentration gradient. Therefore, to maintain equilibrium for cardiac membrane to accept next strong stimulation, sarcoplasmic reticulum needs to be reset. For this purpose, protein molecules are activated that acts as energy pumps to transport calcium into network and junctional sarcoplasmic reticulum [135]. The transportation of calcium into sarcoplasmic reticulum brings the cardiac membrane to its resting state.

5.4.4 Cardiac Myocytes in Zebra-fish

The electrical response of cardiac myocyte in zebra-fish is manipulated in Figure 5.24. The cardiac action potential is initiated from -80mV resting potential. When cardiac membrane is in an equilibrium state, extracellular fluid is saturated with sodium ions. When strong

stimulation current approaches cardiac membrane, an upstroke of action potential is generated. When cardiac action potential reaches its apex, sodium channels are closed and net efflux of potassium takes place. During early re-polarization phase of action potential, calcium channels are activated. This causes the transportation of calcium ions into cardiac membrane [136]. As a result, a stable plateau phase of action potential is generated as depicted in Figure 5.24.

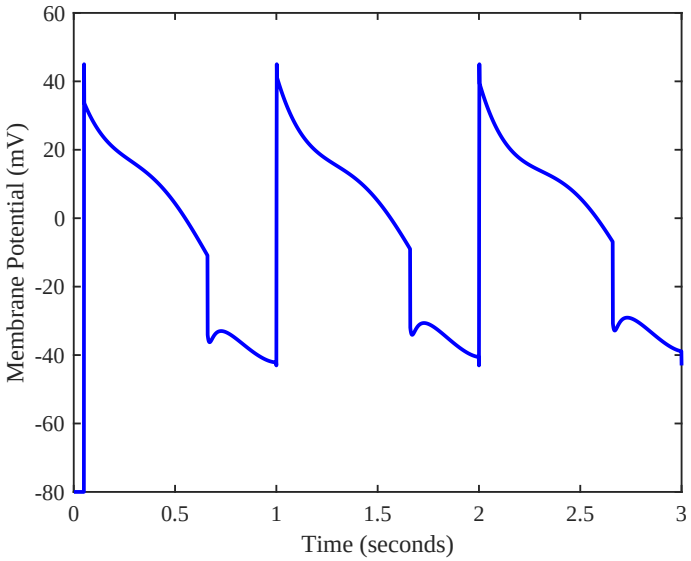


Figure 5.24 Action potential of zebra-fish cardiac myocyte

The computational model of cardiac action potential for zebrafish is defined by Equations 5.1, 5.2, 5.3 and 5.4. The values of model parameters are listed in Table 5.2. The value of cardiac membrane potential time constant a is taken 0.5, larger than human and dog due to late potassium and calcium ions. Similarly, time constant for membrane potential recovery parameter b is positive due to L-type calcium ions. L-type calcium and potassium ions tends to fire small potential spike after down stroke of cardiac action potential as depicted in Figure 5.24.

5.4.5 Cardiac Myocytes in Guinea Pig

The electrical response of cardiac myocyte in guinea pig is due to sodium, potassium and calcium ions. The sinoatrial node and atrioventricular node generate electrical pulses that approach cardiac myocyte to depolarize its membrane. The sin-atrial node contains natural pace-making cells that activate the cardiac ionic channels. On the other hand, atrioventricular node introduces delays in cardiac action potential during tachycardia. Under resting condition, intracellular fluid contains potassium while extracellular fluid is saturated with sodium ions. The electrical pulses from sin-atrial node reach the cardiac membrane. Depending upon strength of pulse, sodium ion channels are activated. As a result, extracellular sodium ions are transported into intracellular fluid [137]. This causes an abrupt increase in cardiac membrane potential as delineated in Figure 5.25.

Cardiac membrane is saturated by sodium ions and a strong electric potential is developed across membrane. This potential activates the potassium channels, allowing the intracellular potassium to move outside the cell. Meanwhile, sodium channels are closed, to block the

outward flow of sodium. The extracellular movement of potassium drops the membrane potential causing the membrane to re-polarize. During re-polarization process, calcium ion channels are activated. A net influx of calcium takes place that gradually decrease the membrane potential as illustrated in Figure 5.25. This process regulates the plateau phase of cardiac action potential. The formation of cardiac action potential is due to three types of ions that generate certain potential across cardiac membrane. While modeling the cardiac membrane potential, we need to consider the potential generated by these ions.

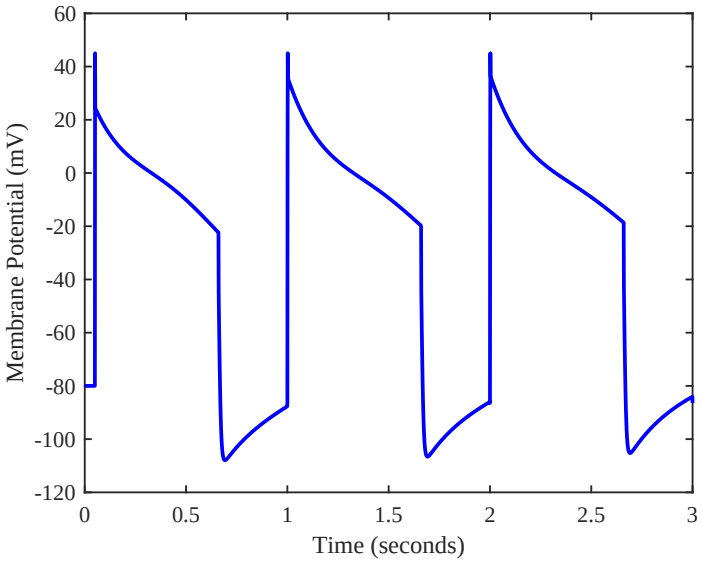


Figure 5.25 Action potential of guinea pig cardiac myocyte

The mathematical model of guinea pig cardiac myocyte is defined by Equations 5.1, 5.2, 5.3 and 5.4. In Table 5.2, the potential generated by potassium, sodium and calcium ions across cardiac membrane is denoted by V_α, V_β and V_{Ca} respectively. The value to V_α is negative due the fact that although potassium ions are positively charged, however their effect of cardiac membrane in negative. Similarly, the effect of sodium and calcium ions on cardiac membrane is increasing, therefore, V_β and V_{Ca} are taken positive. The effect of calcium potential on plateau phase can be observed in Figure 5.25. For guinea pig cardiac myocyte action potential, plateau phase is flattened by small amount due to lower concentration of calcium in network and junctional sarcoplasmic reticulum. The time constant upstroke ions is denoted by a and its value is taken as 0.03. Similarly, time constant of membrane recovery parameter u is denoted by b and its value is taken as -2. The negative value represents decaying of membrane potential from peak value. The recovery of membrane potential is an energy consuming process, carried by protein molecules that are negatively charged. These protein molecules act as energy pumps to transport the ions across cardiac membrane to recover the polarization of cardiac membrane. Therefore, the value of time constant b for membrane recovery parameter is assumed as negative. The calcium concentration in sarcoplasmic reticulum reservoir of guinea pig is lesser than human. Therefore, plateau phase of guinea pig cardiac action potential is flatter as compared to human.

5.4.6 Cardiac Myocytes in Rabbit

The electrical response of cardiac myocyte in rabbit is primarily due to sodium, potassium and calcium ions. The concentration of calcium ions in rabbit cardiac action potential is low as

compared to guinea pig. Therefore, plateau phase of rabbit cardiac action potential is slow decaying function of membrane potential as delineated in Figure 5.26. Under resting conditions, extracellular fluid of cardiac membrane contains higher concentration of sodium ions. When a strong stimulation current approaches cardiac membrane, an upstroke of action potential is generated. This causes an increase in cardiac membrane potential due to depolarization. The action potential reaching its apex causes potassium channels activation. As a result, re-polarization of cardiac membrane takes place. During re-polarization process, calcium channels are activated. The drop in cardiac potential possess a weak electrical potential on calcium ion channels. Therefore, small amount of calcium ions is transferred into intracellular fluid [138]. Due to low calcium concentration in intracellular fluid, cardiac membrane potential continuously decay from its peak value as depicted in Figure 5.26. However, the rate of cardiac membrane potential decay is slow due to larger size and molecular mass of calcium.

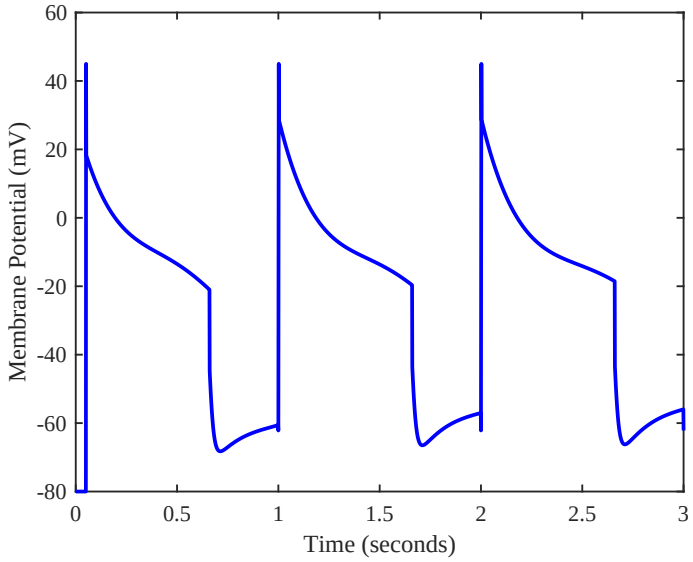


Figure 5.26 Action potential of rabbit cardiac myocyte

The values of model parameters of rabbit cardiac action potential are listed in Table 5.2. The cardiac membrane potential time constant a for rabbit is same as that of guinea pig. However, time constant b of membrane recovery parameter u is changed from -6 to -2 due to small amount of calcium transportation in intracellular fluid. Due to low calcium concentration, calcium induced potential value is also decreased. The value of calcium induced potential V_{Ca} is taken as 25mV for rabbit cardiac myocyte.

5.4.7 Cardiac Myocytes in Mouse

The cardiac action potential of mouse cardiac myocyte is manipulated in Figure 5.27. The waveform of mouse cardiac action potential is exponentially decaying function. The slope of time constant depends upon the efflux of calcium ions being transported into cardiac membrane. Under equilibrium state, intracellular fluid of mouse cardiac myocyte is enriched with potassium ions. When strong stimulation current depolarizes the cardiac membrane, calcium channels are activated. This calcium defines the frequency of mouse cardiac action potential. The strength of potassium current that re-polarizes cardiac membrane is weak, therefore, calcium channels of sarcoplasmic reticulum are partially activated [139]. This causes slow transportation of calcium across cardiac membrane.

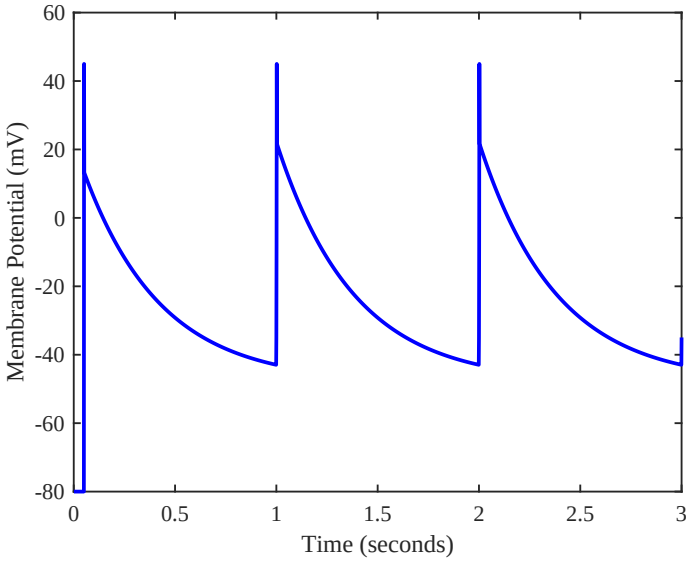


Figure 5.27 Action potential of mouse cardiac myocyte

The values of model parameters of mouse cardiac myocyte is listed in Table 5.2. The value of time constant b for membrane potential recovery parameter u is assumed -2 due to partially activation of calcium channels. Observe the value of membrane capacitance for mouse as 100μF. This value of membrane capacitance increases the decaying time constant of membrane potential. The value of calcium induced potential is taken zero due to low concentration of calcium ions transported by sarcoplasmic reticulum.

5.4.8 Cardiac Myocytes in Rat

The cardiac action potential of rat cardiac myocyte is depicted in Figure 5.28. The cardiac action potential of rat resembles with action potential of neuron. The absence of plateau phase in rat cardiac action potential is the very low concentration of calcium ions in network sarcoplasmic reticulum. Under resting state, extracellular fluid of cardiac membrane is saturated by sodium ions and small amount of calcium ions. The role of calcium ions in rat action potential generation is like leakage ions that can be transported across cardiac membrane. When cardiac membrane is depolarized by strong stimulation current, only small amount of calcium is transported in intracellular fluid [140]. Therefore, a very narrow plateau phase is observed in cardiac action potential of rat as illustrated in Figure 5.28.

The model parameters of rat cardiac myocyte are listed in Table 5.2. Observe the values of calcium induced potential V_{Ca} and resistance of potassium channels R_k. The low value of calcium concentration in intracellular fluid of rat cardiac membrane induces negligible potential that can be approximated as zero. Similarly, low resistance of potassium channels indicates fast movement of potassium ions from intracellular to extracellular fluid. This causes an abrupt decrease in cardiac membrane potential towards polarization. The fast polarization and depolarization of rat cardiac action potential is depicted in Figure 5.28.

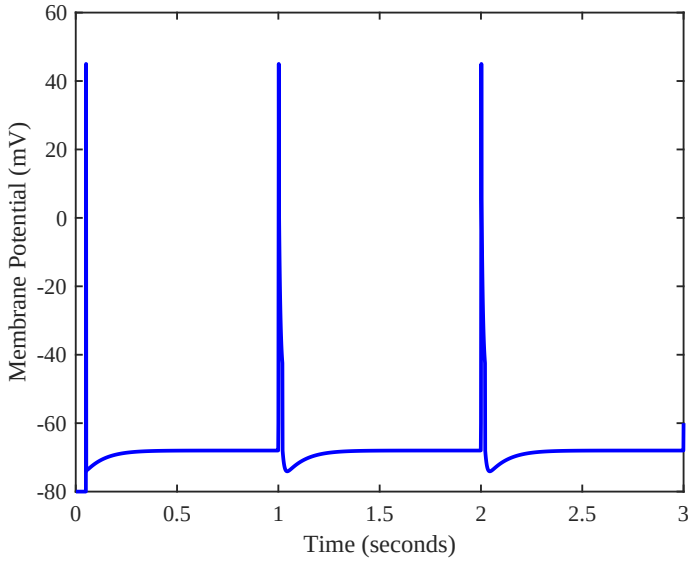


Figure 5.28 Action potential of rat cardiac myocyte

5.5 Cardio-Neural Network

Cardio-Neural Network refers to the communication pathways between brain, heart and autonomic nervous system. Unlike neurons, cardiac action potential is prolonged due to plateau phase. This phase is due to the transportation of calcium ions across cardiac myocyte membrane. While dealing with neural network, we consider the firing of neuron as point in time domain. In case of cardiac myocyte, this concept is contradictory. Therefore, point excitability model is not applicable for cardiac myocytes due to prolonged action potential duration.

To model the network of cardiac myocytes, we consider the features of adrenergic receptors. Whenever cardiac myocyte is fired, an upstroke of spike is generated along with beta adrenergic receptor. The neurons sensitive to beta adrenergic receptors also fired to send the signal to brain. Similarly, when down-stroke of cardiac action potential takes place, alpha adrenergic receptors are released. The neurons sensitive to alpha adrenergic receptors also fired to send the signal to brain. Thus, the brain holds the information of firing of each cardiac myocyte by alpha and beta neurons. Therefore, if we want to model the network of cardiac myocytes, we need to model the firing patterns of alpha and beta neurons [141].

For simulation of large-scale heart model, we assume a network of 1000 neurons coupled with cardiac myocytes. It is clear from previous discussion that firing of beta-adrenergic neuron, is the triggering of cardiac myocyte itself. To stimulate the cardiac myocyte, we assume random synaptic current within the range of cardiac ionic currents. For simulation of cardio-neural network, we assume alpha neurons (AN) and beta neurons (BN) depending upon the sensitivity of neurons towards corresponding adrenergic receptors. To distinguish between neurons, we associate a random variable r to cardio-neural network distributed uniformly over the interval [0,1]. If the random variable r returns the value 1, the corresponding neuron will be labeled as beta neuron, similarly, value of 0 will reflect alpha neuron.

To study the heterogeneity in cardio-neural network, we define the model parameters in terms

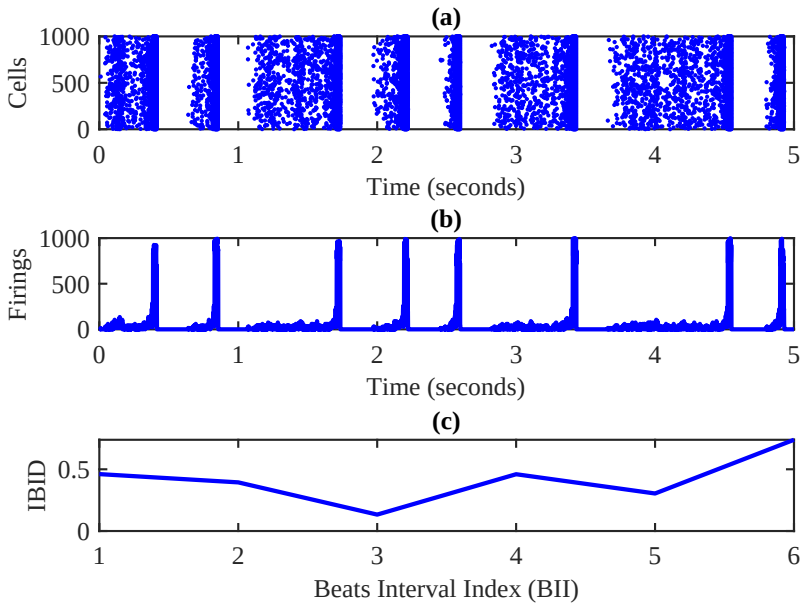


Figure 5.29 (a) Cardio-neural network of 1000 neurons synchronized with upstroke of 1000 cardiac myocytes. (b) Collective behavior of neural network to estimate the occurrence of heartbeat. (c) Inter-beat-interval-difference calculated from inter-beat-interval.

of random variable r as $a = 0.02 + 0.8r$, $b = 0.2 + 0.05r$, $c = -65 + 15r^2$, $d = 8 - 6r^2$ where, c is reset value of membrane potential and d is the step size of membrane potential recovery parameter u. The response of 1000 cardiac myocytes coupled with alpha and beta neurons is depicted in Figure 5.29. Each dot in Figure 5.29a represents the firing of beta neuron, manipulating the firing of corresponding cardiac myocyte associated with it. Figure 5.29b elucidates the superposition of firing of neurons at particular instant of time. This constitutes the spiking pattern of cardio-neural network equivalent to the heart beats. From heart beats we can calculate heart rate variability, one of the key indicator of healthy heart as illustrated in Figure 5.29c.

Heart rate variability (HRV) is the root mean square of successive difference (RMSSD) between heart beats. To find HRV, we first calculate the time indices of heart beats from Figure 5.29b. From Figure 5.29b, the indices of heart beats are [0.386 0.804 1.683 2.168 2.52 3.332 4.448 4.825]. To find the successive difference between heart beats, we calculate the inter-beat interval vector (IBI) as [0.418 0.879 0.485 0.352 0.812 1.116 0.377]. Next, we find the inter-beat interval difference (IBID) vector by evaluating the successive difference of IBI as [0.461 0.394 0.133 0.46 0.304 0.739]. The variance of IBID (RMSSD) is referred as HRV and is manipulated in Figure 5.29(c).
RMSSD(IBID) = Var(IBID) = 40ms.
Value of HRV varies from 30ms to 150ms depending upon the physique, age and fitness of the subject. A higher value of HRV refers to a healthy heart. Value of HRV drops gradually due to aging. Therefore, under normal conditions, 40ms HRV is referred to as a healthy elderly subject.

During the past few years, a remarkable development in the field of intelligent implants has been observed. Due to nature's masterpiece, the brain, with its exceptional accuracy, brain-

organ interfaces have been developed. One of the key outcomes of this study is the brain-heart interface, where heart control is monitored directly from brain signals. Thus, by introducing suitable implants, it is expected to reduce the risk of morbidity before its occurrence.

5.6 Pancreatic Cells

The number of victims of diabetes increasing across the globe due to abnormalities in glucose concentration in the blood. Researchers are investigating the phenomenon behind glucose abnormalities through clinical trials and computer simulations. It is believed that glucose homeostasis is established by the brain through the sympathetic and parasympathetic nervous system, however, the underlying mechanism is unclear. For this purpose, computational models of pancreatic cells have been proposed to understand the brain's control of pancreatic activities. Pancreatic cells are specialized to control glucose homeostasis by α, β, and δ pancreatic cells. α-cells release glucagon when glucose level in blood is low while β and δ-cells secrete insulin when glucose level in blood is high. The simplest model to estimate the electrical activity of pancreatic cells can be written as:

$$CV^{'} = k(V - V_r)f(V - V_{th}) - u + V_\alpha + V_\beta + RI \tag{5.5}$$

$$u^{'} = a(bV - u) \tag{5.6}$$

Glucagon induced potential can be defined as:

$$V_\alpha = V_{glu}e^{-(t-n\tau)/T_k}$$

Insulin induced potential can be manipulated as:

$$V_\beta = V_{ins}e^{-(t-n\tau)^2/T_{Ca}}$$

The ion dependent excitation current can be defined as:

$$I = I_{Na} + I_{CaL} + I_{CaN} + I_{CaT} + I_K + I_{K(ATP)} + I_{KA} + I_L + I_{SOC}$$

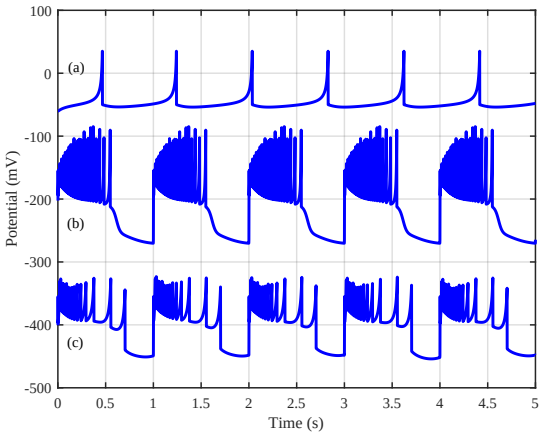


Figure 5.30 (a) Pancreatic α-cells, when the glucose level is low, the threshold of the cell is constant. (b) Pancreatic β-cells, when glucose level exponentially approaches the peak. (c) Pancreatic δ-cells, when glucose level exponentially decays from the peak.

Readers interested to find the details of ionic current I can consult [26]. After spike potential, from hyper-polarization to resting potential can be approximated as:

$$\text{If } V \geq V_{th}\ ; \ \text{ then } V = \begin{cases} V_p & \forall\ t \\ V_r & \forall\ (t+1) \end{cases} \tag{5.7}$$

$$V_{th} = V_{glu} e^{-(t-n\tau)/T_k} + V_{ins} e^{-(t-n\tau)^2/T_{Ca}} \tag{5.8}$$

For implementation of model described by Equations 5.5, 5.6, 5.7 and 5.8, Euler method

Table 5.3 Values of model parameters for simulation of pancreatic cells

Parameters	α-Cells	β-Cells	δ-Cells
a	0.03	0.02	0.02
b	-2	-5	-1
c	0	50μF	50μF
d	100	50	60
k	1	3	0.3
f	0.1	0.05	0.2
V_{glu}	0	35mV	35mV
V_{ins}	0	30mV	40mV
V_{Ca}	0	70mV	70mV
R_k	0	5MΩ	5MΩ
R_{Ca}	0	5MΩ	5MΩ
R	95MΩ	95MΩ	95MΩ

is utilized to evaluate membrane potential as $V(k+1) = V(k) + hV'(k)$, where $(')$ illustrates first-order derivative with respect to time. The spiking behavior of α-cells is delineated in Figure 5.30a, where the glucose concentration in the blood is quite low. Figure 5.30b illustrates β-cells when insulin secretion is exponentially increasing. Figure 5.30c depicts δ-cells when insulin level is decaying exponentially from the maximum value. Observe the effect of glucagon and insulin concentration on the threshold as illustrated in Equation 5.8. The values of model parameters for simulation of α, β and δ pancreatic cells are listed in Table 5.3.

5.7 Summary

In this chapter hybrid excitable cell model is extended to represent the electrophysiological behavior of cardiac myocyte. The electrical response of cardiac myocyte is divided into six phases depending upon the ion channel dynamics. These six phases are labeled as stimulation, upstroke, early re-polarization, plateau, hyper-polarization and resting. During each phase certain ion channels are activated and transportation of ions across cardiac membrane takes place. Unlike neuron, cardiac action potential is prolonged. The duration of cardiac action potential depends upon sodium, potassium and calcium signaling that completes the cardiac action potential cycle. The model is further extended to pancreatic cells by introducing glucagon and insulin induced potentials. The spiking behavior of α, β and δ pancreatic cells is reproduced, where glucagon and insulin concentrations alter the threshold of the cell. This extension provides a basis to study the control of glucose homeostasis by the brain through the autonomic nervous system.

KEY TAKEAWAYS

- SA- and AV-node pulses and α/β-adrenergic terms extend the HEC model to cardiac myocytes, whose action potential has six phases.
- Fourteen ionic currents and four calcium fluxes (J_{leak}, J_{rel}, J_{tr}, J_{up}) are reproduced and explained.
- Calcium released from the sarcoplasmic reticulum shapes the **plateau**; in mouse and rat it is almost absent.
- A **cardio-neural network** of 1000 myocytes coupled to α/β neurons yields heartbeats and a heart rate variability (RMSSD) of about **40 ms**.
- With glucagon- and insulin-induced potentials, the same model reproduces the spiking of pancreatic α, β and δ cells, which is a step towards modelling how the brain controls glucose levels.

CHAPTER 06

Conclusion and Future Directions

> *The best way to predict the future is to invent it.*
>
> — Alan Kay

QUESTIONS TO EXPLORE

1. How does the model of this thesis become a chip?
2. What do the NeuroBit64 chips for the brain, the heart, the pancreas and the kidney contain, and what do they show in simulation?
3. How do the reports of a chip reach a mobile phone, and what do the applications do with them?
4. What advantages can such chips and applications offer in future, and what still has to be done before they can detect disease in a subject?

IN THIS CHAPTER

6.1 From Model to Silicon: the NeuroBit64 Chip Family 86
6.2 Mobile Applications 92
6.3 Expected Advantages of the Chips and Applications 94
6.4 Future Directions 95

This thesis proposed one behavioural model, the Hybrid Excitable Cell model, for the excitable cells of the body, tested it against recordings of cortical neurons, extended it to the cardiac myocyte and the pancreatic cell, and coupled heart and brain in a cardio-neural network. The conclusion of that work is practical: the model is small enough to be built. This chapter therefore does not repeat the earlier chapters. It describes what has been built from them since, a family of chips called NeuroBit64 and the mobile applications that display their reports, what advantages such chips and applications can offer, and what remains to be done.

6.1 From Model to Silicon: the NeuroBit64 Chip Family

The binary representation of neural firing described in Section 4.3, and the cardio-neural network of Chapter 5, were carried one step further after the simulations of this thesis were completed: they were written as digital circuits. The result is a family of four designs, called NeuroBit64, that share one architecture. The first design is a brain chip; the other three are variants of it for the heart, the pancreas and the kidney. All four are described in Verilog, were verified against software models that use the same integer arithmetic, and are available in public repositories [142, 143, 144, 145]. None of them has been fabricated. This section reports what was designed and tested, and Section 6.1.7 states what has not been shown.

6.1.1 NeuroBit64: the Brain Chip

NeuroBit64 is the hardware form of the bit matrix of Section 4.3. Sixty-four neurons share one neuron circuit. In every tick each neuron reads an 8-bit input sample, updates its membrane value and decides 1 (fire) or 0; the 64 decisions form one 64-bit word, which is exactly one entry of the bit matrix, and the word is sent to a serial memory on three pins. The neuron is either a threshold neuron or a leaky integrate-and-fire neuron. In the serial version of the chip (NeuroBit64-S) a clock of 50 MHz gives 97,656 words per second. The complete test of 1.6 billion words, that is 102.4 billion decision bits (the number of neurons of the human brain used in Section 4.3), was run with the software model, and the Verilog description was shown to produce identical words in seven configurations.

NeuroBit64-S is the only member of the family for which a mask layout exists (Figure 6.1). The layout was produced with the open SkyWater 130 nm process design kit through the Tiny Tapeout flow [146]. It contains 3,172 standard cells on an area of about 0.33×0.22 mm, passed the design-rule and layout-versus-schematic checks without errors, and meets the 50 MHz timing with a margin of 4.45 ns in the slowest corner [142].

6.1.2 Organ Variants: Common Architecture

The three organ variants keep the time-shared principle of NeuroBit64-S and replace the neuron by an excitable cell of the organ together with its adrenergic neurons. Each variant contains 1000 organ cells. One cell is served in a slot of 8 clocks, exactly as one neuron in NeuroBit64-S, so that a tick of the whole network takes 8000 clocks; with a clock of 8 MHz one tick is one millisecond and the model runs in real time. The state of all cells circulates in a shift register, and one arithmetic circuit computes one forward-Euler step of the Hybrid Excitable Cell (HEC) model for the cell that is at the output of the register. The membrane potential is held in units of 1/16 mV and the recovery variable in units of 1/32 mV.

Three interfaces are common to the variants (Figure 6.2).

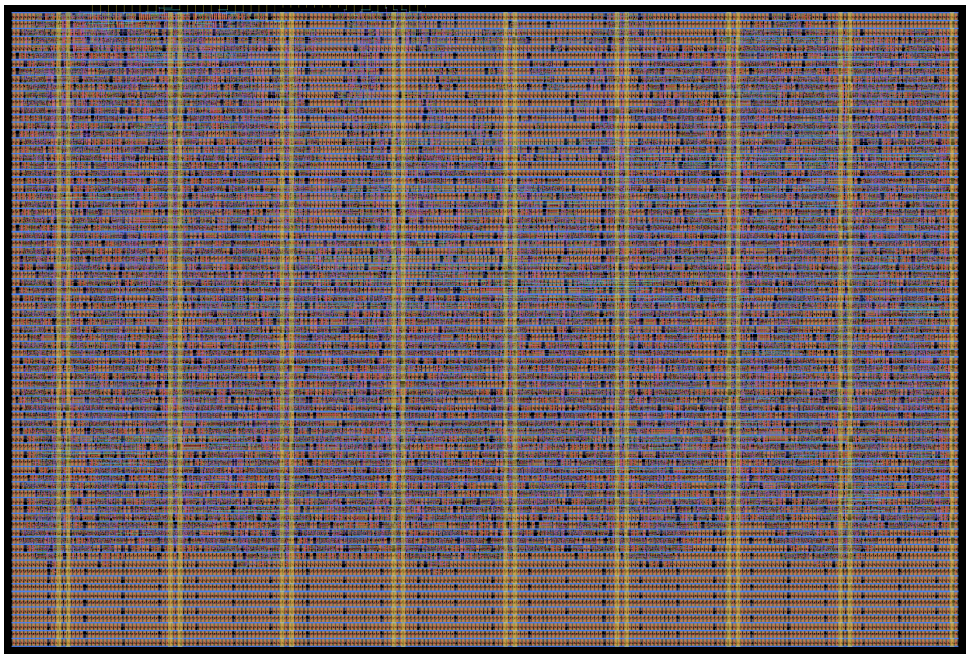


Figure 6.1 Mask layout of NeuroBit64-S in the SkyWater 130 nm process (3,172 standard cells, design-rule and layout-versus-schematic clean). The chip has not been fabricated.

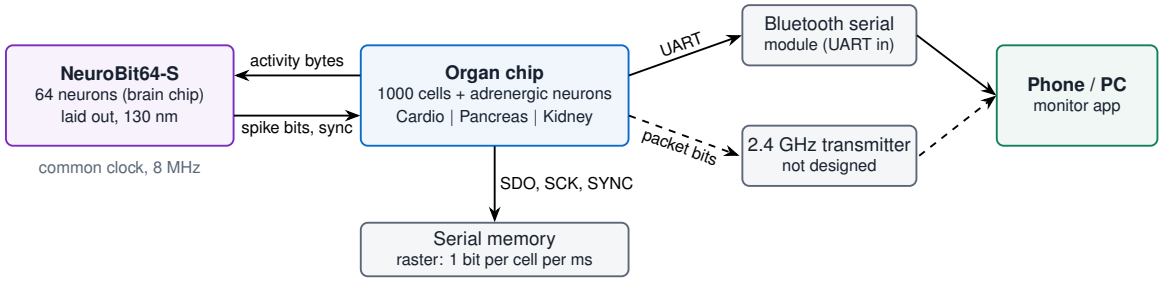


Figure 6.2 Connections of an organ chip. The brain chip and the organ chip exchange activity over three wires; the organ chip reports to a phone or computer through a Bluetooth serial module. Broken lines: the bit stream for a 2.4 GHz transmitter is generated, but the transmitter itself is not designed.

- *Brain link.* The 1000 cells are divided into 32 groups. The activity of every group is sent as an 8-bit sample to a NeuroBit64-S chip in the format of its input pin, so that 32 of its neurons receive the group activities and the other 32 receive the inverted values. In the opposite direction the organ chip reads the 64 decision bits of NeuroBit64-S; the ones of neurons 0–31 are counted as sympathetic drive and the ones of neurons 32–63 as parasympathetic drive. The neuron and the organ cell therefore communicate in both directions, which is the brain–organ interface of Figure 3.1 in hardware.

- *Telemetry.* Every 16 ms the chip sends a report of 16 bytes on a serial pin at 115.9 kbaud. A ready-made Bluetooth serial module carries the report to a mobile phone or a computer, where a web application displays it [147]. Every 128 ms the chip also produces the complete bit stream of a Bluetooth Low Energy advertising packet (whitening and 24-bit checksum included).

- *Raster output.* One bit per cell per tick leaves the chip in the serial format of NeuroBit64-S,

so the firing of the network can be stored as a bit matrix in the same way as the firing of the brain chip.

The properties of the three variants are summarized in Table 6.1.

Table 6.1 The NeuroBit64 family. Cell counts and areas are synthesis results for the SkyWater 130 nm standard-cell library; those of the organ variants are for the complete chips with 1000 units.

	NeuroBit64-S	Cardio	Pancreas	Kidney
Organ	Brain	Heart	Pancreas	Kidney
Cells	64 neurons	1000 myocytes	1000 islet cells	1000 nephrons
Adrenergic neurons	–	1000 α, 1000 β	687 α_2, 313 β_2	1000 α_1, 1000 β_1
State per unit (bits)	11	64	35	55
Clock	50 MHz	8 MHz	8 MHz	8 MHz
Standard cells	3,172	248,566	140,446	211,392
Cell area (mm^2)	0.029	2.25	1.27	1.92
Mask layout	yes	no	no	no
Repository	[142]	[143]	[144]	[145]

6.1.3 NeuroBit64-Cardio: Brain and Heart

NeuroBit64-Cardio [143] is the cardio-neural network of Section 5.5 as a circuit: 1000 cardiac myocytes, each coupled with one β-adrenergic and one α-adrenergic neuron. The myocyte follows Equations 5.1–5.4 with the human parameters of Table 5.2. At rest the membrane obeys the quadratic HEC equation. When the threshold is crossed the β-receptor potential V_β is released and the membrane follows the plateau waveform; when the decaying V_β has fallen below 5 mV the action potential ends and the α-receptor potential V_α is released. The β neuron of a cell integrates V_β and the α neuron integrates V_α. As proposed in Section 5.5, the β neurons therefore fire at the upstroke and the α neurons at the end of the plateau, and the chip measures the action potential duration as the time between the two bursts of the neuron populations (Figure 6.3). The 32 groups of cells form a conduction path: the first group has a pacemaker drive and every cell is excited by the upstrokes of its own and of the preceding group, so that an activation crosses the network in about 64 ms. A beat is counted when half of the cells have fired, which is the collective-firing criterion of Figure 5.29.

From these signals the chip derives the beat interval, the change of the interval from beat to beat and the action potential duration, and raises flags for tachycardia, bradycardia, irregular rhythm, a blocked activation, a prolonged action potential, a pause and a low participation of cells. Six conditions are built into the chip to exercise the flags. In 60 s of model time the normal condition gave 79 beats per minute with a root mean square of successive differences of 35 ms, close to the 40 ms obtained in Section 5.5, and raised no flag. The tachycardia condition (137 beats per minute), the bradycardia condition (50), the conduction-block condition (every second activation dies out at one group; 39 beats per minute in the remaining groups) and the condition with the thesis value of the potassium time constant (action potential of 601 ms) were flagged in every report after the first beats; the irregular condition was flagged in 72 % of the reports. With a NeuroBit64-S chip connected, the drive returned by its neurons changed the rate (for example from 50 to 62 beats per minute in the bradycardia condition), which shows that the loop between the two chips is closed. These are conditions of the model. They demonstrate that rhythm disorders of the cardio-neural network can be recognized from the adrenergic neurons alone; they are not a clinical evaluation.

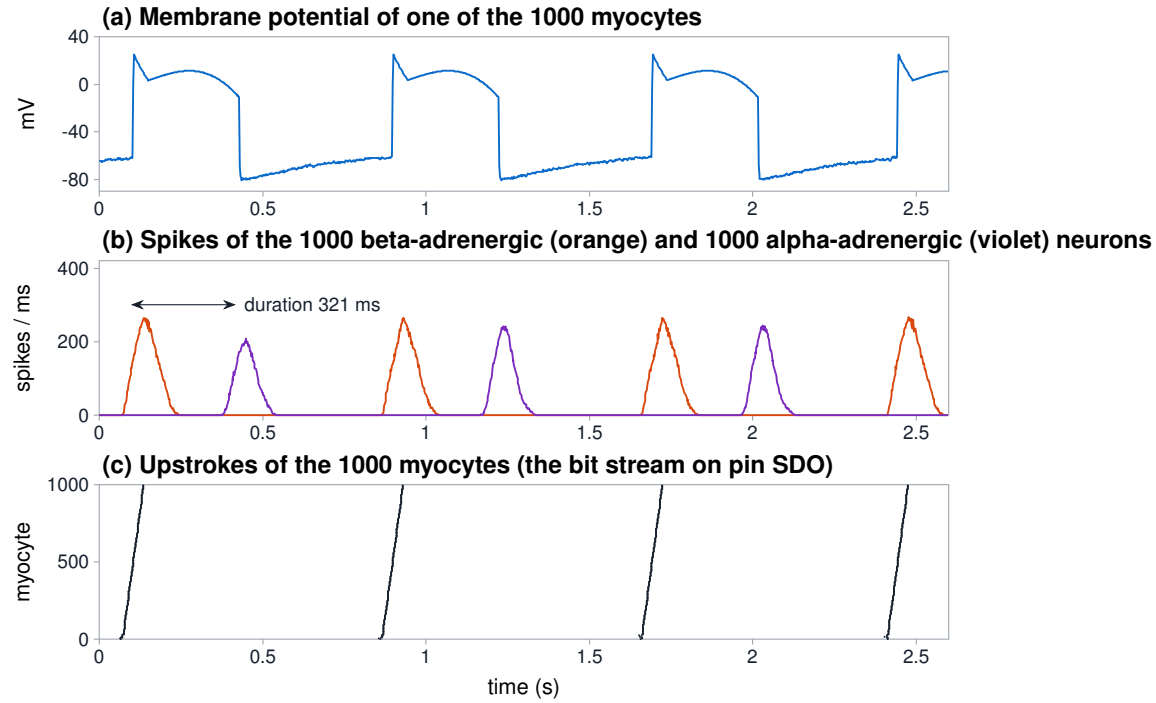


Figure 6.3 NeuroBit64-Cardio, normal rhythm (software model that is bit-identical to the Verilog description). (a) Action potential of one myocyte. (b) Population spikes of the β-adrenergic and α-adrenergic neurons; their distance is the action potential duration. (c) Upstrokes of the 1000 myocytes travelling through the 32 conduction groups.

6.1.4 NeuroBit64-Pancreas: Brain and Pancreas

NeuroBit64-Pancreas [144] contains the pancreatic cells of Section 5.6: 594 β-cells, 313 α-cells and 93 δ-cells with the parameters of Table 5.3. The glucagon-induced and insulin-induced potentials of Equation 5.8 are produced by the network itself: every spike of an α-cell adds to a glucagon level and every spike of a β- or δ-cell adds to an insulin level, and the two levels raise the threshold of the β- and δ-cells. The glucose concentration is an input of the chip. It drives the α-cells below 90 mg/dL and the β- and δ-cells above 100 mg/dL. Every cell has one adrenergic neuron driven by the sympathetic signal of the brain chip: an α_2-type neuron on β- and δ-cells, whose spikes inhibit the cell, and a β_2-type neuron on α-cells, whose spikes excite it; the parasympathetic signal drives the β-cells.

Figure 6.4a shows that the α-cells are active at low glucose and the β- and δ-cells at high glucose, as in Figure 5.30. Because the firing rates change monotonically with glucose, the chip can read the glucose level back from the activity of the cells (Figure 6.4b): over a sweep from 40 to 295 mg/dL the mean difference between the value read from the cells and the value given to the chip was 8 mg/dL for the healthy islet. The same comparison detects an islet that does not answer as it should. When 13 of 16 β-cells were removed, when the β-cells responded weakly, or when the α-cells did not respond, the chip raised the corresponding flag ("β-cells do not answer" or "α-cells do not answer"), and a high sympathetic tone was recognized in every report. The glucose value itself must come from a sensor. The companion project GlucoSense provides this part: a wearable glucose-sensor chip (GS-1) whose digital core already contains one α-, one β- and one δ-cell of the HEC model, and a mobile application that receives its measurements by Bluetooth [148, 149]. NeuroBit64-Pancreas accepts the glucose value of

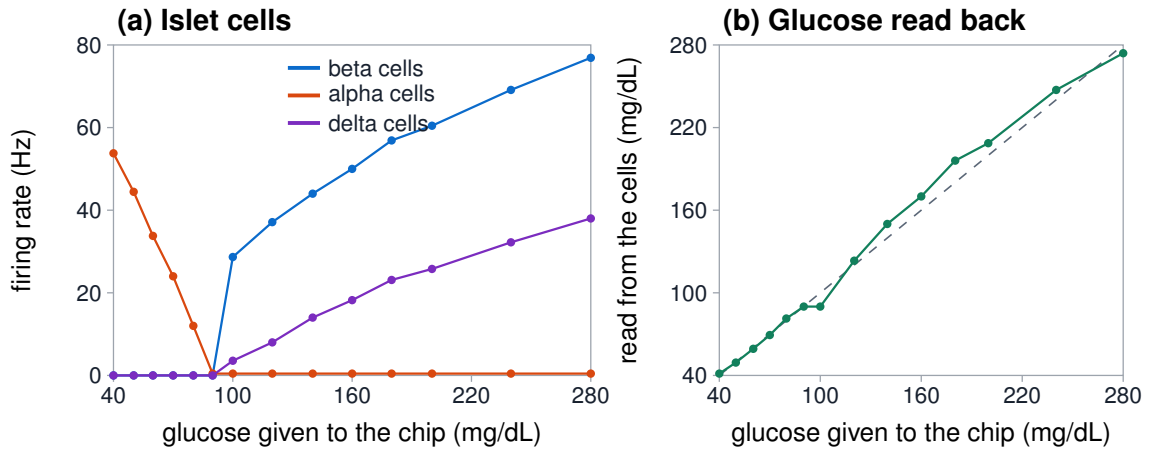


Figure 6.4 NeuroBit64-Pancreas, healthy islet. (a) Firing rates of the three cell populations at fixed glucose concentrations. (b) Glucose concentration read back by the chip from the firing rates against the concentration given to it.

such a sensor on its serial input.

6.1.5 NeuroBit64-Kidney: Brain and Kidney

The thesis contains no model of the kidney. NeuroBit64-Kidney [145] is therefore a proposal that applies the HEC model, with the regular-spiking parameters of Chapter 3, to a new organ. The chip contains 1000 nephron units. One spike of a unit stands for one quantum of filtrate; the adaptive threshold of the HEC model (Equation 3.5), which rises after every spike and decays again, plays the part of tubuloglomerular feedback. The perfusion pressure is an input. A renin level rises as long as the filtration of all nephrons together is below a set point and drives the working nephrons harder. Every unit has an α_1-adrenergic neuron, whose spikes reduce the filtration of the unit, and a β_1-adrenergic neuron, whose spikes release renin; both are driven by the sympathetic signal of the brain chip.

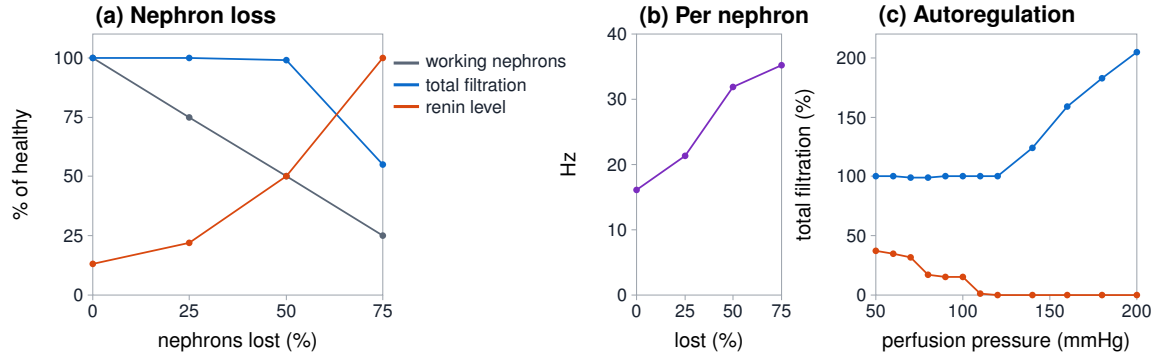


Figure 6.5 NeuroBit64-Kidney. (a) Loss of nephrons: the total filtration stays normal up to a loss of 50 % because (b) the remaining nephrons filter more and the renin level rises. (c) Total filtration (blue) and renin level (orange) of the healthy kidney at different perfusion pressures.

The behaviour that matters for early detection is shown in Figure 6.5. When 25 % or 50 % of the nephrons were switched off, the total filtration remained at 100 % of the set point, because the remaining nephrons increased their rate from 16 to 21 and 32 spikes per second.

A measurement of the total filtration alone would not show the loss. The chip counts the nephrons that are active and the filtration of each of them, and in both cases raised the flags "nephrons missing" and "hyperfiltration" together, which it reports as an early-loss pattern. Only at a loss of 75 % did the total filtration fall (to 55 %) and the renin level reach its limit. Low and high perfusion pressure and a high sympathetic tone were also distinguished. It must be stressed that this is a property of the model: whether such a pattern can be measured in a real kidney, through the renal nerves or otherwise, is an open question, and the model has not been compared with kidney recordings.

6.1.6 Verification and Size

Each organ chip was simulated with Icarus Verilog and compared with its software model. The comparison covered every report, every Bluetooth packet bit by bit, and a signature of the complete raster stream; in the runs with a brain chip the original Verilog description of NeuroBit64-S was connected and the signature of its output words was compared as well. All runs of Table 6.2 were identical. An independent receiver model accepted the checksum of every Bluetooth packet.

Table 6.2 Comparison of the Verilog descriptions with the software models.

Chip	Runs (with brain chip)	Simulated time	Reports	Bluetooth packets	Result
Cardio	6 (3)	8.8 s	550	201	identical
Pancreas	7 (3)	5.8 s	360	126	identical
Kidney	7 (3)	5.9 s	370	132	identical

The designs were synthesized with Yosys for the SkyWater 130 nm library (Table 6.1). The state register dominates the area. Figure 6.6 shows block floorplans drawn to scale from the synthesized areas. With pads the organ chips need between about 4 and 6 mm^2 of silicon, more than ten times the largest area offered by the flow that produced the layout of NeuroBit64-S, so their layout requires a die of their own on a multi-project wafer run.

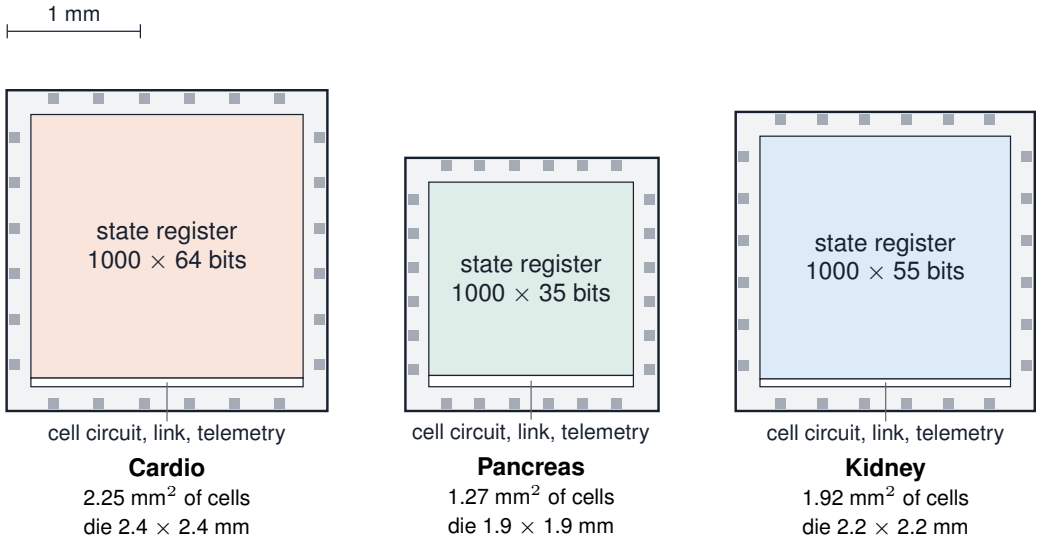


Figure 6.6 Block floorplans of the three organ chips, to scale (55 % utilization assumed). These are planning drawings, not mask layouts.

6.1.7 Limitations

- No chip has been fabricated. Only NeuroBit64-S has a mask layout. For the organ chips, placement and routing, timing analysis and simulation of the gate-level netlist have not been carried out.
- The radio transmitter is not designed. The chips generate the bits of a Bluetooth packet, and the path through a Bluetooth serial module to a phone has not been tried with hardware. The monitor applications have been tested with the simulated chips only.
- The disorders that the chips recognize are conditions built into the models. No recording from a patient or an animal has been used, and the chips are not diagnostic devices.
- Several elements were added to the models of the thesis in order to obtain a network that can be built: the conduction groups and the pacemaker drive of the heart chip; the glucose drive, the hormone levels and the read-out of the pancreas chip; and the complete kidney model. They are documented in the repositories and still have to be compared with physiological data.
- NeuroBit64-S is a general chip of 64 neurons. Which of its neurons are regarded as sympathetic or parasympathetic is a convention of the link, not a model of a brain region.

The hardware descriptions, test benches and documentation of the chip family were prepared with the help of AI tools where applicable, for convenience; every design was verified as described above.

6.2 Mobile Applications

A chip that listens to an organ is useful only if its report reaches the person who needs it. The mobile phone is the natural display: it is already in the pocket of the patient and of the physician, it has a Bluetooth radio, a screen and a connection to the network, and it needs no additional equipment. Three applications accompany the chips. All of them are web applications: they are opened as a page in the browser of an Android phone or a computer, need no installation, and use the Bluetooth and serial interfaces of the browser to talk to the hardware.

6.2.1 From the Chip to the Phone

The path of the data is the same for every organ chip. Every 16 ms the chip writes a frame of 19 bytes on its serial pin: two start bytes, the 16 bytes of the report and a checksum. A small ready-made Bluetooth serial module forwards the bytes to the phone. The application searches for the two start bytes, verifies the checksum, and decodes the report into the sequence number, the organ and its condition, the flags, the mean membrane potential, three spike counts and three measured values. Because the report is small, 62 reports per second are only about 1.2 kilobytes per second, which a Bluetooth Low Energy link carries easily. In the opposite direction the application can write an input to the chip, the glucose value for the pancreas chip or the perfusion pressure for the kidney chip, with a command of three bytes.

The applications can also run the chip themselves. The software model of each chip, which produces the same bits as the Verilog description, is part of the application, so the page shows a working chip before any hardware exists, and the same displays serve later for the fabricated

chip. This is how the applications have been tested so far. The applications are online at the addresses given with the references [143, 144, 145, 147]; the simulated chip starts as soon as the page is opened, and the address can select the organ and the condition, for example `?organ=kidney&cond=1` for a kidney with 25 % of its nephrons switched off.

6.2.2 The Organ Monitor

The NeuroBit64 Organ Monitor shows one chip at a time (Figure 6.7, centre and right). The user selects heart, pancreas or kidney and the source of the data: the simulated chip, a Bluetooth serial module, or a serial cable. For the heart the application displays the heart rate, the beat interval, the action potential duration and the root mean square of successive differences, which it computes from the intervals reported by the chip. For the pancreas it displays the glucose given to the chip, the glucose read back from the cells and the insulin level; for the kidney the number of working nephrons, the total filtration, the perfusion pressure and the renin level. Below these values the flags raised by the chip are listed by name, followed by the mean membrane potential, the spike counts and, for the simulated chip, the raster of the 1000 cells.

6.2.3 The Body Monitor

The NeuroBit64 Body Monitor [147] runs the whole family together (Figure 6.7, left): three brain chips, each connected to one organ chip through the brain link, and the heart, pancreas and kidney chips. Two rules of the application connect the organs to each other. The perfusion pressure of the kidney follows the rate of the heart, and the glucose given to the pancreas chip follows a glucose balance with meals, insulin and glucagon. These rules are simple assumptions and are not part of the chips.

An anomaly detector watches the complete picture. It combines three kinds of evidence: the flags of the chips; nine values compared with their range in the healthy model, for example the heart rate, the glucose concentration, the number of working nephrons and the renin level; and four patterns that appear only across organs, such as a slow heart together with a low perfusion of the kidney, or a high glucose concentration together with a weak insulin answer. The result is one of three states, normal, watch or abnormal, with the list of findings in plain words, an anomaly score and a log of events. In the scenario of a conduction block of the heart, for example, the detector reported the blocked activation, the slow heart, the fall of the perfusion pressure of the kidney to 67 mmHg, the rise of renin, and the heart–kidney pattern.

6.2.4 GlucoSense

GlucoSense [148, 149] is the application of the companion glucose-sensor project. It receives the measurements of a wearable sensor by Bluetooth, removes noise, converts the sensor current into a glucose concentration with a calibration, raises alerts for low and high values and produces reports. Its sensor chip, GS-1, contains one α-, one β- and one δ-cell of the HEC model. Together with NeuroBit64-Pancreas it forms a complete chain: the sensor measures glucose, the islet network shows how a healthy pancreas would answer to it, and the phone shows both.

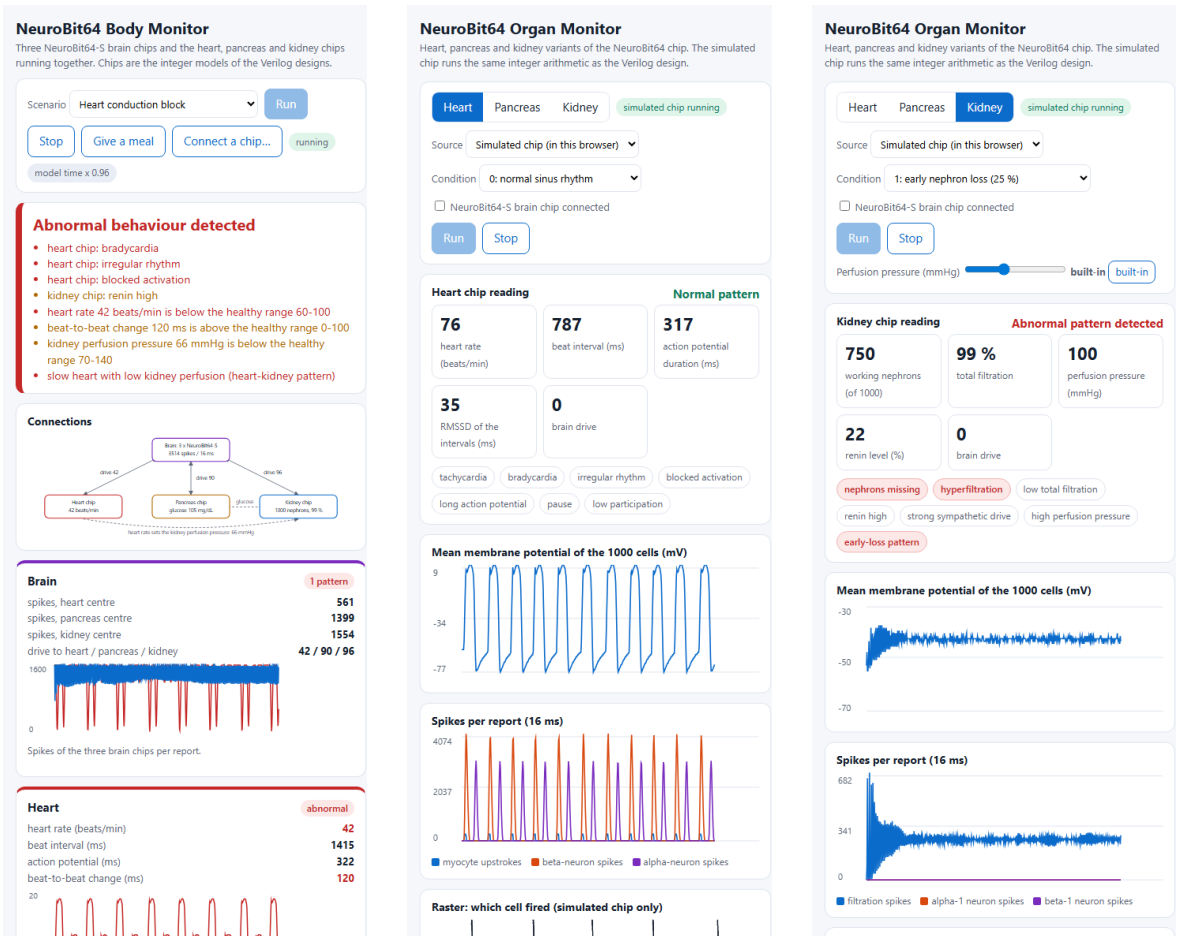


Figure 6.7 The applications at the width of a phone screen, running the software models of the chips. Left: Body Monitor in the conduction-block scenario. Centre: Organ Monitor, heart chip in normal rhythm. Right: Organ Monitor, kidney chip with 25 % of the nephrons switched off.

6.3 Expected Advantages of the Chips and Applications

The advantages listed here are those that the designs make possible. They are expectations that follow from the properties of the designs, and each of them has to be demonstrated with fabricated chips and with data from subjects.

- *Monitoring in real time and without interruption.* An examination in a clinic is a short sample of a long process: an electrocardiogram of a few minutes, a blood test a few times per year. Many disorders are intermittent or develop slowly and are missed by such samples. A chip that runs the model of the organ in real time, one step every millisecond, follows the organ continuously and reports every 16 ms.

- *Early detection.* The models look at the relation between signals and not at one number: the time between the β and α neurons of the heart, the answer of the islet to the measured glucose, the number of working nephrons against the load on each. In the simulations these relations changed before the conventional quantity changed; the loss of half of the nephrons, for example, left the total filtration normal. If the same holds in subjects, disease can be recognized at a stage in which treatment is simpler and cheaper.

- *Small size, low power and low cost.* Each chip is a purely digital circuit of a few square millimetres in a mature 130 nm process, without analog blocks or memory macros, and runs at 8 MHz. Such circuits are inexpensive to fabricate in quantity and can be supplied by a small battery, which is the condition for a wearable patch and, later, for an implant. The time-shared architecture is the reason: 1000 cells need one arithmetic circuit, not 1000.
- *No special equipment.* The display is a phone and the applications are web pages. A basic health unit, a general practitioner or the patient at home can use them without a dedicated instrument and without installing software, which matters most where specialists and laboratories are far away.
- *Results that can be explained.* Every flag has a definition in terms of a physiological quantity, for example "beat interval above 1000 ms" or "filtration of each working nephron above 125 %". A physician can check why the chip raised it. This distinguishes a model-based chip from a classifier that was trained on data and gives a label without a reason.
- *Privacy.* The signals are processed on the chip and displayed on the user's own phone. Nothing has to be sent to a server for the result to appear, so the data stay with the person they belong to unless that person shares them.
- *The whole body, not one organ.* Heart, pancreas and kidney influence each other, and cardiovascular disease, diabetes and kidney disease often occur together. Chips with a common link to the brain model and a common report format can be combined, and the Body Monitor shows that disorders can then be recognized in the relation between organs, which no single-organ device can see.
- *One architecture for many organs.* A further organ needs a cell model and a set of parameters, not a new chip architecture: the brain link, the report, the Bluetooth packet generator and the applications are reused. The effort for each new organ therefore falls.
- *Open and reproducible.* The designs, the models, the tests and the applications are public, and the layout of the brain chip was made with free tools. Other groups can repeat the results, correct the models and build on them, and students can follow the complete path from a model to a chip.
- *A testbed for the model.* Before any use on a subject, the chips are instruments for research: a model of an organ that runs in real time, connected to a model of the brain, in which a condition can be switched on and its signature in the neural signals observed within seconds.

6.4 Future Directions

Computer models are of key importance in diagnosis and treatment of morbidity related to brain and heart. The recent advancements in wearable devices enabled us to monitor the subject condition in real-time. With development in nano-electronics, nano-implants are developed that can detect morbidity by analyzing small signals from neural responses. The composite signals received from conventional devices used for electro-cardio-gram (ECG) and electro-encephalo-gram (EEG) contain correlated noise, encountered by neural firings. Thus,

we cannot distinguish the information related to abnormalities from composite signal of ECG and EEG. Therefore, we need to develop computational models of brain that can be coupled with organs in real-time to gather the neural data.

One of the manifestations of computational models is brain-heart interface. The computer model captures the real-time data of the brain and heart. The data is gathered from EEG and ECG electrodes and provided to the computer for analysis. The computer model reflects the interplay between brain and heart in real-time under given conditions. The difficulty in this approach is to distinguish the anomalies related to morbidity from composite signal. The development of nano-chips based upon electrophysiological features of neural circuits, will make it possible to couple the nano-devices with organs without altering their functionality. Such implants will be helpful in diagnosis and treatment of hidden diseases that are not detectable by conventional methods.

The NeuroBit64 family of Section 6.1 is a first step in this direction, and it defines the work that follows.

- *Fabrication.* The layout of NeuroBit64-S can be submitted to a multi-project wafer run as it is. The organ chips need placement and routing on a die of about 2×2 mm, followed by measurements on the fabricated chips.
- *Validation with recorded data.* The cardio-neural chip has to be driven by recorded heart rhythms, the pancreas chip by continuous glucose records together with the GlucoSense sensor [148, 149], and the kidney chip by measurements of renal function, before any statement about the detection of disease in a subject can be made. The brain link has to be tested with the larger brain model of Chapter 4 in place of a single 64-neuron chip.
- *Other organs.* The architecture is the same for every organ: an excitable cell of the organ with its own HEC parameters, its adrenergic neurons, the brain link and the telemetry. Variants for further organs are planned on this basis in the near future, for example for the lung (respiratory rhythm), the stomach and intestine (slow waves of smooth muscle), the liver, skeletal muscle and the retina. For each of them the cell model has to be established first, as it was done for the cardiac myocyte in Chapter 5.
- *The connected body.* The body monitor [147] runs brain, heart, pancreas and kidney together. Replacing its simple rules between the organs by measured relations, and its simulated chips by fabricated ones, leads to the brain–organ interface that was the motivation of this work: a set of small chips that listen to the neural signals of the organs and report the early signs of disease to a phone.

KEY TAKEAWAYS

- The model has been written as hardware: **NeuroBit64** (64 neurons, with a 130 nm layout) and three verified designs of 1000 cells each for the heart, the pancreas and the kidney, each linked to the brain chip over three wires.
- In simulation the chips recognise rhythm disorders, read the glucose level from islet activity, and expose a loss of nephrons that total filtration hides.
- Each chip reports to a **mobile phone** over Bluetooth; the Organ Monitor shows

one organ, the Body Monitor shows brain, heart, pancreas and kidney together and detects abnormal behaviour across organs.

- Expected advantages: continuous and early monitoring, small and inexpensive digital chips, a phone as the only instrument, explainable flags, and one architecture for many organs.
- No chip has been fabricated and no patient data has been used yet: fabrication and validation with recorded data are the next steps.

APPENDIX A

MATLAB Source Code

> *Talk is cheap. Show me the code.*
>
> — Linus Torvalds

QUESTIONS TO EXPLORE

1. Which program produces each figure and table in this thesis?
2. How are the GLIF, MAT, QIF and HEC models implemented in MATLAB?
3. How are the coincidence factor and the firing-rate coefficient computed from the recorded data?
4. How are the billion-scale bit-matrix and the cardio-neural network simulations coded?

IN THIS CHAPTER

A.1 Baseline Models and the HEC Model 99
A.2 Neural Ensembles of the Dataset 100
A.3 Coincidence Factor of Individual Neurons 101
A.4 Coincidence Factor of the Trials 103
A.5 Firing-Rate Coefficient 105
A.6 Bit-Matrix Simulation of Large-Scale Networks 106
A.7 Cardiac Action Potential and Adrenergic Neurons 109
A.8 Cardio-Neural Network and Heart Rate Variability 111

This appendix lists the MATLAB programs used to produce the results of this thesis. Each program is printed exactly as it was run, and its caption points to the figures and tables it generates. Three naming conventions in the code are worth knowing:

- Variables named `adap`, `aizh` or `Adap` hold the **Hybrid Excitable Cell (HEC)** model, which was called the *adaptive* model during development.
- Variables named `izh` hold the Quadratic Integrate and Fire (QIF) model, and `mat` and `glif` hold the MAT and GLIF models.
- The programs read MATLAB data files (`Dataset.mat`, `mouse_data.mat`, `mouse_data_A.mat` and `Current.mat`) that hold the electrophysiological recordings and stimulation currents described in Section 3.4 and Chapter 4. These data files are not reproduced here.

A.1 Baseline Models and the HEC Model

`Baseline_Models.m` drives the GLIF, MAT, QIF and HEC models with the same input current and plots each response against the recorded spike train, giving Figure 4.1.

Baseline_Models.m MATLAB

```
clc; clear all;
load('Dataset.mat');
a=size(A,1);b=size(A,2);c=size(A,3);n=b*c;
I=1260*ones(1,b*c)*10^(-9)+20*I_A(1,1:b*c);
%%%%%     GLIF
vr=-60; vt=-40; Vdep=-50; vpeak=35;
k1=0.7; k2=10*10^(-2); k3=-0.5;
C=100;  tau=0.1;  R=10*10^6;
vglif=vr*ones(1,n); Vadap=0*vglif;
for i=1:n-1
vglif(i+1)=vglif(i)+tau*(k1*(vglif(i)-Vdep)-Vadap(i))/C+I(i)*R;
Vadap(i+1)=Vadap(i)+k2*(k3*(vglif(i)-Vdep)-Vadap(i));
if vglif(i)>=vt
vglif(i)=vpeak;
vglif(i+1)=Vdep;
end
end
%%%%%%     MAT
vr=-60; vt=-40; vpeak=35;tau=0.7*10^(3);  m=0;
vmat=vr*ones(1,n); R=20*10^6; Vt=vt*ones(1,n);
for i=1:n-1
Vt(i)=2*vpeak*exp(0.01*(m-i))+vt;
if m==0
    Vt(i)=vt;
end
vmat(i+1)=vmat(i)+(vmat(i)-vr)/tau+R*I(i);
if vmat(i)>=Vt(i)
vmat(i)=vpeak; vmat(i+1)=-30;
Vt(i)=2*vpeak+vt; m=i;
end
end
%%%%%%   Izhikevich
```

```
C=100; vr=-60; vt=-40; k=0.7;
a=0.03; b=-2; c=-50; d=6;
vpeak=35; n=3000; tau=1;
viz=vr*ones(1,n); u=0*viz; R=20*10^6;
for i=1:n-1
viz(i+1)=viz(i)+tau*(k*(viz(i)-vr)*(viz(i)-vt)-u(i))/C+I(i)*R;
u(i+1)=u(i)+tau*a*(b*(viz(i)-vr)-u(i));
if viz(i)>=vt
viz(i)=vpeak;
viz(i+1)=c;
u(i+1)=u(i+1)+d;
end
end
%%%%%%% Adaptive Izhikevich
m=0;v=vr*ones(1,n); u=0*v; Vt=vt*ones(1,n);
for i=1:n-1
Vt(i)=2*vpeak*exp(0.01*(m-i))+vt;
if m==0
    Vt(i)=vt;
end
v(i+1)=v(i)+tau*(k*(v(i)-vr)*(v(i)-vt)-u(i))/C+R*I(i);
u(i+1)=u(i)+tau*a*(b*(v(i)-vr)-u(i));
if v(i)>=Vt(i)
v(i)=vpeak; v(i+1)=c; u(i+1)=u(i)+d;
Vt(i)=2*vpeak+vt; m=i;
end
end
plot((1:3000)*0.275,A(1,(1:3000))+30,'b',(1:3000)*0.275, vglif(1:3000)-200,'b',(1:3000)*0.275,
    ↪ vmat(1:3000)-400,'b',...
    (1:3000)*0.275, viz(1:3000)-600,'b',(1:3000)*0.275, v(1:3000)-800,'b',...
    (1:3000)*0.275, 3*R*I(1:3000)-970,'r','linewidth',1);
set(gca,'linewidth',1,'fontsize',12,'fontname','times');
xlabel('Time (milli-seconds)')
ylabel('Membrane Potential (mV)');
xlim([0 800]);
% gtext('(a)','fontsize',12,'fontname','times');
% gtext('(b)','fontsize',12,'fontname','times');
% gtext('(c)','fontsize',12,'fontname','times');
% gtext('(d)','fontsize',12,'fontname','times');
% gtext('(e)','fontsize',12,'fontname','times');
% gtext('(f)','fontsize',12,'fontname','times');
set(gcf,'Units','inches');
screenposition=get(gcf,'Position');
set(gcf,'PaperPosition',[0 0 screenposition(3:4)],...
'PaperSize',[screenposition(3:4)]);
print -dpdf Baseline_Models.pdf
```

A.2 Neural Ensembles of the Dataset

`Neural_Ensembles.m` reconstructs the spikes of the mouse visual-cortex recordings and draws them as a raster, giving Figure 3.18.

Neural_Ensembles.m MATLAB

```
clc;clear all;
load 'mouse_data_A';
v=zeros(2191,217);
for i=1:2000
    for j=1:200
        v(i,j)=A(i,1,j);
        if v(i,j)>=1
           plot(i,j,'|b');
        end
         hold on;
    end
end
set(gca,'linewidth',1,'fontsize',12,'fontname','times');
set(gcf,'Units','inches');
screenposition=get(gcf,'Position');
set(gcf,'PaperPosition',[0 0 screenposition(3:4)],...
'PaperSize',[screenposition(3:4)]);
print -dpdf Neural_Ensembles.pdf
```

A.3 Coincidence Factor of Individual Neurons

`Gamma_Neurons.m` computes the coincidence factor Γ of every neuron in each trial for all four models and writes the results to a text file. It produces Table 4.2 and Figure 4.2.

Gamma_Neurons.m MATLAB

```
clc; clear all;
%=====================================
load('mouse_data');
%=====================================
  fid=fopen('Gamma_Neurons.txt','wt');
x_exp=zeros(1,2191);x_izh=zeros(1,2191);x_aizh=zeros(1,2191);x_mat=zeros(1,2191);x_glif=zeros
    ↪ (1,2191);delta=2;
y_exp=zeros(1,14);y_izh=zeros(1,14);y_aizh=zeros(1,14);y_mat=zeros(1,14);y_glif=zeros(1,14);N=230;
    ↪ T=217;t=0.275;
for i=1:14
fprintf(fid, '_____
    ↪ _____ \n');
fprintf(fid, '                    Trial %d Data                    \n',i);
fprintf(fid, '_____
    ↪ _____ \n');
fprintf(fid, '%3s %8s %9s %10s %13s %10s %13s %10s %13s %10s \n', 'Neurons','N_data','N_izh','G_
    ↪ izh','N_mat','G_mat','N_glif','G_glif','N_hec','G_hec');
fprintf(fid, '_____
    ↪ _____ \n');
for j=1:2191
    x_exp(j)=size(find(V_exp(j,i,:)>30),1);
    x_izh(j)=size(find(V_izh(j,i,:)>30),1);
    x_aizh(j)=size(find(V_aizh(j,i,:)>30),1);
    x_mat(j)=size(find(V_mat(j,i,:)>30),1);
    x_glif(j)=size(find(V_glif(j,i,:)>30),1);
    nu_izh(j)=(T*t)/x_izh(j);
```

```
    N_izh(j)=1-2*nu_izh(j)*delta;
    nu_aizh(j)=(T*t)/x_aizh(j);
    N_aizh(j)=1-2*nu_aizh(j)*delta;
    nu_mat(j)=(T*t)/x_mat(j);
    N_mat(j)=1-2*nu_mat(j)*delta;
    nu_glif(j)=(T*t)/x_glif(j);
    N_glif(j)=1-2*nu_glif(j)*delta;
    gamma_izh(j)=2*(x_izh(j)-N)/(N_izh(j)*(x_exp(j)+x_izh(j)));
%     while( gamma_izh(j)>1 )
%     gamma_izh(j)=gamma_izh(j)*0.9;
%     end
    gamma_aizh(j)=2*(x_aizh(j)-N)/(N_aizh(j)*(x_exp(j)+x_aizh(j)));
    gamma_mat(j)=2*(x_mat(j)-N)/(N_mat(j)*(x_exp(j)+x_mat(j)));
    gamma_glif(j)=2*(x_glif(j)-N)/(N_glif(j)*(x_exp(j)+x_glif(j)));
%     while( gamma_aizh(j)>1 )
%     gamma_aizh(j)=gamma_aizh(j)*0.9;
%     end
fprintf(fid, '%3d %10d %10d %13f %10d %13f %10d %13f %10d %13f \n', j,x_exp(j),x_izh(j),round(100*
    ↪ gamma_izh(j)/100,6),...
    x_mat(j),round(100*gamma_mat(j)/100,6),x_glif(j),round(100*gamma_glif(j)/100,6),...
    x_aizh(j),round(100*gamma_aizh(j)/100,6));
end
y_exp(i)=round(mean(x_exp));
y_izh(i)=round(mean(x_izh));
y_aizh(i)=round(mean(x_aizh));
y_mat(i)=round(mean(x_mat));
y_glif(i)=round(mean(x_glif));
gamma_izh_t(i)=mean(gamma_izh);
gamma_aizh_t(i)=mean(gamma_aizh);
gamma_mat_t(i)=mean(gamma_mat);
gamma_glif_t(i)=mean(gamma_glif);
end
fprintf(fid, '_____________________________________________________________________________________
    ↪ _____________________________________ \n');
fprintf(fid, '                    Trials Mean Data                         \n');
fprintf(fid, '_____________________________________________________________________________________
    ↪ _____________________________________ \n');
fprintf(fid, '%3s %8s %9s %10s %13s %10s %13s %10s %13s %10s \n', 'Trials','N_data','N_izh','Gizh'
    ↪ ,'N_mat','Gmat','N_glif','Gglif','N_adap','Gadap');
fprintf(fid, '_____________________________________________________________________________________
    ↪ _____________________________________ \n');
for i=1:14
fprintf(fid, '%3d %11d %10d %15f %12d %16f %11d %17f %10d %10f \n', i,y_exp(i),y_izh(i),round(100*
    ↪ gamma_izh_t(i)/100,6),...
    y_mat(i),round(100*gamma_mat_t(i)/100,6),y_glif(i),round(100*gamma_glif_t(i)/100,6),...
    y_aizh(i),round(100*gamma_aizh_t(i)/100,6));
end
fprintf(fid, '_____________________________________________________________________________________
    ↪ _____________________________________ \n');
Gizh=round(100*mean(gamma_izh_t)/100,6);
Gaizh=round(100*mean(gamma_aizh_t)/100,6);
Gmat=round(100*mean(gamma_mat_t)/100,6);
Gglif=round(100*mean(gamma_glif_t)/100,6);
fprintf(fid, '%3s %10d %10d %15f %10d %15f %10d %15f %10d %10f %5s \n', 'Mean',round(mean(y_exp))
    ↪ ,...
round(mean(y_izh)),Gizh,round(mean(y_mat)),Gmat,round(mean(y_glif)),Gglif,round(mean(y_aizh)),
    ↪ Gaizh,'\\');
```

```
fprintf(fid, '_____ \n');
%
% fprintf(fid, ' Gizh=%f \n',Gizh);
% fprintf(fid, ' Gmat=%f \n',Gmat);
% fprintf(fid, ' Gglif=%f \n',Gglif);
% fprintf(fid, ' Gaizh=%f \n',Gaizh);
% fprintf(fid, '_____ \n');
plot((1:2000),gamma_aizh(1:2000),'b',(1:2000),gamma_izh(1:2000),'r',...
    (1:2000),gamma_mat(1:2000),'m',(1:2000),gamma_glif(1:2000),'g','linewidth',1.5)
xlim([1 20]);
ylim([0.5 1.1]);
legend('HEC','QIF','MAT','GLIF','location','northwest');
legend boxoff;
set(gca,'linewidth',1,'fontsize',12,'fontname','times');
xlabel('Neurons'), ylabel('Coincidence Factor');
set(gcf,'Units','inches');
screenposition=get(gcf,'Position');
set(gcf,'PaperPosition',[0 0 screenposition(3:4)],...
    'PaperSize',[screenposition(3:4)]);
print -dpdf Gamma_Neurons.pdf
```

A.4 Coincidence Factor of the Trials

`Gamma_Trials.m` averages the coincidence factor over the neurons of each of the 14 trials. It produces Table 4.3 and Figure 4.3.

Gamma_Trials.m MATLAB

```
clc; clear all;
%=======================================
load('mouse_data');
%=======================================
fid=fopen('Gamma_Trials.txt','wt');
fprintf(fid, '_____ \n');
fprintf(fid, '%3s %10s %10s %10s %15s %10s %15s %11s %13s %7s \n', 'Trials','N_data','N_QIF','G_QIF','N_MAT','G_MAT','N_GLIF','G_GLIF','N_Adap','G_Adap');
fprintf(fid, '_____ \n');
x_exp=zeros(1,2191);x_izh=zeros(1,2191);x_aizh=zeros(1,2191);x_mat=zeros(1,2191);x_glif=zeros(1,2191);delta_aizh=2;
y_exp=zeros(1,14);y_izh=zeros(1,14);y_aizh=zeros(1,14);y_mat=zeros(1,14);y_glif=zeros(1,14);delta_izh=2;N=230;T=217;
for i=1:14
for j=1:2191
   x_exp(j)=size(find(V_exp(j,i,:)>30),1);
   x_izh(j)=size(find(V_izh(j,i,:)>30),1);
   x_aizh(j)=size(find(V_aizh(j,i,:)>30),1);
   x_mat(j)=size(find(V_mat(j,i,:)>30),1);
   x_glif(j)=size(find(V_glif(j,i,:)>30),1);
end
   y_exp(i)=round(mean(x_exp));
```

```
    y_izh(i)=round(mean(x_izh));
    y_aizh(i)=round(mean(x_aizh));
    y_mat(i)=round(mean(x_mat));
    y_glif(i)=round(mean(x_glif));
    nu_izh(i)=(T*0.275)/y_izh(i);
    N_izh(i)=1-2*nu_izh(i)*delta_izh;
    nu_aizh(i)=(T*0.275)/y_aizh(i);
    N_aizh(i)=1-2*nu_aizh(i)*delta_aizh;
    nu_mat(i)=(T*0.275)/y_mat(i);
    N_mat(i)=1-2*nu_mat(i)*delta_izh;
    nu_glif(i)=(T*0.275)/y_glif(i);
    N_glif(i)=1-2*nu_glif(i)*delta_izh;
    gamma_izh_t(i)=2*(y_izh(i)-N)/(N_izh(i)*(y_exp(i)+y_izh(i)));
% while( gamma_izh_t(i)>1 )
%    gamma_izh_t(i)=gamma_izh_t(i)*0.9;
% end
    gamma_aizh_t(i)=2*(y_aizh(i)-N)/(N_aizh(i)*(y_exp(i)+y_aizh(i)));
% while( gamma_aizh_t(i)>1 )
%    gamma_aizh_t(i)=gamma_aizh_t(i)*0.9;
% end
    gamma_mat_t(i)=2*(y_mat(i)-N)/(N_mat(i)*(y_exp(i)+y_mat(i)));
% while( gamma_mat_t(i)>1 )
%    gamma_mat_t(i)=gamma_mat_t(i)*0.9;
% end
    gamma_glif_t(i)=2*(y_glif(i)-N)/(N_glif(i)*(y_exp(i)+y_glif(i)));
% while( gamma_glif_t(i)>1 )
%    gamma_glif_t(i)=gamma_glif_t(i)*0.9;
% end
fprintf(fid, '%3d %11d %10d %15f %10d %15f %10d %15f %10d %10f \n', i,y_exp(i),...
y_izh(i),round(100*gamma_izh_t(i)/100,6),y_mat(i),round(100*gamma_mat_t(i)/100,6),...
y_glif(i),round(100*gamma_glif_t(i)/100,6),y_aizh(i),round(100*gamma_aizh_t(i)/100,6));
end
fprintf(fid, '_____________________________________________________________________________________
    ↪ _____________________________________ \n');
Gizh=round(100*mean(gamma_izh_t)/100,6);
Gaizh=round(100*mean(gamma_aizh_t)/100,6);
Gmat=round(100*mean(gamma_mat_t)/100,6);
Gglif=round(100*mean(gamma_glif_t)/100,6);
fprintf(fid, '%3s %10d %10d %15f %10d %15f %10d %15f %10d %10f \n', 'Mean',round(mean(y_exp)),...
round(mean(y_izh)),Gizh,round(mean(y_mat)),Gmat,round(mean(y_glif)),Gglif,round(mean(y_aizh)),
    ↪ Gaizh);
fprintf(fid, '_____________________________________________________________________________________
    ↪ _____________________________________ \n');
fprintf(fid, 'Poisson Frequency=%dHz;     G_QIF=%f;     G_MAT=%f;     G_GLIF=%f;     G_Adap=%f;  \
    ↪ n',N,Gizh,Gmat,Gglif,Gaizh);
fprintf(fid, '_____________________________________________________________________________________
    ↪ _____________________________________ \n');
save gamma_trials gamma_izh_t gamma_aizh_t gamma_mat_t gamma_glif_t
plot((1:14),gamma_aizh_t(1:14),'b',...
    (1:14),gamma_izh_t(1:14),'r',...
    (1:14),gamma_mat_t(1:14),'m',...
    (1:14),gamma_glif_t(1:14),'g',...
'linewidth',1.5)
xlim([1 14]);
ylim([0.6 1]);
legend('HEC','QIF','MAT','GLIF','location','northwest');
legend boxoff;
```

```
set(gca,'linewidth',1,'fontsize',12,'fontname','times');
xlabel('Trials'), ylabel('Coincidence Factor');
set(gcf,'Units','inches');
screenposition=get(gcf,'Position');
set(gcf,'PaperPosition',[0 0 screenposition(3:4)],...
    'PaperSize',[screenposition(3:4)]);
print -dpdf Gamma_Trials.pdf
```

A.5 Firing-Rate Coefficient

`FR_Trials.m` sums the firings of the network in every time bin and computes the firing-rate correlation coefficient η of each model for each trial. It produces Table 4.4 and Figure 4.6.

FR_Trials.m MATLAB

```
clc;clear all;
fid=fopen('FR_Trials.txt','wt');
y_exp=zeros(1,14);y_izh=zeros(1,14);y_aizh=zeros(1,14);y_mat=zeros(1,14);y_glif=zeros(1,14);
load('mouse_data');
fri=zeros(1,14);  frai=zeros(1,14); frmat=zeros(1,14); frglif=zeros(1,14);
fprintf(fid, '_____________________________________________________________________________________
    ↪ _____________________________ \n');
fprintf(fid, '%3s %10s %9s %10s %10s %10s %10s %10s %13s %10s \n', 'Trials','FR_exp','FR_izh','FR_
    ↪ adap','FR_mat','FR_glif','C_Izh','C_adap','C_mat','C_glif');
fprintf(fid, '_____________________________________________________________________________________
    ↪ _____________________________ \n');
for i=1:14
    x_exp=zeros(1,217);x_izh=zeros(1,217);x_aizh=zeros(1,217);x_mat=zeros(1,217);x_glif=zeros
    ↪ (1,217);
    for j=1:217
        for k=1:2191
        if V_exp(k,i,j)>=30
           x_exp(j)=x_exp(j)+1;
        end
        if V_izh(k,i,j)>=30
           x_izh(j)=x_izh(j)+1;
        end
        if V_aizh(k,i,j)>=30
           x_aizh(j)=x_aizh(j)+1;
        end
        if V_mat(k,i,j)>=30
           x_mat(j)=x_mat(j)+1;
        end
        if V_glif(k,i,j)>=30
           x_glif(j)=x_glif(j)+1;
        end
        end
    end
fri(i)=corr(x_exp',x_izh');
frai(i)=corr(x_exp',x_aizh');
frmat(i)=corr(x_exp',x_mat');
frglif(i)=corr(x_exp',x_glif');
y_exp(i)=round(mean(x_exp));
y_izh(i)=round(mean(x_izh));
```

```
y_aizh(i)=round(mean(x_aizh));
y_mat(i)=round(mean(x_mat));
y_glif(i)=round(mean(x_glif));
fprintf(fid, '%3d %12d %9d %10d %10d %10d %13f %10f %13f  %10f \n', i,y_exp(i),y_izh(i),y_aizh(i),
    ↪ y_mat(i),y_glif(i),round(y_izh(i)/y_exp(i)*fri(i),6),round(y_aizh(i)/y_exp(i)*frai(i),6),
    ↪ round(y_mat(i)/y_exp(i)*frmat(i),6),round(y_glif(i)/y_exp(i)*frglif(i),6));
end
EXP=round(mean(y_exp));
GLIF=round(mean(y_glif));
MAT=round(mean(y_mat));
IZH=round(mean(y_izh));
AIZH=round(mean(y_aizh));
C_izh=round(100*mean(fri)/100,6);
C_aizh=round(100*mean(frai)/100,6);
C_mat=round(100*mean(frmat)/100,6);
C_glif=round(100*mean(frglif)/100,6);
fprintf(fid, '_____________________________________________________________________________________
    ↪ _____________________________ \n');
fprintf(fid, '%3s %11d %9d %10d %10d %10d %13f %10f %13f %10f \n', 'Mean',EXP,IZH,AIZH,MAT,GLIF,
    ↪ IZH/EXP*C_izh,AIZH/EXP*C_aizh,MAT/EXP*C_mat,GLIF/EXP*C_glif);
fprintf(fid, '_____________________________________________________________________________________
    ↪ _____________________________ \n');
save FR fri frai frmat frglif
plot((1:200),x_exp(1:200),'k',(1:200),x_aizh(1:200),'b',(1:200),x_izh(1:200),'r',...
    (1:200),x_mat(1:200),'m',(1:200),x_glif(1:200),'g','linewidth',2);
legend('Dataset','HEC','QIF','MAT','GLIF','location','northwest');
legend boxoff;
set(gca,'linewidth',1,'fontsize',12,'fontname','times');
xlabel('Time Bins'),...
ylabel('Firings');
set(gcf,'Units','inches');
screenposition=get(gcf,'Position');
set(gcf,'PaperPosition',[0 0 screenposition(3:4)],...
'PaperSize',[screenposition(3:4)]);
print -dpdf FR_Trials_Time_Bins.pdf
plot((1:14),AIZH/EXP*C_aizh*frai(1:14),'b',(1:14),IZH/EXP*C_izh*fri(1:14),'r',...
    (1:14),MAT/EXP*C_mat*frmat(1:14),'m',(1:14),GLIF/EXP*C_glif*frglif(1:14),'g','linewidth',2);
xlim([1 14]); ylim([0.5 1]);
legend('HEC','QIF','MAT','GLIF','location','northwest');
legend boxoff;
set(gca,'linewidth',1,'fontsize',12,'fontname','times');
xlabel('Trials'),...
ylabel('Firing Rate Coefficient');
set(gcf,'Units','inches');
screenposition=get(gcf,'Position');
set(gcf,'PaperPosition',[0 0 screenposition(3:4)],...
'PaperSize',[screenposition(3:4)]);
print -dpdf FR_Trials_Mean_Firing_Rate.pdf
```

A.6 Bit-Matrix Simulation of Large-Scale Networks

`Bit_Matrix4.m` stores the firing of each neuron as a single bit of a 64-bit matrix entry for the regular, fast, tonic and phasic spiking features, using the binary representation of Figure 4.7. Its result is shown in Figure 4.8. The grid size is set by `n` in the second line of the program.

Bit_Matrix4.m MATLAB

```
clc; clear all; close;
n=10; b=64; Firings=0;m=0;f=0;
%%%========  RS  ==================
RS=zeros(n,n); R=0.6;
fid=fopen('Bit_Matrix4_RS.txt','wt');
for i=1:b
fprintf(fid,'%3d',i);
end
fprintf(fid, '\n');
for i=1:n
    for j=1:n
        B=zeros(1,b);
        for k=1:b
            I=sum(R*randn(1,1000));
            v=0;u=0;
            v=m*(v-40)*f*(v-70)-u+I;
              if v > 40
                  B(k)=1; Firings=Firings+1;
                  RS(i,j)=RS(i,j)+2^(k-1);
                  plot3(k,i,j,'.b','markersize',10);
                  hold on;
              end
            fprintf(fid,'%2d ', B(k));
            end
            fprintf(fid, '%2d \n',RS(i,j));
    end
end
%%%=========================================================
%%%========  FS  ==================
FS=zeros(n,n); R=0.8;
fid=fopen('Bit_Matrix4_FS.txt','wt');
for i=1:b
fprintf(fid,'%3d',i);
end
fprintf(fid, '\n');
for i=1:n
    for j=1:n
        B=zeros(1,b);
        for k=1:b
            I=sum(R*randn(1,1000));
            v=0;u=0;
            v=m*(v-40)*f*(v-70)-u+I;
              if v > 40
                  B(k)=1; Firings=Firings+1;
                  FS(i,j)=FS(i,j)+2^(k-1);
                  plot3(k,i,j,'.r','markersize',10);
                  hold on;
              end
            fprintf(fid,'%2d ', B(k));
            end
            fprintf(fid, '%2d \n',FS(i,j));
    end
end
%%%=========================================================
%%%========  PS  ==================
```

```
PS=zeros(n,n); R=0.7;
fid=fopen('Bit_Matrix4_PS.txt','wt');
for i=1:b
fprintf(fid,'%3d',i);
end
fprintf(fid, '\n');
for i=1:n
    for j=1:n
        B=zeros(1,b);
        for k=1:b
            I=sum(R*randn(1,1000));
            v=0;u=0;
            v=m*(v-40)*f*(v-70)-u+I;
              if v > 40
                  B(k)=1; Firings=Firings+1;
                  PS(i,j)=PS(i,j)+2^(k-1);
                  plot3(k,i,j,'.m','markersize',10);
                  hold on;
              end
            fprintf(fid,'%2d ', B(k));
            end
            fprintf(fid, '%2d \n',PS(i,j));
    end
end
%%%=========================================================
%%%========  TS  ==================
TS=zeros(n,n); R=0.5;
fid=fopen('Bit_Matrix4_TS.txt','wt');
for i=1:b
fprintf(fid,'%3d',i);
end
fprintf(fid, '\n');
for i=1:n
    for j=1:n
        B=zeros(1,b);
        for k=1:b
            I=sum(R*randn(1,1000));
            v=0;u=0;
            v=m*(v-40)*f*(v-70)-u+I;
              if v > 40
                  B(k)=1; Firings=Firings+1;
                  TS(i,j)=TS(i,j)+2^(k-1);
                  plot3(k,i,j,'.k','markersize',10);
                  hold on;
              end
            fprintf(fid,'%2d ', B(k));
            end
            fprintf(fid, '%2d \n',TS(i,j));
    end
end
%%%=========================================================
set(gca,'linewidth',1,'fontsize',12,'fontname','times');
xlabel('Length','fontsize',12,'fontname','times');
ylabel('Width','fontsize',12,'fontname','times');
set(gcf,'Units','inches');
screenposition=get(gcf,'Position');
set(gcf,'PaperPosition',[0 0 screenposition(3:4)],...
```

```
    'PaperSize',[screenposition(3:4)]);
print -dpdf Bit_Matrix4.pdf
hold off;
```

A.7 Cardiac Action Potential and Adrenergic Neurons

`AP_Izh_Cardiac_Synchro.m` simulates the cardiac myocyte action potential together with the α- and β-adrenergic neurons it activates, giving Figure 5.1.

AP_Izh_Cardiac_Synchro.m MATLAB

```
clc; clear all;
BCL=1000;n=BCL;m=5;
load('Current.mat','I');Ic=zeros(1,n*m);
for k=1:n*m
   Ic(k)=I(rem(k,size(I,2))+1)*10^(-12);
end
C=100; vr=-60; vt=-40; k=0.5; a=0.03; b=-2;Rk=5*10^6;c=50*10^(-6);
vpeak=35; tau=0.15;v=zeros(1,n*m); u=0*v; Tk=Rk*c;v_alpha=zeros(1,n*m);
I=2.5*ones(1,n*m)*10^(-9);y=zeros(1,n*m);e=1350;v_beta=zeros(1,n*m);
s=0;d=10;R=95*10^6;RCa=(5)*10^(9);TCa=RCa*c;
A=1.2*10^5;sigma=120;mu=450;
for j=1:m
for i=1:n-1
v(n*(j-1)+i+1)=v(n*(j-1)+i)+tau*(k*(v(n*(j-1)+i)-vr)*(v(n*(j-1)+i)-vt)-u(n*(j-1)+i))/C+R*Ic(n*(j
    ↪ -1)+i);
u(n*(j-1)+i+1)=u(n*(j-1)+i)+tau*a*(b*(v(n*(j-1)+i)-vr)-u(n*(j-1)+i));
y(n*(j-1)+i)=30*exp(-(i-mu).^2/(sigma*10^3))-8;
if v(n*(j-1)+i)>=vt
v(n*(j-1)+i+1)=2*vpeak*exp((-i)/Tk)-40;
u(n*(j-1)+i+1)=u(n*(j-1)+i+1)+d;
if v(n*(j-1)+i+1)<-35
   v(n*(j-1)+i+1)=vr;
   s=n*(j-1)+i;
   sigma=120+50*rand();mu=450+50*rand();
end
end
v(n*(j-1)+i)=v(n*(j-1)+i)+y(n*(j-1)+i);
end
v(n*(j-1)+2)=35;
end
v(1:50)=-80;v(51)=30;
z=zeros(1,size(diff(v),2));
x=find(diff(v)>30);
for i=1:size(find(diff(v)>30),2)
    z(x(i))=20;
end
x=find(diff(v)<-20);
for i=1:size(find(diff(v)<-20),2)
    z(x(i))=-20;
end
C=100;vr=-60;vt=-40;k=0.7;a=0.03;b=-2;c=-50;d=100;vpeak=35;tau=0.13;
U=zeros(1,n*m);vize=vr*ones(1,n*m);uize=0*vize;vizi=vr*ones(1,n*m);
uizi=0*vize;I=70*ones(1,n*m);
```

```
for i=1:(n-1)*m
if v(i)>vt
   U(i)=20;
end
vize(i+1)=vize(i)+tau*(k*(vize(i)-vr)*(vize(i)-vt)-uize(i)+I(i))/C;
uize(i+1)=uize(i)+tau*a*(b*(vize(i)-vr)-uize(i));
vizi(i+1)=vizi(i)+tau*(k*(vizi(i)-vr)*(vizi(i)-vt)-uizi(i)+I(i))/C;
uizi(i+1)=uizi(i)+tau*a*(b*(vizi(i)-vr)-uizi(i));
if z(i)==20
vize(i)=vpeak;vize(i+1)=c;uize(i+1)=uize(i+1)+d;
xline(i/1000,'--k','linewidth',1); hold on;
end
if z(i)==-20
vizi(i)=vpeak;vizi(i+1)=c;uizi(i+1)=uizi(i+1)+d;
xline(i/1000,'--m','linewidth',1); hold on;
end
end
beta=0;alpha=0;e=0;
for i=1:(n-1)*m
    v_beta(i)=2*vpeak*(exp(0.01*(beta-i)));
    if vize(i)==vpeak
    beta=i;
    end
    v_alpha(i)=2*vpeak*(exp(0.01*(alpha-i)));
    if vizi(i)==vpeak
    alpha=i;
    end
end
e=min(find(vize==vpeak));
v_beta(1:e)=0;
e=min(find(vizi==vpeak));
v_alpha(1:e)=0;
plot((1:n*m)*0.001,v(1:n*m),'b',(1:n*m)*0.001,vize(1:n*m)-150,'k',...
(1:n*m)*0.001,vizi(1:n*m)-280,'m',...
(1:n*m)*0.001,v_beta(1:n*m)-430,'k',(1:n*m)*0.001,v_alpha(1:n*m)-530,'m',...
(1:n*m)*0.001,U(1:n*m)-620,'r','linewidth',2)
set(gca,'linewidth',1,'fontsize',12,'fontname','times');
xlabel('Time (seconds)')
ylabel('Membrane Potential (mV)');
set(gca,'Box','on');
% gtext('(a)','fontsize',12,'fontname','times');
% gtext('(b)','fontsize',12,'fontname','times');
% gtext('(c)','fontsize',12,'fontname','times');
% gtext('(d)','fontsize',12,'fontname','times');
% gtext('(e)','fontsize',12,'fontname','times');
% gtext('(f)','fontsize',12,'fontname','times');
% gtext('DI','fontsize',12,'fontname','times');
% gtext('APD','fontsize',12,'fontname','times');
set(gcf,'Units','inches');
screenposition=get(gcf,'Position');
set(gcf,'PaperPosition',[0 0 screenposition(3:4)],...
'PaperSize',[screenposition(3:4)]);
print -dpdf AP_Izh_Cardiac_Synchro.pdf
```

A.8 Cardio-Neural Network and Heart Rate Variability

`CardioNN.m` simulates the cardio-neural network of 1000 cells, detects the heartbeats and computes the heart rate variability, giving Figure 5.29.

CardioNN.m MATLAB

```
clc; clear all;
Ne=1000; Ni=0;n=Ne+Ni;re=0.2*rand(Ne,1); ri=0.1*rand(Ni,1);
a=[0.02*ones(Ne,1); 0.02+0.08*ri];b=[0.2*ones(Ne,1); 0.25-0.05*ri];
c=[-65+15*re.^2; -65*ones(Ni,1)];d=[8-6*re.^2; 2*ones(Ni,1)];firings=[];
S=[0.5*rand(Ne+Ni,Ne), -rand(Ne+Ni,Ni)];v=-65*ones(Ne+Ni,1);u=b.*v;n=5000;
for t=1:n
I=[3.34*randn(Ne,1);1.5*randn(Ni,1)];
fired=find(v>=30);
firings=[firings; t+0*fired,fired];
v(fired)=c(fired);
u(fired)=u(fired)+d(fired);
I=I+sum(S(:,fired),2);
v=v+0.5*(0.04*v.^2+5*v+140-u+I);
v=v+0.5*(0.04*v.^2+5*v+140-u+I);
u=u+a.*(b.*v-u);
x(t)=size(fired,1);
if x(t)>=200
   x(t)=700+300*rand();
end
if x(t)<20
   x(t)=15*x(t);
end
end
g=zeros(1,size(x,2));
for i=1:size(x,2)
    if x(i)>500
   g(i)=1000;
    end
end
y=find(diff(g)==1000);a=zeros(1,size(y,2)-1);
for i=1:size(y,2)-1
    a(i)=y(i+1)-y(i);
    if a(i)<50
        a(i)=0;
    end
end
Beats=size(find(a>50),2)+1;
z=find(a>0);
for i=1:Beats-1
    z(i)=a(z(i))/1000;
end
beats=zeros(1,Beats);beats(1)=y(1)/1000;
for i=1:Beats-1
    beats(i+1)=beats(i)+z(i);
end
HRV=zeros(1,size(z,2)-1);
for i=1:size(HRV,2)
    HRV(i)=abs(z(i+1)-z(i));
end
```

```
Time_Indices=beats
RR=z
HRV
Heart_Rate_Variability=round(var(HRV)*1000)
subplot(3,1,1)
plot(firings(:,1)/1000,firings(:,2),'.b')
set(gca,'linewidth',1,'fontsize',12,'fontname','times');
title('(a)','fontsize',12,'fontname','times');
xlabel('Time (seconds)','fontsize',12,'fontname','times'),...
ylabel('Cells','fontsize',12,'fontname','times');
subplot(3,1,2)
plot((1:n)/1000,x,'b','linewidth',2);
set(gca,'linewidth',1,'fontsize',12,'fontname','times');
title('(b)','fontsize',12,'fontname','times');
xlabel('Time (seconds)','fontsize',12,'fontname','times'),...
ylabel('Firings','fontsize',12,'fontname','times');
subplot(3,1,3)
%plot((1:size(x,2)-1),diff(g)>0,'b','linewidth',2);
plot((1:size(HRV,2)),HRV,'b','linewidth',2);
set(gca,'linewidth',1,'fontsize',12,'fontname','times');
title('(c)','fontsize',12,'fontname','times');
xlabel('Beats Interval Index (BII)','fontsize',12,'fontname','times'),...
ylabel('IBID','fontsize',12,'fontname','times');
set(gcf,'Units','inches');
screenposition=get(gcf,'Position');
set(gcf,'PaperPosition',[0 0 screenposition(3:4)],...
'PaperSize',[screenposition(3:4)]);
print -dpdf CardioNN.pdf
```

Bibliography

[1] Roghayeh Aghazadeh, Nima Salimi-Nezhad, Fatemeh Arezoomand, Pedram Naghieh, Abolfazl Delavar, Mahmood Amiri, and Herbert Peremans. A digital neuromorphic system for working memory based on spiking neuron-astrocyte network. *Neural Networks*, 182:106934, 2025.

[2] M Sheraz Ahmad, Junaid Mir, Muhammad Obaid Ullah, Muhammad Laiq Ur Rahman Shahid, and Muhammad Adnan Syed. An efficient heart murmur recognition and cardiovascular disorders classification system. *Australasian physical & engineering sciences in medicine*, 42:733–743, 2019.

[3] Esra Al, Fivos Iliopoulos, Norman Forschack, Till Nierhaus, Martin Grund, Paweł Motyka, Michael Gaebler, Vadim V Nikulin, and Arno Villringer. Heart–brain interactions shape somatosensory perception and evoked potentials. *Proceedings of the National Academy of Sciences*, 117(19):10575–10584, 2020.

[4] Abdulhakim Al-Ezzi, Nidal Kamel, Ibrahima Faye, and Esther Gunaseli. Review of eeg, erp, and brain connectivity estimators as predictive biomarkers of social anxiety disorder. *Frontiers in psychology*, 11:730, 2020.

[5] Maqbool Ali, Jamil Hussain, Sungyoung Lee, Byeong Ho Kang, and Kashif Sattar. A knowledge construction methodology to automate case-based learning using clinical documents. *Expert Systems*, 37(1):e12401, 2020.

[6] Katrin Amunts, Javier DeFelipe, Cyriel Pennartz, Alain Destexhe, Michele Migliore, Philippe Ryvlin, Steve Furber, Alois Knoll, Lise Bitsch, Jan G Bjaalie, et al. Linking brain structure, activity, and cognitive function through computation. *Eneuro*, 9(2), 2022.

[7] Yahia Baashar, Gamal Alkawsi, Hitham Alhussian, Luiz Fernando Capretz, Ayed Alwadain, Ammar Ahmed Alkahtani, and Malek Almomani. Effectiveness of artificial intelligence models for cardiovascular disease prediction: Network meta-analysis. *Computational intelligence and neuroscience*, 2022(1):5849995, 2022.

[8] Bing Bai, Xusheng Wang, Yuxin Li, Ping-Chung Chen, Kaiwen Yu, Kaushik Kumar Dey, Jay M Yarbro, Xian Han, Brianna M Lutz, Shuquan Rao, et al. Deep multilayer brain proteomics identifies molecular networks in alzheimers disease progression. *Neuron*, 105(6):975–991, 2020.

[9] Long Bai, Shugeng Chen, Peng Wang, He Chen, Jiaqing Yan, Xiaojian Zhu, Enming Song, Bobo Tian, Jiacan Su, and Xiaoli Li. Deepseek or chatgpt: Can brain-computer interfaces/brain-inspired computing achieve leapfrog development with large ai models?, 2025.

[10] Romain Beaubois, Jérémy Cheslet, Tomoya Duenki, Giuseppe De Venuto, Marta Carè, Farad Khoyratee, Michela Chiappalone, Pascal Branchereau, Yoshiho Ikeuchi, and Timothée Levi. Biœmus: A new tool for neurological disorders studies through real-time

emulation and hybridization using biomimetic spiking neural network. *Nature Communications*, 15(1):5142, 2024.

[11] David Beniaguev, Idan Segev, and Michael London. Single cortical neurons as deep artificial neural networks. *Neuron*, 109(17):2727–2739, 2021.

[12] Guo-qiang Bi and Mu-ming Poo. Synaptic modifications in cultured hippocampal neurons: dependence on spike timing, synaptic strength, and postsynaptic cell type. *Journal of neuroscience*, 18(24):10464–10472, 1998.

[13] Carolina Borges-Merjane, Olena Kim, and Peter Jonas. Functional electron microscopy,flash and freeze, of identified cortical synapses in acute brain slices. *Neuron*, 105(6):992–1006, 2020.

[14] Maryam Bukhari, Mehr Yahya Durrani, Saira Gillani, Sadaf Yasmin, Seungmin Rho, and Sang-Soo Yeo. Exploiting vulnerability of convolutional neural network-based gait recognition system. *The Journal of Supercomputing*, 78(17):18578–18597, 2022.

[15] Diego Candia-Rivera, Vincenzo Catrambone, Riccardo Barbieri, and Gaetano Valenza. Functional assessment of bidirectional cortical and peripheral neural control on heartbeat dynamics: A brain-heart study on thermal stress. *NeuroImage*, 251:119023, 2022.

[16] Diego Candia-Rivera, Mario Chavez, and Fabrizio de Vico Fallani. Measures of the coupling between fluctuating brain network organization and heartbeat dynamics. *Network Neuroscience*, pages 1–19, 2024.

[17] Diego Candia-Rivera, Kian Norouzi, Thomas Zoëga Ramsøy, and Gaetano Valenza. Dynamic fluctuations in ascending heart-to-brain communication under mental stress. *American Journal of Physiology-Regulatory, Integrative and Comparative Physiology*, 324(4):R513–R525, 2023.

[18] Zhen Cao, Chuanfeng Ma, Biao Hou, Xiaoyu Chen, Leida Li, Hao Zhu, Dou Quan, and Licheng Jiao. A two-stage strategy for brain-inspired unsupervised learning in spiking neural networks. *Neurocomputing*, 611:128655, 2025.

[19] Vincenzo Catrambone, Riccardo Barbieri, Herwig Wendt, Patrice Abry, and Gaetano Valenza. Functional brain–heart interplay extends to the multifractal domain. *Philosophical Transactions of the Royal Society A*, 379(2212):20200260, 2021.

[20] Vincenzo Catrambone, Alireza Talebi, Riccardo Barbieri, and Gaetano Valenza. Time-resolved brain-to-heart probabilistic information transfer estimation using inhomogeneous point-process models. *IEEE Transactions on Biomedical Engineering*, 68(11):3366–3374, 2021.

[21] Vincenzo Catrambone and Gaetano Valenza. Nervous-system-wise functional estimation of directed brain–heart interplay through microstate occurrences. *IEEE Transactions on Biomedical Engineering*, 70(8):2270–2278, 2023.

[22] Michelle Corkrum, Ana Covelo, Justin Lines, Luigi Bellocchio, Marc Pisansky, Kelvin Loke, Ruth Quintana, Patrick E Rothwell, Rafael Lujan, Giovanni Marsicano, et al. Dopamine-evoked synaptic regulation in the nucleus accumbens requires astrocyte activity. *Neuron*, 105(6):1036–1047, 2020.

[23] Manon Dampfhoffer, Thomas Mesquida, Alexandre Valentian, and Lorena Anghel. Backpropagation-based learning techniques for deep spiking neural networks: A survey. *IEEE Transactions on Neural Networks and Learning Systems*, 2023.

[24] Yongping Dan, Changhao Sun, Hengyi Li, and Lin Meng. Adaptive spiking neuron with population coding for a residual spiking neural network. *Applied Intelligence*, 55(4):288, 2025.

[25] Suixin Deng, Junlong Li, Quansheng He, Xiaoxue Zhang, Jie Zhu, Liang Li, Zhen Mi, Xiufeng Yang, Man Jiang, Qiang Dong, et al. Regulation of recurrent inhibition by asynchronous glutamate release in neocortex. *Neuron*, 2019.

[26] Alain Destexhe and Mayank Mehta. Properties and computational consequences of fast dendritic spikes during natural behavior. *Neuroscience*, 489:251–261, 2022.

[27] Dexin Duan, Peilin Liu, Bingwei Hui, and Fei Wen. Brain-inspired online adaptation for remote sensing with spiking neural network. *IEEE Transactions on Geoscience and Remote Sensing*, 2025.

[28] Robert Egger, Rajeevan T Narayanan, Jason M Guest, Arco Bast, Daniel Udvary, Luis F Messore, Suman Das, Christiaan PJ De Kock, and Marcel Oberlaender. Cortical output is gated by horizontally projecting neurons in the deep layers. *Neuron*, 105(1):122–137, 2020.

[29] Mohd Faizan, Sajad A Loan, and Hend I Alkhammash. Highly scalable in0. 95ga0. 05as based controllable leaky-integrate-fire neuron for high performance spiking neural network and applications. *Physica Scripta*, 100(2):025934, 2025.

[30] Wei Fang, Zhaofei Yu, Yanqi Chen, Tiejun Huang, Timothée Masquelier, and Yonghong Tian. Deep residual learning in spiking neural networks. *Advances in Neural Information Processing Systems*, 34:21056–21069, 2021.

[31] Sergey Filist, Riad Taha Al-Kasasbeh, Olga Vladimirovna Shatalova, Mohammad Hjouj Btoush, Manafaddin Namazov, Ashraf Adel Shaqadan, Mahdi Salman Alshamasin, Nikolay Korenevskiy, Saleh Aloqeili, and Maxim Borisovich Myasnyankin. Biotechnical neural network system for predicting cardiovascular health state using processing of bio-signals. *International Journal of Medical Engineering and Informatics*, 2024.

[32] ShouWei Gao, XiangYu Fan, XingYang Deng, ZiChao Hong, Hao Zhou, and ZiHao Zhu. Te-spikformer: Temporal-enhanced spiking neural network with transformer. *Neurocomputing*, 602:128268, 2024.

[33] Shouwei Gao, Ruixin Zhu, Yu Qin, Wenyu Tang, and Hao Zhou. Sg-snn: a self-organizing spiking neural network based on temporal information. *Cognitive Neurodynamics*, 19(1):14, 2025.

[34] Richard Gast, Sara A Solla, and Ann Kennedy. Neural heterogeneity controls computations in spiking neural networks. *Proceedings of the National Academy of Sciences*, 121(3):e2311885121, 2024.

[35] Marco Gatti, Jessica Amianto Barbato, and Claudio Zandron. Spiking neural network classification of x-ray chest images. *Knowledge-Based Systems*, 314:113194, 2025.

[36] Padraig Gleeson, Matteo Cantarelli, Boris Marin, Adrian Quintana, Matt Earnshaw, Sadra Sadeh, Eugenio Piasini, Justas Birgiolas, Robert C Cannon, N Alex Cayco-Gajic, et al. Open source brain: a collaborative resource for visualizing, analyzing, simulating, and developing standardized models of neurons and circuits. *Neuron*, 103(3):395–411, 2019.

[37] Juan M Górriz, Javier Ramírez, Andres Ortiz, Francisco J Martinez-Murcia, Fermin Segovia, John Suckling, Matthew Leming, Yu-Dong Zhang, Jose Ramón Álvarez-Sánchez, Guido Bologna, et al. Artificial intelligence within the interplay between natural and artificial computation: Advances in data science, trends and applications. *Neurocomputing*, 410:237–270, 2020.

[38] Olivia Guest and Andrea E Martin. On logical inference over brains, behaviour, and artificial neural networks. *Computational Brain & Behavior*, 6(2):213–227, 2023.

[39] Lei Guo, Weihang Ding, Youxi Wu, Menghua Man, and Miaomiao Guo. Anti-damage ability of biological plausible spiking neural network with synaptic time delay based on speech recognition under random attack. *Engineering Applications of Artificial Intelligence*, 144:110061, 2025.

[40] Lei Guo, Chongming Li, Huan Liu, and Yihua Song. Complex spiking neural network evaluated by injury resistance under stochastic attacks. *Brain Sciences*, 15(2):186, 2025.

[41] Max Haberbusch, Silvia Frullini, and Francesco Moscato. A numerical model of the acute cardiac effects provoked by cervical vagus nerve stimulation. *IEEE Transactions on Biomedical Engineering*, 69(2):613–623, 2021.

[42] Bing Han, Feifei Zhao, Yang Li, Qingqun Kong, Xianqi Li, and Yi Zeng. Similarity-based context aware continual learning for spiking neural networks. *Neural Networks*, 184:107037, 2025.

[43] Bing Han, Feifei Zhao, Wenxuan Pan, and Yi Zeng. Adaptive sparse structure development with pruning and regeneration for spiking neural networks. *Information Sciences*, 689:121481, 2025.

[44] Iman Yakzan Abou Hassan and Nikola K Kasabov. Neuden: a framework for the integration of neuromorphic evolving spiking neural networks with dynamic evolving neuro-fuzzy systems for predictive and explainable modelling of streaming data. *Evolving Systems*, 16(1):1–18, 2025.

[45] Malik Khizar Hayat, Ali Daud, Ameen Banjar, Riad Alharbey, and Amal Bukhari. A deep co-evolution architecture for anomaly detection in dynamic networks. *Multimedia Tools and Applications*, 83(14):40489–40508, 2024.

[46] Ping He, Rong Xiao, Chenwei Tang, Shudong Huang, Jiancheng Lv, and Huajin Tang. Stsf: Spiking time sparse feedback learning for spiking neural networks. *IEEE Transactions on Neural Networks and Learning Systems*, 2025.

[47] Alexander Henkes, Jason K Eshraghian, and Henning Wessels. Spiking neural networks for nonlinear regression. *Royal Society Open Science*, 11(5):231606, 2024.

[48] Eghbal A Hosseini, Martin Schrimpf, Yian Zhang, Samuel Bowman, Noga Zaslavsky, and Evelina Fedorenko. Artificial neural network language models predict human brain responses to language even after a developmentally realistic amount of training. *Neurobiology of Language*, 5(1):43–63, 2024.

[49] Yung-Ting Hsieh, Khizar Anjum, and Dario Pompili. Ultra-low power analog folded neural network for cardiovascular health monitoring. *IEEE Journal of Biomedical and Health Informatics*, 2024.

[50] Eugene M Izhikevich. Simple model of spiking neurons. *IEEE Transactions on neural networks*, 14(6):1569–1572, 2003.

[51] Faisal Jamil and Do Hyeun Kim. Improving accuracy of the alpha–beta filter algorithm using an ann-based learning mechanism in indoor navigation system. *Sensors*, 19(18):3946, 2019.

[52] Taewook Kang, Chanwoo Shin, Jongseok Lee, Jae-Jin Lee, Donggyu Sim, and Seong-Eun Kim. Bcrnet-snn: Body channel response-aware spiking neural network for user recognition. *IEEE Transactions on Industrial Informatics*, 2025.

[53] Anurag Kavatlawar, Ananya Bohare, Anup Dakare, Ayush Dubey, and Madhuri Sahu. Cardiovascular disease (cvd) recognition using convolutional neural networks. *Grenze International Journal of Engineering & Technology (GIJET)*, 10, 2024.

[54] Junaid Ali Khan, Muhammad Asif Zahoor Raja, Muhammed I Syam, Shujaat Ali Khan Tanoli, and Saeed Ehsan Awan. Design and application of nature inspired computing approach for nonlinear stiff oscillatory problems. *Neural Computing and Applications*, 26:1763–1780, 2015.

[55] Robert Kim and Terrence J Sejnowski. Strong inhibitory signaling underlies stable temporal dynamics and working memory in spiking neural networks. *Nature neuroscience*, 24(1):129–139, 2021.

[56] AV Kurbako, DM Ezhov, VI Ponomarenko, and MD Prokhorov. Spike-timing dependent plasticity learning of small spiking neural network for image recognition. *The European Physical Journal Special Topics*, pages 1–10, 2025.

[57] Yawen Lan, Yuchen Wang, Yuping Zhang, and Hong Zhu. Low-power and lightweight spiking transformer for eeg-based auditory attention detection. *Neural Networks*, 183:106977, 2025.

[58] Yunlin Lei, Huiqi Li, Mingrui Li, Yaoyu Chen, Yu Zhang, Zihui Jin, and Xu Yang. How to form brain-like memory in spiking neural networks with the help of frequency-induced mechanism. *Neurocomputing*, 623:129361, 2025.

[59] Pengju Li, Yasheng Zhang, Jiayu Qiu, Jun He, Jishun Li, Chixing Lu, Yuqiang Fang, and Jian Zhao. Msr-snn: Advancing neuromorphic vision object classification with multi-scale-residual spiking neural networks. *IEEE Sensors Journal*, 2025.

[60] Qianyi Li, Ben Sorscher, and Haim Sompolinsky. Representations and generalization in artificial and brain neural networks. *Proceedings of the National Academy of Sciences*, 121(27):e2311805121, 2024.

[61] Xiao Li, Xieyuanli Chen, Ruibin Guo, Yujie Wu, Zongtan Zhou, Fangwen Yu, and Huimin Lu. Neurove: Brain-inspired linear-angular velocity estimation with spiking neural networks. *IEEE Robotics and Automation Letters*, 2025.

[62] Yanyan Li, Bosheng Song, and Xiangxiang Zeng. Spiking neural p systems with weights and delays on synapses. *Theoretical Computer Science*, page 114028, 2023.

[63] Yudong Li, Yunlin Lei, and Xu Yang. Rethinking residual connection in training large-scale spiking neural networks. *Neurocomputing*, 616:128950, 2025.

[64] Xingyue Liang, Qiaoyun Wu, Wenzhang Liu, Yun Zhou, Chunyu Tan, Hongfu Yin, and Changyin Sun. Intrinsic plasticity coding improved spiking actor network for reinforcement learning. *Neural Networks*, 184:107054, 2025.

[65] Xiaojian Liao, Guang Li, You Wang, Lining Sun, and Hongmiao Zhang. Constructing lightweight and efficient spiking neural networks for eeg-based motor imagery classification. *Biomedical Signal Processing and Control*, 100:107000, 2025.

[66] Xiaode Liu, Yufei Guo, Yuanpei Chen, Jie Zhou, Yuhan Zhang, Weihang Peng, Xuhui Huang, and Zhe Ma. Enhancing navigation performance in unknown environments using spiking neural networks and reinforcement learning with asymptotic gradient method. *Complex & Intelligent Systems*, 11(2):1–13, 2025.

[67] Xiyu Liu, Yuzhen Zhao, and Liping Wang. Nonlinear neural-like p model for time series classification. *Theoretical Computer Science*, page 114055, 2023.

[68] Yoav Livneh, Arthur U Sugden, Joseph C Madara, Rachel A Essner, Vanessa I Flores, Lauren A Sugden, Jon M Resch, Bradford B Lowell, and Mark L Andermann. Estimation of current and future physiological states in insular cortex. *Neuron*, 105(6):1094–1111, 2020.

[69] Fabrizio Lombardi, Selver Pepić, Oren Shriki, Gašper Tkačik, and Daniele De Martino. Statistical modeling of adaptive neural networks explains co-existence of avalanches and oscillations in resting human brain. *Nature Computational Science*, 3(3):254–263, 2023.

[70] Sergio Lucas and Eva Portillo. Methodology based on spiking neural networks for univariate time-series forecasting. *Neural Networks*, 173:106171, 2024.

[71] Eugene M Izhikevich and Gerald M Edelman. Large-scale model of mammalian thalamocortical systems. *Proceedings of the national academy of sciences*, 105(9):3593–3598, 2008.

[72] Jean-Pierre Roussarie, Vicky Yao, Patricia Rodriguez-Rodriguez, Rose Oughtred, Jennifer Rust, Zakary Plautz, Shirin Kasturia, Christian Albornoz, Wei Wang, Eric F Schmidt, et al. Selective neuronal vulnerability in alzheimer disease: a network-based analysis. *Neuron*, 107(5):821–835, 2020.

[73] Oleg I Rumyantsev, Jérôme A Lecoq, Oscar Hernandez, Yanping Zhang, Joan Savall, Radosław Chrapkiewicz, Jane Li, Hongkui Zeng, Surya Ganguli, and Mark J Schnitzer. Fundamental bounds on the fidelity of sensory cortical coding. *Nature*, 580(7801):100–105, 2020.

[74] Basabdatta Sen-Bhattacharya, Sebastian James, Oliver Rhodes, Indar Sugiarto, Andrew Rowley, Alan B Stokes, Kevin Gurney, and Steve B Furber. Building a spiking neural network model of the basal ganglia on spinnaker. *IEEE Transactions on Cognitive and Developmental Systems*, 10(3):823–836, 2018.

[75] Jun Igarashi, Hiroshi Yamaura, and Tadashi Yamazaki. Large-scale simulation of a layered cortical sheet of spiking network model using a tile partitioning method. *Frontiers in Neuroinformatics*, 13:71, 2019.

[76] Maximilian Schmidt, Rembrandt Bakker, Claus C Hilgetag, Markus Diesmann, and Sacha J van Albada. Multi-scale account of the network structure of macaque visual cortex. *Brain Structure and Function*, 223(3):1409–1435, 2018.

[77] David B Stockton and Fidel Santamaria. Integrating the allen brain institute cell types database into automated neuroscience workflow. *Neuroinformatics*, 15(4):333–342, 2017.

[78] F Malandrone, V Catrambone, S Carletto, PG Rossini, M Coletti Moja, F Oliva, M Pagani, G Valenza, and L Ostacoli. Restoring bottom-up communication in brain-heart interplay after trauma-focused psychotherapy in breast cancer patients with post-traumatic stress disorder. *Journal of Affective Disorders*, 351:143–150, 2024.

[79] Shifeng Mao, Baoxin Yang, Hongze Sun, Wuque Cai, and Daqing Guo. Tr-snn: a lightweight spiking neural network based on tensor ring decomposition. *Brain-Apparatus Communication: A Journal of Bacomics*, 4(1):2472166, 2025.

[80] Jesse A Mark, Adrian Curtin, Amanda E Kraft, Matthias D Ziegler, and Hasan Ayaz. Mental workload assessment by monitoring brain, heart, and eye with six biomedical modalities during six cognitive tasks. *Frontiers in neuroergonomics*, 5:1345507, 2024.

[81] Asif Mehmood, Ayesha Ilyas, and Hajira Ilyas. Cardiac heterogeneity prediction by cardio-neural network simulation. *Neuroinformatics*, 23(2):1–21, 2025.

[82] Asif Mehmood and Muhammad Javed Iqbal. Hybrid excitable spiking neural network for cardiovascular disease prediction. *IEEE Access*, 11:128187–128197, 2023.

[83] Asif Mehmood and Muhammad Javed Iqbal. Hybrid spiking neural networks for anomaly detection of brain, heart and pancreas. *Arabian Journal for Science and Engineering*, pages 1–11, 2024.

[84] Asif Mehmood, Muhammad Javed Iqbal, Hassan Dawood, and Ping Guo. Computationally efficient low power neuron model for digital brain. In *2018 14th International Conference on Computational Intelligence and Security (CIS)*, pages 1–5. IEEE, 2018.

[85] Farzaneh Najafi, Gamaleldin F Elsayed, Robin Cao, Eftychios Pnevmatikakis, Peter E Latham, John P Cunningham, and Anne K Churchland. Excitatory and inhibitory subnetworks are equally selective during decision-making and emerge simultaneously during learning. *Neuron*, 105(1):165–179, 2020.

[86] Li-Ye Niu, Ying Wei, Liping Zhao, and Keli Hu. Deep spiking neural networks based on model fusion technology for remote sensing image classification. *Engineering Applications of Artificial Intelligence*, 142:109873, 2025.

[87] Obinnaya CB Omankwu, MC Okoronkwo, and Chigbundu Kanu. Cardiovascular (heart) diseases prediction using deep learning neural network model. *NIPES-Journal of Science and Technology Research*, 6(1), 2024.

[88] Alejandro Torrado Pacheco, Juliet Bottorff, Ya Gao, and Gina G Turrigiano. Sleep promotes downward firing rate homeostasis. *Neuron*, 109(3):530–544, 2021.

[89] Michalis Pagkalos, Spyridon Chavlis, and Panayiota Poirazi. Introducing the dendrify framework for incorporating dendrites to spiking neural networks. *Nature Communications*, 14(1):131, 2023.

[90] Woojun Park, Jongmu Kim, Inhoi Jeong, and Kyoung J Lee. Temporal pavlovian conditioning of a model spiking neural network for discrimination sequences of short time intervals. *Journal of Computational Neuroscience*, pages 1–17, 2025.

[91] Roshan Paudel, Mohsin Saleet Jafri, and Aman Ullah. Pacing dynamics determines the arrhythmogenic mechanism of the cpvt2-causing casq2g112+ 5x mutation in a guinea pig ventricular myocyte computational model. *Genes*, 14(1):23, 2023.

[92] Luca Pegolotti, Martin R Pfaller, Natalia L Rubio, Ke Ding, Rita Brugarolas Brufau, Eric Darve, and Alison L Marsden. Learning reduced-order models for cardiovascular simulations with graph neural networks. *Computers in Biology and Medicine*, 168:107676, 2024.

[93] Spase Petkoski and Viktor K Jirsa. Normalizing the brain connectome for communication through synchronization. *Network Neuroscience*, pages 1–56, 2022.

[94] Lisa Quadt, Hugo Critchley, and Yoko Nagai. Cognition, emotion, and the central autonomic network. *Autonomic Neuroscience*, 238:102948, 2022.

[95] Gianluca Quaglio, Patrizia Toia, Edvard I Moser, Theodoros Karapiperis, Katrin Amunts, Shigeo Okabe, Mu ming Poo, Jong Cheol Rah, Yves De Koninck, John Ngai, et al. The international brain initiative: enabling collaborative science. *The Lancet Neurology*, 20(12):985–986, 2021.

[96] Muhammad Imran Razzak, Muhammad Imran, and Guandong Xu. Efficient brain tumor segmentation with multiscale two-pathway-group conventional neural networks. *IEEE journal of biomedical and health informatics*, 23(5):1911–1919, 2018.

[97] Bernardete Ribeiro, Francisco Antunes, Dylan Perdigão, and Catarina Silva. Convolutional spiking neural networks targeting learning and inference in highly imbalanced datasets. *Pattern Recognition Letters*, 189:241–247, 2025.

[98] MA Seenivasan, Adarsh V Parekkattil, Rekib Uddin Ahmed, and Prabir Saha. Biologically inspired tonic and bursting lif neuron model for spiking neural network: a cmos implementation. *Microsystem Technologies*, 31(2):475–489, 2025.

[99] Fitzwilliam Seibertz, Markus Rapedius, Funsho E Fakuade, Philipp Tomsits, Aiste Liutkute, Lukas Cyganek, Nadine Becker, Rupamanjari Majumder, Sebastian Clauß, Niels Fertig, et al. A modern automated patch-clamp approach for high throughput electrophysiology recordings in native cardiomyocytes. *Communications biology*, 5(1):1–10, 2022.

[100] Ahmed Shaban, Sai Sukruth Bezugam, and Manan Suri. An adaptive threshold neuron for recurrent spiking neural networks with nanodevice hardware implementation. *Nature Communications*, 12(1):4234, 2021.

[101] Feng Shao and Zheng Shen. How can artificial neural networks approximate the brain? *Frontiers in Psychology*, 13:970214, 2023.

[102] Guobin Shen, Dongcheng Zhao, and Yi Zeng. Exploiting high performance spiking neural networks with efficient spiking patterns. *IEEE Transactions on Emerging Topics in Computational Intelligence*, 2025.

[103] Jiangrong Shen, Wenyao Ni, Qi Xu, Gang Pan, and Huajin Tang. Context gating in spiking neural networks: Achieving lifelong learning through integration of local and global plasticity. *Knowledge-Based Systems*, page 112999, 2025.

[104] Jiankai Shi, Yue Zhao, Chu Wang, Hong Zeng, and Guojun Dai. Eegsnet: A novel eeg cognitive recognition model using spiking neural network. *Biomedical Signal Processing and Control*, 105:107610, 2025.

[105] Kexin Shi, Mengshu Hou, Xiaoling Luo, Dehao Zhang, Hanwen Liu, and Jingya Wang. Spike-vad: Efficient and robust spiking neural network for voice activity detection. *IEEE Transactions on Cognitive and Developmental Systems*, 2025.

[106] Ninni Singh, Vinit Kumar Gunjan, Fahimuddin Shaik, and Sudipta Roy. Detection of cardio vascular abnormalities using gradient descent optimization and cnn. *Health and Technology*, 14(1):155–168, 2024.

[107] Raunak Sinha, Tabrez J Siddiqui, Nirmala Padmanabhan, Julie Wallin, Chi Zhang, Benyamin Karimi, Fred Rieke, Ann Marie Craig, Rachel O Wong, and Mrinalini Hoon. Lrrtm4: A novel regulator of presynaptic inhibition and ribbon synapse arrangements of retinal bipolar cells. *Neuron*, 2020.

[108] PV Sruthi and TS Bindiya. Modeling of izhikevich spiking neurons with high matching accuracy using comb-exp functions and its multiplier-free realization. *IEEE Transactions on Circuits and Systems I: Regular Papers*, 2025.

[109] David Sterratt, Bruce Graham, Andrew Gillies, Gaute Einevoll, and David Willshaw. *Principles of computational modelling in neuroscience*. Cambridge University Press, 2023.

[110] Anand Subramoney, Guillaume Bellec, Franz Scherr, Robert Legenstein, and Wolfgang Maass. Fast learning without synaptic plasticity in spiking neural networks. *Scientific Reports*, 14(1):8557, 2024.

[111] Sara Sultana, Sharifullah Khan, and Muhammad A Abbas. Predicting performance of electrical engineering students using cognitive and non-cognitive features for identification of potential dropouts. *International Journal of Electrical Engineering Education*, 54(2):105–118, 2017.

[112] Pengfei Sun, Jorg De Winne, Malu Zhang, Paul Devos, and Dick Botteldooren. Delayed knowledge transfer: Cross-modal knowledge transfer from delayed stimulus to eeg for continuous attention detection based on spike-represented eeg signals. *Neural Networks*, 183:107003, 2025.

[113] Pengfei Sun, Jibin Wu, Paul Devos, and Dick Botteldooren. Towards parameter-free attentional spiking neural networks. *Neural Networks*, 185:107154, 2025.

[114] Henry Sutanto. Transforming clinical cardiology through neural networks and deep learning: A guide for clinicians. *Current Problems in Cardiology*, page 102454, 2024.

[115] Ali Turab, Wutiphol Sintunavarat, Farhan Ullah, Shujaat Ali Zaidi, Andrés Montoyo, and Josué-Antonio Nescolarde-Selva. Computational modelling of animal behaviour in t-mazes: Insights from machine learning. *Ecological Informatics*, 81:102639, 2024.

[116] AM Uttley. Progress in brain research. volume 2: Nerve, brain and memory models. by norbert wiener and jp schade. elsevier publishing company ltd. 1963. pp. 280. price 80s. *The British Journal of Psychiatry*, 110(466):448–448, 1964.

[117] C Venkatesan, P Karthigaikumar, Anand Paul, S Satheeskumaran, and Rajagopal Kumar. Ecg signal preprocessing and svm classifier-based abnormality detection in remote healthcare applications. *IEEE Access*, 6:9767–9773, 2018.

[118] Shui-Hua Wang, Preetha Phillips, Yuxiu Sui, Bin Liu, Ming Yang, and Hong Cheng. Classification of alzheimer's disease based on eight-layer convolutional neural network with leaky rectified linear unit and max pooling. *Journal of medical systems*, 42:1–11, 2018.

[119] Yu Wang, Xinxin Yin, Zhouzhou Zhang, Jiejue Li, Wenyu Zhao, and Zengcai V Guo. A cortico-basal ganglia-thalamo-cortical channel underlying short-term memory. *Neuron*, 109(21):3486–3499, 2021.

[120] Yusong Wang, Xuanye Fang, Huifeng Yin, Dongyuan Li, Guoqi Li, Qi Xu, Yi Xu, Shuai Zhong, and Mingkun Xu. Big-fusion: Brain-inspired global-local context fusion framework for multimodal emotion recognition in conversations. In *Proceedings of the AAAI Conference on Artificial Intelligence*, volume 39, pages 1574–1582, 2025.

[121] Zisheng Wang, Shaochen Li, Jianping Xuan, and Tielin Shi. Biologically inspired compound defect detection using a spiking neural network with continuous time–frequency gradients. *Advanced Engineering Informatics*, 65:103132, 2025.

[122] Kaichao Wu and Leonardo L Gollo. Mapping and modeling age-related changes in intrinsic neural timescales. *Communications Biology*, 8(1):167, 2025.

[123] Chetali Yadav and Bhupendra Singh Reniwal. Spatially invariant convolutional spiking neural network for resource-constrained iot devices. *Circuits, Systems, and Signal Processing*, pages 1–22, 2025.

[124] Yi Yang, Richard M Voyles, Haiyan H Zhang, and Robert A Nawrocki. Fractional-order spike-timing-dependent gradient descent for multi-layer spiking neural networks. *Neurocomputing*, 611:128662, 2025.

[125] Man Yao, Guangshe Zhao, Hengyu Zhang, Yifan Hu, Lei Deng, Yonghong Tian, Bo Xu, and Guoqi Li. Attention spiking neural networks. *IEEE transactions on pattern analysis and machine intelligence*, 45(8):9393–9410, 2023.

[126] Zexiang Yi, Jing Lian, Qidong Liu, Hegui Zhu, Dong Liang, and Jizhao Liu. Learning rules in spiking neural networks: A survey. *Neurocomputing*, 531:163–179, 2023.

[127] Bojian Yin, Federico Corradi, and Sander M Bohté. Accurate and efficient time-domain classification with adaptive spiking recurrent neural networks. *Nature Machine Intelligence*, 3(10):905–913, 2021.

[128] Bojian Yin, Federico Corradi, and Sander M Bohté. Accurate online training of dynamical spiking neural networks through forward propagation through time. *Nature Machine Intelligence*, 5(5):518–527, 2023.

[129] Qian Yin, Bingxin Xu, Kaiyan Zhou, and Ping Guo. Bayesian pseudoinverse learners: from uncertainty to deterministic learning. *IEEE transactions on cybernetics*, 52(11):12205–12216, 2021.

[130] Chuhan Zhang, Wei Pan, and Cosimo Della Santina. Nisnn-a: Noniterative spiking neural network with attention with application to motor imagery eeg classification. *IEEE Transactions on Neural Networks and Learning Systems*, 2025.

[131] Geng Zhang, Shuangming Yang, Xuetao Zhang, and Badong Chen. Biologically plausible unsupervised learning for self-organizing spiking neural networks with dendritic computation. *Neurocomputing*, 631:129707, 2025.

[132] Jing Zhang, Tianlang Yang, Cheng Jiang, Jingwei Liu, and Haoran Zhang. Chaotic loss-based spiking neural network for privacy-preserving bullying detection in public places. *Applied Soft Computing*, 169:112643, 2025.

[133] Xiangyu Zhang, Joshua Kim, and Susumu Tonegawa. Amygdala reward neurons form and store fear extinction memory. *Neuron*, 105(6):1077–1093, 2020.

[134] Youdong Zhang, Lingfei Mo, Xu He, and Xiaolin Meng. Unsupervised spiking neural network based on liquid state machine and self-organizing map. *Neurocomputing*, 620:129120, 2025.

[135] Di Zhao, Jixiang Zong, Jiulong Wang, Guirun Li, and Ruopu Wu. Polaris 23: a high throughput neuromorphic processing element by risc-v customized instruction extension for spiking neural network (rv-snn 2.0) and simd-style implementation of lif model with backpropagation stdp. *The Journal of Supercomputing*, 81(2):398, 2025.

[136] Dongcheng Zhao, Guobin Shen, Yiting Dong, Yang Li, and Yi Zeng. Improving stability and performance of spiking neural networks through enhancing temporal consistency. *Pattern Recognition*, 159:111094, 2025.

[137] Hanle Zheng, Zhong Zheng, Rui Hu, Bo Xiao, Yujie Wu, Fangwen Yu, Xue Liu, Guoqi Li, and Lei Deng. Temporal dendritic heterogeneity incorporated with spiking neural networks for learning multi-timescale dynamics. *Nature Communications*, 15(1):277, 2024.

[138] Jiayi Zheng, Yaping Wan, Xin Yang, Hua Zhong, Minghua Du, and Gang Wang. Motion feature extraction using magnocellular-inspired spiking neural networks for drone detection. *Frontiers in Computational Neuroscience*, 19:1452203, 2025.

[139] Hongliang Zhou, Tingting Xiong, Zhongpeng Dai, Haowen Zou, Xvmiao Wang, Hao Tang, Yinghong Huang, Hao Sun, Wei You, Zhijian Yao, et al. Brain–heart interaction disruption in major depressive disorder: disturbed rhythm modulation of the cardiac

cycle on brain transient theta bursts. *European Archives of Psychiatry and Clinical Neuroscience*, 274(3):595–607, 2024.

[140] Yue Zhou, Jiawei Fu, Zirui Chen, Fuwei Zhuge, Yasai Wang, Jianmin Yan, Sijie Ma, Lin Xu, Huanmei Yuan, Mansun Chan, et al. Computational event-driven vision sensors for in-sensor spiking neural networks. *Nature Electronics*, 6(11):870–878, 2023.

[141] Zhichao Zhu, Yang Qi, Wenlian Lu, Zhigang Wang, Lu Cao, and Jianfeng Feng. Toward a free-response paradigm of decision-making in spiking neural networks. *Neural Computation*, pages 1–41, 2025.

[142] Asif Mehmood. NeuroBit64: 64 time-shared neurons that store their decisions in a serial memory. Verilog design, tests and SkyWater 130 nm layout. https://github.com/asifnazquaidian/neurobit64, 2026.

[143] Asif Mehmood. NeuroBit64-Cardio: a cardio-neural network chip of 1000 cardiac myocytes with alpha- and beta-adrenergic neurons. https://github.com/asifnazquaidian/neurobit64-cardio, 2026. Running application: https://asifnazquaidian.github.io/neurobit64-cardio/app/?organ=heart.

[144] Asif Mehmood. NeuroBit64-Pancreas: an islet network chip of 1000 pancreatic alpha, beta and delta cells with adrenergic neurons. https://github.com/asifnazquaidian/neurobit64-pancreas, 2026. Running application: https://asifnazquaidian.github.io/neurobit64-pancreas/app/?organ=pancreas.

[145] Asif Mehmood. NeuroBit64-Kidney: a network chip of 1000 nephron units with alpha-1 and beta-1 adrenergic neurons. https://github.com/asifnazquaidian/neurobit64-kidney, 2026. Running application: https://asifnazquaidian.github.io/neurobit64-kidney/app/?organ=kidney.

[146] Tiny Tapeout. Tiny Tapeout: an educational project that makes it possible to manufacture small digital designs on a shared chip. https://tinytapeout.com, 2026.

[147] Asif Mehmood. NeuroBit64 body monitor: brain, heart, pancreas and kidney chips running together with an anomaly detector. https://github.com/asifnazquaidian/neurobit64-body, 2026. Running application: https://asifnazquaidian.github.io/neurobit64-body/app/.

[148] Asif Mehmood. GlucoSense: a web application for a wearable glucose monitor with Bluetooth Low Energy. https://glucosensor.netlify.app, 2026.

[149] Asif Mehmood. GlucoSense GS-1: digital core of a wearable glucose-sensor chip with a hybrid excitable cell islet model. https://github.com/asifnazquaidian/glucosense-gs1, 2026. Running application: https://asifnazquaidian.github.io/glucosense-gs1/app/.

ABOUT THIS THESIS

How can a computer simulate a brain of one hundred billion neurons, and listen to the heart at the same time? This thesis proposes a **unified hybrid excitable cell model**. It combines an adaptive threshold, neurotransmitter dynamics and adrenergic receptors, so one compact set of equations reproduces the rich firing patterns of neurons and the electrical activity of cardiac myocytes.

Validated on recordings from 2191 mouse visual-cortex neurons, the model reaches an **86 % coincidence factor** and an **83 % firing-rate coefficient**, ahead of the GLIF, MAT and QIF models. With neurons coded as bits, a network of **100 billion neurons** fits in about 13 GB of memory. The same model reproduces the cardiac action potentials of eight species, and a 1000-cell cardio-neural network predicts heart rate variability. This lays the computational groundwork for future **brain–heart interfaces**.

Spiking Neural Networks | Computational Neuroscience | Brain–Heart Interface

DR. ASIF MEHMOOD

University of Engineering and Technology, Taxila, Pakistan